Approaches to Particulate Matter Monitoring, Sampling and Analysis for Personal Exposure Evaluation

Jiayang He

A dissertation

submitted in partial fulfillment of the

requirements for the degree of

Doctor of Philosophy

University of Washington

2021

Reading Committee:

Igor Novosselov, Chair
Edmund Seto
Alberto Aliseda

Program Authorized to Offer Degree:

Mechanical Engineering

ABSTRACT

Aerosol is a suspension of airborne particles in the air or other gas. It is more commonly known as Particulate Matter (PM). Aerosols are ubiquitous throughout our environment in various forms, such as dust, fume, smog, mist, etc. They originate from both natural and anthropogenic sources. Some natural aerosols include pollen, sea salts, smoke from forest fires, and desert dust. Examples of anthropogenic sources include mobile and industrial combustion, construction sites, domestic fuel burning. These aerosols come in a wide range in size from a few nanometers (nm)—less than the width of the smallest viruses—to several tens of micrometers (μm)—about the diameter of human hair. They have significant impacts on climate, human health, and quality of life. This work focuses on developing tools and methods for monitoring, sampling, and analyzing course, fine and ultrafine aerosols (between 10 nm and 10 μm) to study and mitigate their health impact.

ACKNOWLEDGEMENTS

I owe a debt of gratitude to many for the financial, educational, and emotional support provided to me over the long and winding road which resulted in this dissertation. First, I would like to thank my advisor Dr. Igor Novosselov for constant guidance and support. Thank you for introducing me to the aerosol science field and providing me with the opportunity to conduct research in the Novosselov Research Group. Thank you for allowing me to explore my research interests with freedom and providing help whenever needed. I also want to thank Dr. Alberto Aliseda, Dr. Edmund Seto, Dr. Timothy Larson, Dr. Christopher Simpson, and Dr. James Hecker for their valuable feedback on my research. It has been an honor and a joy to work with all of you.

This work would not have been possible without the constant support of Dr. Jay Rutherford and Dr. Gaurav Mahamuni. Thank you for being the best people to discuss ideas with and work in collaboration on projects with throughout graduate school. My work in the EEM analysis field would not have been possible without the foundation you built. I want to thank Byron Ockerman, our outstanding research engineer, for his unparalleled hardware skills. I can always count on the hardware you built to conduct my research.

I would also like to express my appreciation to the crew working on the AeroSpec project. In particular, I would like to thank Dr. Sep Makhsous, Brenden Singh, Cheng-Ying (Eric) Wu, Ching-Hsuan (Shirley) Huang, Yuwen Li, Robert Rochlin, Zehua Zhu, Ziyi Huang and Jiawei Zhang. Without their help, much of my work in the sensor network field would not have been possible.

Finally, I offer my deep gratitude to my family and dear friends for their patience, love and support, throughout this long and challenging journey. To my dad, Junxing He, I offer

appreciation for fostering in me an appreciation for education, and to my mom, Yali Ren, for always believing in me. To my wife, Mengyao Zhang, words cannot express the depth of my gratitude. I owe you a world of love and appreciation for always encouraging me, helping me with data analysis, cooking the delicious meals that fed my body and soul.

TABLE OF CONTENTS

LIST OF FIGURES

LIST OF TABLES

Chapter 1. INTRODUCTION

1.1 BACKGROUND

Aerosol is a suspension of airborne particles in air or other gas [1]. It is more commonly known as Particulate Matter (PM) by the public. Aerosols are ubiquitous throughout our environment in various forms, such as dust, fume, smog, mist, etc. They originate from both natural and anthropogenic sources. Some natural aerosols include pollen, sea salts, smoke from forest fires, and desert dust. Examples of anthropogenic sources include mobile and industrial combustion, construction sites, domestic fuel burning. These aerosols come in a wide range in size from a few nanometers (nm)—less than the width of the smallest viruses—to several tens of micrometers (μm)—about the diameter of human hair. They have significant impacts on climate, human health, and quality of life. This work focuses on developing tools, methods for monitoring, sampling, and analyzing fine and ultrafine aerosols (aerosols between 10 nm and 10 μm) to study and mitigate their negative health impact.

Figure 1.1. Sea salt, dust, and volcanic ash are three common types of aerosols in the atmosphere. (Photograph by Katherine Mann.)

1.2 HEALTH IMPACTS OF AEROSOL

Human exposure to PM is associated with multiple adverse health effects, including cardiovascular disease, cardiopulmonary disease, and lung cancer [2-6]. Estimates show that approximately 3% of cardiopulmonary and 5% of lung cancer deaths are attributed to exposures to PM globally [7]. Exposure to PM, particularly combustion-generated aerosols, has been linked to respiratory and cardiovascular health effects, including ischemic heart disease, stroke, cardiovascular mortality, and exacerbations of asthma and chronic obstructive pulmonary disease [8-10]. The hazard caused by inhaled particles depends on the particle deposition site within the respiratory system as well as their chemical composition. Particle deposition in the human respiratory tract depends on particles' aerodynamic size [11, 12]. Aerodynamic size is defined as the diameter of the spherical particles with a density of 1000kg/m^3 that has the same settling velocity as the particle. Humans have evolved effective defense mechanisms against larger particles, which can be removed by impaction and sedimentation in the ciliated airways of the lungs. However, smaller particles can penetrate deeper into the lungs remain there for varying times depending on the physicochemical properties and type of clearance mechanism involved. EPA groups regulated particle pollution into two categories: "Coarse particles" which are particles larger than 2.5 micrometers and smaller than 10 micrometers in diameter (PM_{10}). These particles are deposited into the airways in the head region when inhaled. "Fine particles" are particles smaller than 2.5 micrometers ($PM_{2.5}$) in diameter; when inhaled, they are deposited into lung airways or the tracheobronchial region. Besides these two categories, there is a growing concern in the public health community about the contribution of Ultrafine particles (UFPs) to adverse human health impacts. UFPs are aerosols with an aerodynamic diameter of 0.1 μm (100 nm) or less. They dominate in terms of the number of particles in the ambient air with the ability

to reach the most distal lung regions (alveoli) and circumvent primary airway defenses (see Figure 1.2). Moreover, UFPs have a high surface area and can adsorb a substantial amount of toxic organic compounds.

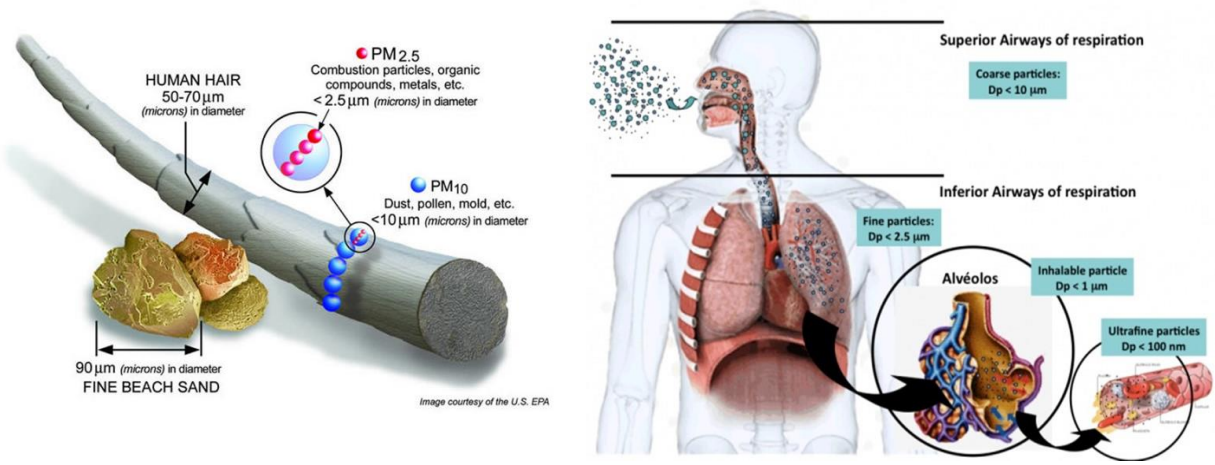

Figure 1.2. Left: Graphical illustration of the relative size of particulate matter (available from EPA.gov); Right: Diagram shows the areas where particles with different sizes can be deposited in the body[13].

Bioaerosol is a common type of PM of biological origin. Bioaerosol can severely impact human health, including infectious diseases, acute toxic effects, and allergies. [14, 15] Since the beginning of 2020, the pandemic caused by coronavirus disease 2019 (COVID-19) has wreaked havoc across the globe. The results of several studies suggest that aerosols play a critical role in COVID-19 transmission [16-21]. COVID-19 is not the only virus that can be transmitted through aerosols – the influenza virus, systemic sclerosis, and many others can also be spread through aerosols [20, 22-25].

1.3 Aerosol Monitoring with the PM Sensor Network

The direct measurement of time- and size-resolved PM concentrations is essential to health-related applications, such as exposure assessments and air quality (AQ) studies but challenging to implement at fine spatial and temporal scales. PM concentrations vary

significantly in space and time across community settings [26, 27]. Hence, time- and size-resolved PM measurements are more informative than traditional total PM weight measurements for assessing adverse health effects. As part of the Clean Air Act, the National Ambient Air Quality Standard (NAAQS) set by the U.S. Environmental Protection Agency (EPA) has adopted and established monitoring requirements for pollutants, including $PM_{2.5}$ and PM_{10} [28, 29]. However, the sparse spatial distribution of government monitoring sites makes fine spatial scale exposure assessment challenging [7]. Traditional PM instruments are large and expensive, thus have limited use in high spatial and temporal resolution mapping applications; these applications instead demand compact, low-cost sensors with reliable performance.

Low-cost particulate matter (PM) sensors find increasing use in various applications, including monitoring AQ in the outdoor [30-33] and indoor environment [34-36] by academic researchers and citizen scientists. The low-cost sensor networks have the potential to provide high spatial and temporal and resolution, identifying pollution sources and hotspots, which in turn can lead to the development of intervention strategies for exposure assessment and intervention strategies for susceptible individuals.

Controlling air pollution reduces adverse health effects and increases general well-being, quality of life, and improves public health. Accurate air quality information is critical for the public, especially the vulnerable groups, to make informative decisions to protect themselves from harmful air pollution. Historically, the public relies on regulatory monitoring network sites to get air quality information. Fixed-site monitors can generate population-level exposure estimates; however, they lack special-temporal resolution. Time-resolved exposure data from wearable monitors can be used to assess individual exposure in near real-time [37]. Individuals constantly move in time and space, while the air pollution landscape is highly variable at the

same time. Monitoring personal exposure provides insights into individual health risks, promoting more effective personalized interventions. In addition, personal monitoring provides a clearer picture of indoor air quality, which is essential since people spend a large part of their time in indoor environments.[38] The feasibility of personal monitoring / indoor monitoring with low-cost sensors has been demonstrated in several studies [39-41].

1.4 WILDFIRE SMOKE EXPOSURE MONITORING

Climate-change-related wildfires have become more frequent and intense in the Western United States. Summer wildfire seasons are already 40 to 80 days longer on average than they were 30 years ago [42]. Evidence suggests that dry mountain forests in California and other Western states will likely see ever-worsening fires for the coming century due to climate change and land management choices [43-45]. The intensified wildfires can release more smoke into the atmosphere [46]. Fine particulate matter ($PM_{2.5}$), a major pollutant found in smoke from wildfires, can penetrate deep into the respiratory tract [47]. Those combustion-generated aerosols consist of elemental carbon and organic carbon fraction linked to high PM toxicity [48]. Complex flow structures associated with large-scale flames and low flame temperature in biomass burning and wildfires lead to low carbonization of organic carbon, thus high levels of polycyclic hydrocarbons (PAHs) [49-52]. Exposure to these PAH compounds can lead to acute and chronic conditions, neurological diseases, and cancer.

As a recent example, a series of large wildfires impacted air quality in western regions of the United States in 2020. The episode measured in this study (2020 Washington Labor Day fires) began on September 7, 2020, and were 90% contained by September 22. The fires burned over 41000 acres of forest.[53] Due to the coronavirus pandemic 2019 (COVID-19) shelter-in-place order by Washington state since early 2020, people probably spent a significant amount of

time indoor during the 2020 wildfire season. Current public health advice for protection from smoke exposure during wildfires is to stay indoors, preferably in a "clean room" with filtered air, close windows and doors, and minimize physical exertion. However, studies have shown that $PM_{2.5}$ could penetrate indoors even with all the windows and doors closed [54, 55]. With limited access to portable air cleaners during wildfires and increasing awareness of the health impacts from wildfire smoke exposure, monitoring the indoor $PM_{2.5}$ is critical to understand the wildfire smoke preparedness of each household.

The demonstration study presented in Chapter 2 Section 2.2 assesses the feasibility of using low-cost sensors during wildfire smoke episodes to measure indoor vs. outdoor PM concentrations and the use of wearable sensors for personal monitoring. We demonstrated calibration of low-cost sensors to regional air quality monitoring data during wildfire episodes, the feasibility of quantifying key metrics, such as indoor/outdoor (I/O) $PM_{2.5}$ ratios, computing differences between wearable monitor and fixed location concentration in the microenvironments. We observed the effects of household interventions in several homes and discussed the potential for these capabilities to inform future studies.

1.5 Aerosol Archival Sampling

Aerosol sampling and identification are used to assess and control PM pollution, airborne pathogens, allergens, and toxins and their effect on air quality, human health, and climate change. Based on the application scenarios, aerosol samplers can be classified into area samplers and personal exposure samplers. Area samplers typically operate at high flow rates greater than 10 L/min to collect particles onto a solid substrate, onto a filter media, or into a liquid volume. Due to the high operating flow rate, area samplers often require powerful vacuum pumps, which

reduces the samplers' portability. Active personal aerosol samplers operate at lower flow rates and typically collect particles onto a filter media or a solid substrate. With the increasing concern regarding the potential health impacts of air pollution, substantial efforts have been made by many researchers to design more effective personal aerosol samplers (e.g., Foat, et al. [56], Schmechel, et al. [57], Willeke, et al. [58]).

Filters and solid substrates are two traditional media used in personal samplers. Most personal exposure samplers use filters to collect airborne particulates due to their broad target particle size range and high collection efficiency. However, high elution volumes, cumbersome sampling setups, high power consumption, and the required sample preparation procedures limit the usability of filter collection in many scenarios. Solid substrate collectors, such as cyclone and inertial impactors, rely on the momentum difference between airborne particulates and air molecules to collect aerosol particles onto a solid surface. Inertial impactors have been used to collect and measure aerosol particles since the end of the 19th century [59]. Airstream carrying particulates is accelerated through a nozzle and directed toward the impaction/collection surface. The flow is diverted at an angle, and the particles whose momentum exceeds a specific value cannot follow the streamline and impact the surface. The particle size that distinguishes between collision and non-collision is the cut-off size for a particular geometry and a flow rate. The cut-off size of an inertial impactor depends on many factors, such as the air stream flow rate, nozzle-to-plate distance, surface conditions, nozzle geometry, and shape of the impaction plate. Theoretical study of the inertial impactor [60] describes how each factor in the geometry influences the particle cut-off size. Several modifications have been found to improve the performance of inertial impactors. For example, increasing nozzle diameter to impaction distance ratio [61] improves collection efficiency. However, this increases the pressure drop of the

impactor, leading to higher power consumption. One study showed that by cooling the impaction plate, a higher collection efficiency could be achieved [62], and electrophoretic force can enhance the collection efficiency of charged aerosol particles [63]; both of these methods require additional hardware that complicates the overall design. Other proposed methods require modification of the impaction plate. It was found that coating the impaction plate with vacuum grease can increase the collection efficiency [64]. Increased surface roughness reduces the cut-off size but flattens the collection efficiency curve [65]. Several concave shapes of the impaction plate were investigated, and it was found that the concave shapes can increase collection efficiency under heavy loading conditions [66].

Growing numbers of personal exposure samplers have been developed, which are essential for gathering personal exposure information and studying the potential health impact of air pollution at the individual level. The Button Personal Inhalable Sampler (SKC, Inc., eighty-four, PA) is a widely used personal aerosol sampler that uses the filter as the collecting media and requires a powerful pump to compensate for the high-pressure drop filter. Small scall bioaerosol collector miniaturizing the wet scrubber technology has been recently reported [67]. Novosselov, et al. [68] utilize aggressively bent micro-channel using centrifugal forces to collect the particles on the channel walls. The microchannel collector has a relatively low-pressure drop; however, its collection area along the collection channel is relatively large (about 100 mm^2), which is not optimal for in-situ optical analysis. The collector requires subsequent elution to analyze the sample with a volume of about 100 microliters.

Aerodynamic focusing of the particles is often used to achieve a collimated particle beam, particularly for increasing particle concentration. Most common aerodynamic lenses (ADL) consist of a series of orifices of decreasing size through which a dilute aerosol is

aspirated. For laminar flow conditions, as the gas flows through the series of orifices, the fluid flow forces particles greater than a specific Stokes number into a narrow beam along the centerline, while the majority of the gas flow away from the centerline is left virtually free of particles [69]. In its original form (see Liu, et al. [70] and Liu, et al. [71]) and in the majority of ADLs in use today, the ADL is used alone without a virtual impactor. The aerosol is aspirated from the atmosphere through a pressure limiting orifice which reduces the flow operating pressure to a few hundred Pascals. This pressure range is beneficial for detection systems operating at low pressure, such as mass spectrometers (see Ziemann, et al. [72], Schreiner, et al. [73], Shu, et al. [74]) and other single-particle analyzers (e.g., Benner, et al. [75], Park, et al. [76]). It has also been shown that ADLs can be operated at higher pressures (Schreiner, et al. [77], Lee, et al. [78] and Deng, et al. [79]). Atmospheric pressure cylindrical ADLs are limited by turbulent transition for the higher flow rates and larger orifice dimensions leading to turbulent particle dispersion. The rectangular geometry of the ADL provides a solution for higher flow rate devices limiting the Reynolds number by adjusting the width of the lens to achieve the higher flow rate (see Novosselov and Ariessohn [80]). For relatively low flow rates (up to about 2 slpm at atmospheric pressure), the cylindrical aerodynamic focusing (AF) inlet falls into the laminar flow regime desirable for particle concentration.

Chapter 3, Section 3.1 presents the development and experimental validation of an aerosol collection cartridge consisting of an AF inlet and a μ-well trap for particles in the 0.5-3 μm size range. The device collects the aerosol sample within the submillimeter region, compatible with in-situ optical analysis and low sample elution volume. The geometry is chosen based on iterative CFD modeling and experiments. The paper first presents a computational

study of the aerodynamic inlet geometry and the µ-well collector, followed by experimental validation of the most suitable design and non-dimensional analysis of the collector performance.

Chapter 3, Section 3.2 presents the performance of the low-cost µ-well aerosol collection cartridge designed for use with the personal exposure monitor. The cartridge's performance is validated in laboratory studies using aerosolized single-organism Bacillus subtilis spores based on comparison with the collection and analysis of the reference filters. Sample recovery for the pipette elution is tested for elution in the 10-20 µl liquid volume.

1.6 Chemical Composition Analysis of Combustion-Generated Aerosols Using Excitation Emission Matrix (EEM)

Combustion-generated ultrafine particles (UFP) consist of elemental carbon (EC) and organic carbon (OC). Brown carbon (BrC), characterized by a significant fraction of OC, is a major air pollution component with known health risks [81] and adverse environmental impacts [82]. Though the severity and mortality of many diseases have been linked to UFP exposure, there is uncertainty about specific causative agents' influence. Size distributions, particle morphologies, optical properties, and chemical compositions of these aerosols vary significantly [26, 27]. The UFP chemical composition determines the potential for biochemical reactions with tissue and cells. BrC forms from the incomplete combustion of fossil, biomass, and other carbonaceous fuels. More than 100 polycyclic aromatic hydrocarbons (PAHs) cluster together to form liquid-like particles [83]. The planar nature and inherent stability of aromatic compounds are linked to the formation of soot particles [84, 85]. Molecular dynamics simulations have approximated the size of PAHs in young soot to be between four rings (Pyrene) and 19 rings (circumcoronene) [86, 87]. The PAHs participating in PM formation or components condensed

on PM during the secondary growth [52, 88] can be oxidized in the flame [49]; however, a significant organic fraction is retained by the particle, especially in the low temperature (incomplete) combustion [50].

Total organic carbon (TOC) is an established method for estimating the PM samples' organic fraction [89, 90]; though the organic fraction in BrC contains a variety of complex hydrocarbon compounds[49, 91], PAHs have been reported to be a major cause of oxidative damage [92-94]. The United States Environmental Protection Agency (EPA) has established a panel of 16 PAH compounds as priority pollutants representing a range of molecular structures with MW=128- 278 g/mol. More recent reports [97] suggest larger PAH molecules' more significant carcinogenic impact [98]. Targeted PAH analysis is typically performed by laboratory methods such as GCMS and LCMS. Both techniques are labor-intensive, require expensive equipment, and require several hours for analysis even after solvent extraction of target compounds from PM (~$100/sample).

PAHs are excellent candidates for analysis by spectroscopic techniques as they have high absorption coefficients and quantum yields [99]. While fluorescence spectroscopy is very sensitive (~1 ng/mL) for PAH detection [92-94], by itself, it is not specific. The UV–visible electronic transitions in sp^2 carbon systems such as PAHs rely on $\pi*–\pi$ transitions. Studies show an inverse power law relationship between the optical band gap (OBG) and the number of benzene rings in PAHs. An increase in MW of PAHs broadens their absorption bands towards longer wavelengths and red-shifts their emission bands due to the decreasing OBG. This variation in spectral properties as a function of MW can distinguish PAH content in combustion aerosols.

One group of particulate-bound chemical components of health concern is reactive oxygen species (ROS). A clear set of mechanisms explaining the linkage between particle mass and adverse health effects has not been established. However, it has been hypothesized that one possible contributing physiological route is a particle's ability to induce oxidative stress via the generation of ROS. The ability of a particle to generate ROS is referred to as oxidative potential (OP). The presence and formation of ROS in the human body overcome antioxidant defenses [95, 96]. Because of the link between PM and oxidative stress, various methods have been developed to measure the oxidative potential of ambient PM [100-102]. The redox-specific chemicals such as transition metals and PAHs have been measured for assessing PM oxidative activity [103]. The dithiothreitol (DTT)-based chemical activity assay is the most widely used technique to assess OP of PM [107].

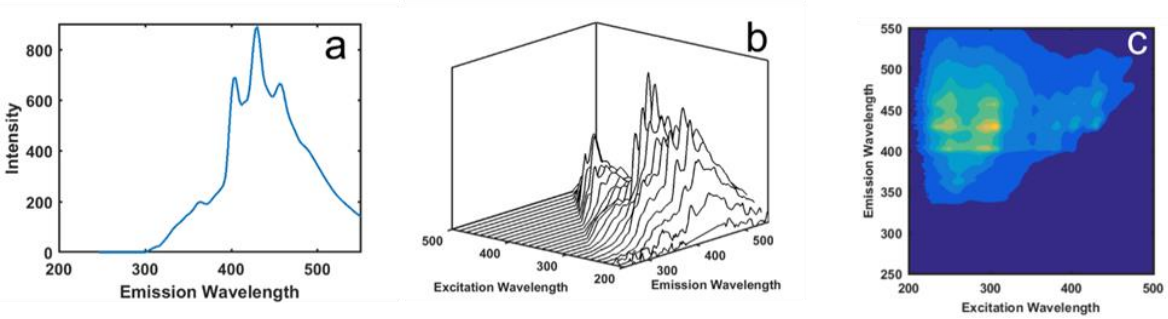

Figure 1.3. EEM spectroscopy. (a) Individual fluorescence emission spectrum is collected, (b) the excitation wavelength is incremented, and additional spectra are collected, (c) The EEM fingerprint is represented using a filled contour plot.

Excitation Emission Matrix (EEM) introduces an orthogonal dimension to the standard fluorescence analysis by scanning over a range of single-wavelength-excitations and stacking fluorescence emissions at each excitation wavelength, which provides a three-dimensional (3D) spectral fingerprint (see Figure 1.3). In this 3D matrix, fluorescence red-shifts for higher molecular weights of OC compounds. This variation allows to further differentiate the types of compounds in a complex mixture with overlapping individual spectra. EEM has been previously

used for the analysis of combustion PM [108-111]. The challenges of deconvolving the overlapping peaks can be addressed by data-driven techniques[50, 112].

Chapter 4 investigates the correlation between EEM signatures and ROS measurements for smoke aerosols. PM samples collected from cookstoves and wildfire smoke were analyzed by EEM and the dithiothreitol (DTT) assay for OP. The results show that the fluorescence EEM spectra correlate with ROS level in PM, suggesting that EEM can be an alternative method to evaluate the ROS level in combustion-generated aerosols.

Chapter 2. AEROSOL MONITORING USING SENSOR NETWORK

2.1 Assessing the Value of Complex Refractive Index and Particle Density for Calibration of Low-Cost Particulate Matter Sensor for Size-Resolved Particle Count and $PM_{2.5}$ Measurements

Commercially available low-cost PM sensors provide output as total or size-specific particle counts and mass concentrations. These quantities are not measured directly but are estimated by the original equipment manufacturers' (OEM) proprietary algorithms and have inherent limitations because particle scattering depends on the particles' composition, size, shape, and complex index of refraction (CRI). Therefore, there is a need to characterize and calibrate their performance under a controlled environment. We present calibration algorithms for Plantower PMS A003 PM sensor as a function of particle size and concentration. A standardized experimental protocol was used to control the PM concentration, environmental conditions and to evaluate sensor-to-sensor reproducibility. The calibration was based on tests when PMS A003 sensors were exposed to different polydisperse standardized testing aerosols. The results suggest particle size distribution from PMS A003 sensor was shifted compared to reference instrument measures. For calibration of number concentration, the linear model without adjusting aerosol properties, including CRI and relative humidity (RH), corrects the raw PMS A003 sensor measurement for a specific size bin with normalized mean absolute error within 4.0% of the reference instrument. Although the Bayesian Information Criterion (BIC) suggests superiority for the models adjusting for particle CRI and RH, they should be used with caution as the particle properties used in this study are within a narrow range for challenge aerosols. The calibration models adjusted for particle CRI and density account for non-linearity in the OEM's

mass concentrations estimates and demonstrated lower error. These results have significant implications for using PMS A003 sensor in high concentration environments, including indoor air quality monitoring, occupational/industrial exposure assessments, wildfire smoke, or near-source monitoring scenarios.

The work was published online in Arxiv [113] and submitted for publication in PlosOne. The authors are Ching-Hsuan Huang, Jiayang He, Elena Austin, Edmund Seto, Igor Novosselov. This work was done under the supervision of Professors Igor Novosselov, Edmund Seto, Elena Austin. Ching-Hsuan Huang, Jiayang He, Edmund Seto, Elena Austin, and Igor Novosselov conceptualized and designed the experiments. Ching-Hsuan Huang and Jiayang He performed the experiments. Ching-Hsuan Huang analyzed and visualized the data. Ching-Hsuan Huang and Jiayang He drafted the manuscript. Edmund Seto, Elena Austin, and Igor Novosselov reviewed, edited, and approved the final version of the manuscript. The calibration methodology and experimental results are presented here for completeness.

2.1.1 *Materials and Methods for PM Sensor Calibration*

2.1.1.1 Plantower PMS A003 and Sensor Test Platform

The low-cost sensor PMS A003 was evaluated. A sensor's photodiode positioned normal to the excitation beam measures the light scattered by the particles in the optical volume. The scattering light intensity is then converted to a voltage signal to estimate PM number density and mass concentration using a proprietary calibration algorithm. The PMS provides estimated particle counts in six size bins with the optical diameter in 0.3-10 μm (#/0.1L) range and mass concentration ($\mu g/m^3$) for PM_1, $PM_{2.5}$, and PM_{10}. PMS reports the mass concentrations for two conditions: "standard" and "atmospheric", which changes the assumed particle density. The standard condition is designed to be used in specific environments, such as an industrial setting.

The "atmospheric" condition has been tuned to measure particles commonly found in the ambient environment.

Six PMS units were installed on a custom printed circuit board (PCB), which also included a Bosch BME680 temperature and relative humidity (RH) sensor (Figure 2.1). All sensors were connected to an Arduino Nano microcontroller through a data selector (multiplexer NXP 74HC4051 breakout board, Sparkfun, Boulder, CO). The controller collects data from the six PMS sensors and an RH and temperature sensor simultaneously with the data acquisition rate of 1 Hz. The data reported in the "standard " condition was used in the analysis.

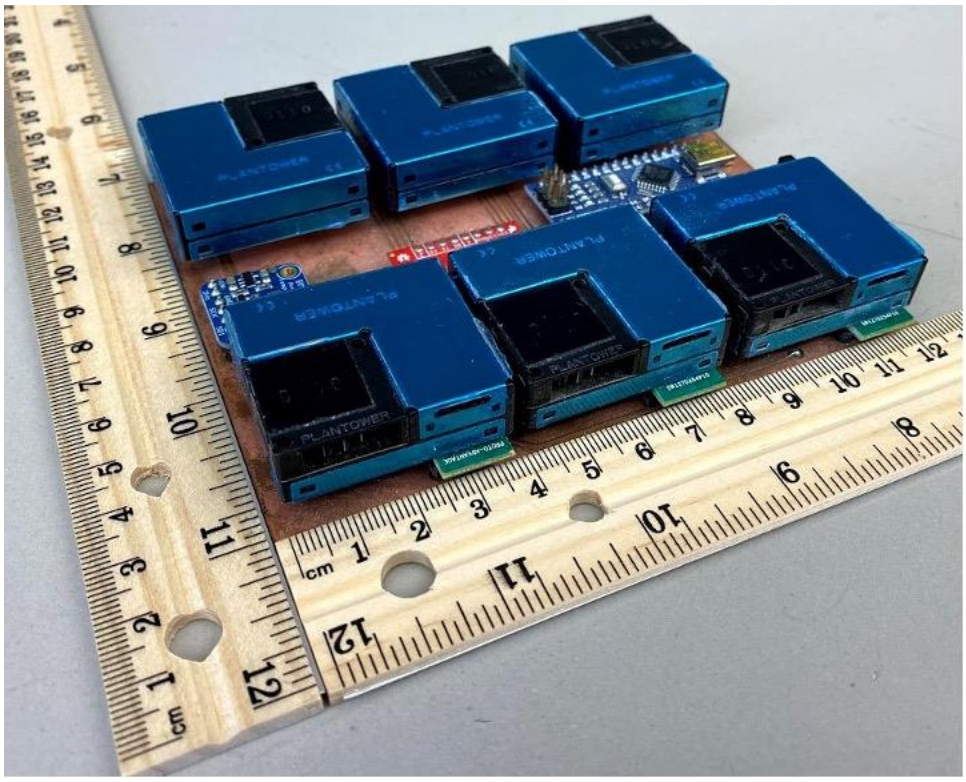

Figure 2.1. Photograph of the testing platform, consisting of six PMS units mounted on the PCB with a temperature and humidity sensor, a multiplexer, and an Arduino microcontroller.

The reference instrument of the experiment was the TSI Aerodynamic Particle Sizer (APS) Spectrometer 3321. Using the time-of-flight principle, APS measures real-time size-resolved particle counts with aerodynamic particle diameters ranging from 0.523 to 20 µm in 52

size bins. Particles smaller than 0.523 μm can be detected by the APS's optical sensor; however, their aerodynamic sizes were not resolved. The instrument estimates mass concentration by assuming spherical particles and setting particle density values. During the experiments, APS continuously measured particle concentrations with a 5-second temporal resolution, the sampling inlet was placed near the PMS sensors. The total number concentration of the aerosols in the experiments was maintained below 1000 #/cc (105 #/0.1L) to minimize the coincidence error in the APS measurement specified in the instrument's user manual.

2.1.1.2 Aerosol Chamber Tests

We tested four polydisperse aerosols in a custom-built aerosol chamber. The four aerosols are Arizona Test Dust (ATD) (Powder Technology Incorporated, Arden Hills, MN), polydisperse W210, and W410 ceramic particles (3M™, St. Paul, MN), and sodium chloride (NaCl) particles. NaCl particles were generated by nebulizing the aqueous solution of 10% wt [114]. The other aerosols were nebulized from powder form. The properties and typical size distributions of these aerosols are summarized in

Table 2.1. Figure 2.2 shows the aerosol chamber (0.56 m × 0.52 m × 0.42 m) used in this study. A full description of the chamber can be found in the reference [115]. The PMS sensor platform was placed in the well-mixed aerosol test chamber, elevated to the same height as the APS inlet. The APS sampled particle-laden air through static-dissipative tubing to eliminate electrostatic losses in the tubing. Particles were generated using a medical nebulizer (MADA Up-Mist Medication Nebulizer) [116]. During the experiments, the RH was controlled by nebulizing deionized water using a separate nebulizer or introducing dry filtered air; tests were conducted in the range of RH = 17% - 80%. Two mixing fans inside the chamber provided well-mixed conditions through the experiments; particle concentration was continuously monitored.

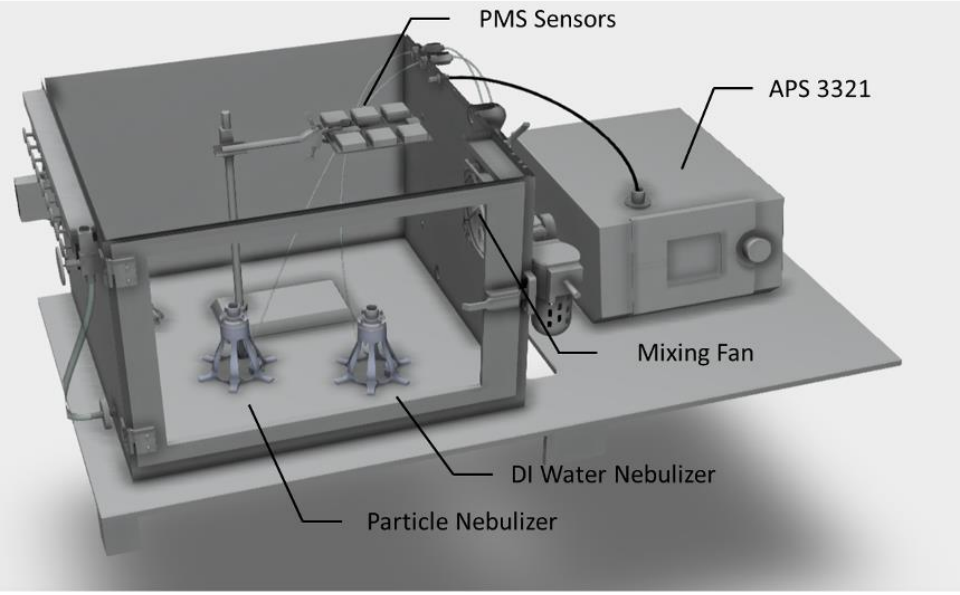

Figure 2.2. 3-D diagram of the experimental setup used for the PMS sensor calibration with the lid of the aerosol chamber removed.

Table 2.1. Characteristics of the standard testing aerosols used in the study [117].

Aerosol	ATD	W210	W410	NaCl
Composition	SiO_2, Al_2O_3, Fe_2O_3, Na_2O [a]	Alkali aluminosilicate ceramic	Alkali aluminosilicate ceramic	Sodium Chloride
Assumed density (g/cm^3)	2.5 – 2.7 [b]	2.4	2.4	1.03
CRI	1.63	1.53	1.53	1.54

[a] Four major components were listed.
[b] For analysis purposes, 2.6 g/cm3 was used.
Definition of abbreviations: ATD = Arizona Test Dust

We controlled the aerosol generation rate by adjusting the compressed air flow rate to the nebulizer. The aerosol generation was stopped when the total number concentration (based on the APS count) reached 1000 #/cm3. Then, the particle concentration was allowed to decay as the chamber was evacuated at a rate of 9.8 L/min; the make-up air entering the test is aspirated through a HEPA filter. The sensor array data and the APS data were acquired via two universal serial bus (USB) cables in real-time until the total number concentration from the APS reached 15 #/cm^3.

2.1.1.3 Data Analysis and Modeling

The data outside the measurement range of the APS was removed. The number concentration reported by the APS was aggregated as summarized in Table 2.2 to match the cumulative number concentrations of the PMS. The 1-second PMS measurement and 5-second APS measurement were aggregated to obtain 1-minute averaged data for calibration. The smallest size bin of the APS (< 0.523 μm) was used as a reference for calibrating PMS size bin > 0.3 μm.

Table 2.2. The PMS size bins and mass indices with the corresponding reference APS size bins for calibration.

PMS indices	Reference APS indices
Number concentration	
> 0.3 μm	aggregated from all size bins (< 0.523 μm and 0.542 – 19.81 μm)
> 0.5 μm	aggregated from size bins 0.542 – 19.81 μm
> 1 μm	aggregated from size bins 1.037 – 19.81 μm
> 2.5 μm	aggregated from size bins 2.642 – 19.81 μm
> 5 μm	aggregated from size bins 5.048 – 19.81 μm
> 10 μm	aggregated from size bins 10.37 – 19.81 μm
Mass concentration	
PM_1	mass aggregated from size bin < 0.523 μm – 0.965 μm
$PM_{2.5}$	mass aggregated from size bin < 0.523 μm – 2.458 μm
PM_{10}	mass aggregated from size bin < 0.523 μm – 9.647 μm

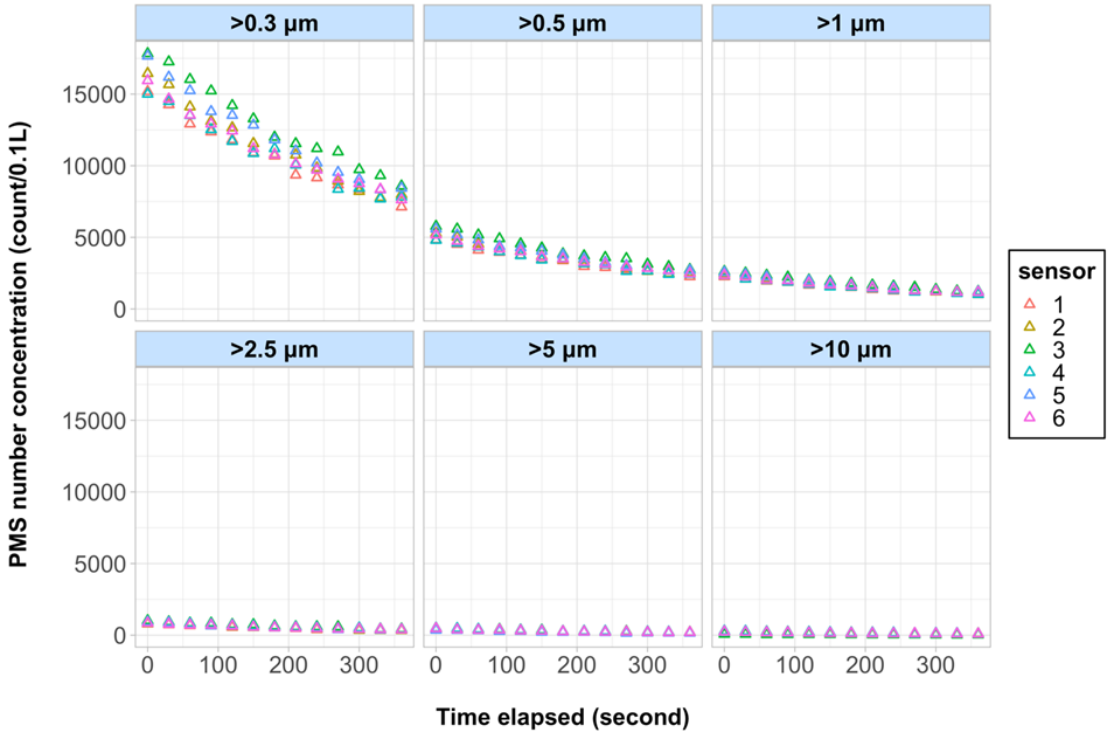

Figure 2.3. Time-series plots of the uncalibrated, 1-second number concentration measurement from the six PMS sensors during an experiment conducted under 30% RH with W210 aerosols.

Figure 2.3 shows the data from 6 PMS sensors during one experiment. In all experiments, the time-series of the uncalibrated concentration measurements from the six PMS sensors were consistent for all size bins with Pearson correlation coefficient > 0.98 for both number concentration and mass concentration. Figure 2.4 shows Dp>0.3 size bin for number concentration and PM_1 for mass concentration as examples. Pearson correlation plots for other size bins are similar to Figure 2.4. The cross-unit similarity allowed us to develop generalized models by fusing the readings from six sensors and correlating the data against the APS measurement with matching time stamps for each size bin. For number concentration. Calibrations models of the following form were fit separately for number concentration data from the APS and PMS:

$$\mathbf{APS_t} = \boldsymbol{\beta_0} + \boldsymbol{\beta_1}\,\mathbf{PMS_t} + \boldsymbol{\varepsilon_t} \qquad (2.1)$$

where APS_t is the number concentration for aggregated APS size bins at timestamp t; PMS_t is the linear term of the PMS measurement (the number concentration of each PMS size bin) at timestamp t; RH_t is the RH measurement of the Bosch BME680 sensor at timestamp t; β_0 and β_1 are regression coefficients; ε_t is the residual. In addition to equation (1), other forms of linear models adjusted for relative humidity, particle density, and CRI were also evaluated (see Table 2.3). For calibration of mass concentration, models including quadratic terms of the PMS measurement were evaluated (see Table 2.3). Since the test temperature variations were within ±2 °C, the temperature was not included as a variable in the models.

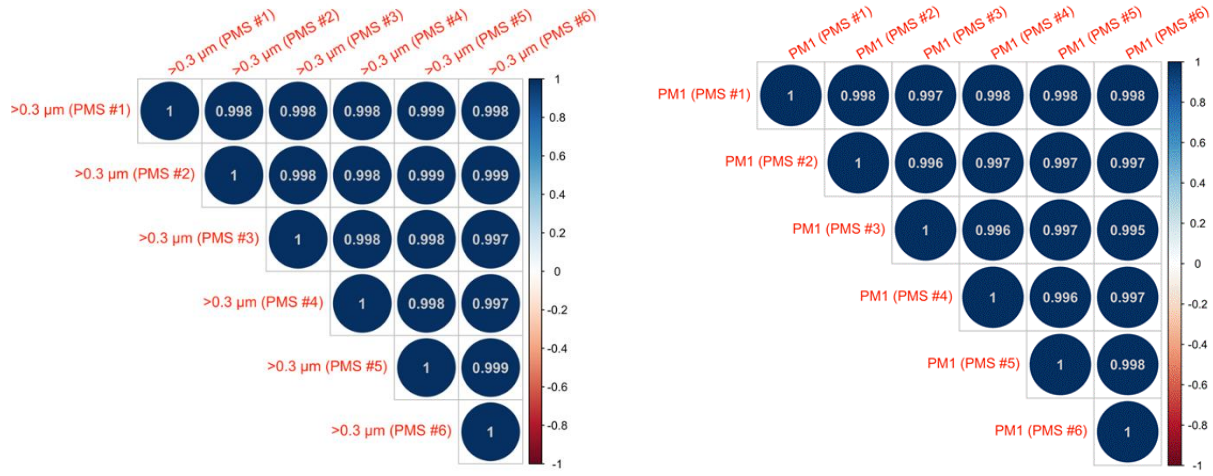

Figure 2.4. Pearson correlation between pairs of PMS for number and mass concentration.

We assumed that the PMS particle count and mass indices should be zero when the APS count is zero, the intercept (β_0) of the models was set to zero. The number of terms included in the optimal calibration model for each size bin was determined based on the Bayesian Information Criterion (BIC). The models with lower BIC were chosen as the optimal models. After identifying the optimal models using BIC and estimating model coefficients, the model was then applied to the pre-calibrated 1-minute PMS measurement to produce the post-calibrated concentrations for model evaluation. Calibration performance was assessed using the normalized mean absolute error (NMAE), which was calculated using the following equation [118]:

$$\mathbf{NMAE}\ (\%) = \frac{\mathbf{Mean}\left(\left|\mathbf{C_{PMS_{post-cal}}} - \mathbf{C_{APS}}\right|\right)}{\mathbf{Mean}(\mathbf{C_{APS}})} \qquad (2.2)$$

where $C_{PMS\_post-cal}$ is the post-calibrated 1-minute averaged PMS concentration, and C_{APS} is the 1-minute averaged APS concentration. The linear models were fitted using the *lm* function in R. All the analyses were conducted using R version 3.6.3.

Table 2.3. Forms of linear model fitted for number concentration and mass concentration for calibration.

Indices	Form of linear model	Equation
Number concentration	Linear	$APS_t = \beta_0 + \beta_1 PMS_t + \varepsilon_t$
	Linear + CRI	$APS_t = \beta_0 + \beta_1 PMS_t + \beta_2 CRI + \varepsilon_t$
	Linear + RH	$APS_t = \beta_0 + \beta_1 PMS_t + \beta_2 RH + \varepsilon_t$
	Linear + Density	$APS_t = \beta_0 + \beta_1 PMS_t + \beta_2 Density + \varepsilon_t$
	Linear + CRI + Density	$APS_t = \beta_0 + \beta_1 PMS_t + \beta_2 CRI + \beta_3 Density + \varepsilon_t$
	Linear + CRI + RH	$APS_t = \beta_0 + \beta_1 PMS_t + \beta_2 CRI + \beta_3 RH + \varepsilon_t$
Mass concentration	Linear	$APS_t = \beta_0 + \beta_1 PMS_t + \varepsilon_t$
	Linear + CRI	$APS_t = \beta_0 + \beta_1 PMS_t + \beta_2 CRI + \varepsilon_t$
	Linear + RH	$APS_t = \beta_0 + \beta_1 PMS_t + \beta_2 RH + \varepsilon_t$
	Linear + Density	$APS_t = \beta_0 + \beta_1 PMS_t + \beta_2 Density + \varepsilon_t$
	Linear + CRI + Density	$APS_t = \beta_0 + \beta_1 PMS_t + \beta_2 CRI + \beta_3 Density + \varepsilon_t$
	Linear + CRI + RH	$APS_t = \beta_0 + \beta_1 PMS_t + \beta_2 CRI + \beta_3 RH + \varepsilon_t$
	Polynomial	$APS_t = \beta_0 + \beta_1 PMS_t + \beta_2 PMS^2{}_t + \varepsilon_t$
	Polynomial + CRI	$APS_t = \beta_0 + \beta_1 PMS_t + \beta_2 PMS^2{}_t + \beta_3 CRI + \varepsilon_t$
	Polynomial + RH	$APS_t = \beta_0 + \beta_1 PMS_t + \beta_2 PMS^2{}_t + \beta_3 RH + \varepsilon_t$
	Polynomial + Density	$APS_t = \beta_0 + \beta_1 PMS_t + \beta_2 PMS^2{}_t + \beta_3 Density + \varepsilon_t$
	Polynomial + CRI + Density	$APS_t = \beta_0 + \beta_1 PMS_t + \beta_2 PMS^2{}_t + \beta_3 CRI + \beta_4 Density + \varepsilon_t$
	Polynomial + CRI + RH	$APS_t = \beta_0 + \beta_1 PMS_t + \beta_2 PMS^2{}_t + \beta_3 CRI + \beta_4 RH + \varepsilon_t$

2.1.2 *Results and Discussion for PM Sensor Calibration*

2.1.2.1 Experimental Conditions

During the experiments, the average temperature in the chamber was 24.8 ℃ (range: 23.2 to 26.6℃), the RH was varied in the range of 17.5 - 79.4%, all experiments were performed at atmospheric pressure conditions. The one-minute APS total number concentration averaged 237.9 #/cm^3 (range: 8.5 to 985.9 #/cm^3), the one-minute $PM_{2.5}$ measurement from the APS and

PMS before calibration (6 sensors pooled together) averaged 106.0 µg/m^3 (range: 1.9 to 641.3 µg/m^3) and 51.5 µg/m^3 (range: 0 to 218.8 µg/m^3), respectively.

2.1.2.2 Particle Size Distribution

The particle size distribution of each test aerosol by APS is shown in Figure 2.5. The NaCl particles (from the nebulized liquid solution) were the smallest among the test aerosols, with nearly all particles < 3 µm. The W410 mixture had slightly larger particles than W210 and had the same CRI as W210 [117].

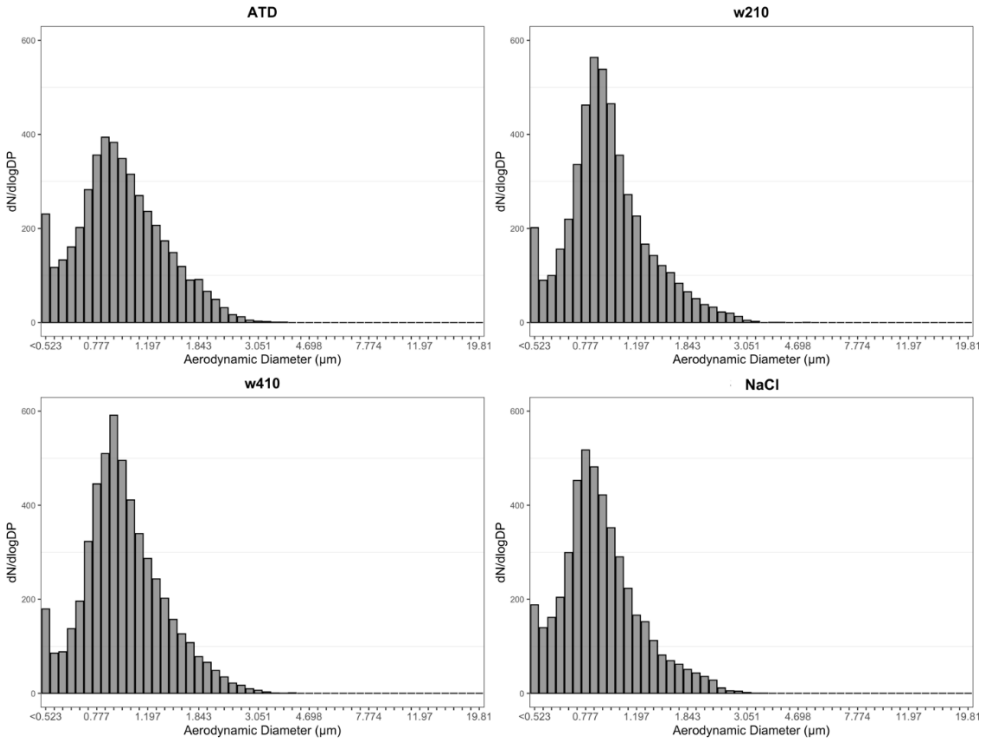

Figure 2.5. The normalized particle size distribution of the Arizona Test Dust (ATD), NaCl, W210, and W410 was measured by the APS. The median diameters of the ATD, saline, W210 and W410 aerosol are 0.94 µm, 0.86 µm, 0.92 µm, and 0.96 µm, respectively.

The normalized particle size distribution of each test aerosol measured by the APS and the PMS was aggregated into six different size bins, as shown in Figure 2.6. For W210 and

W410, which had similar particle size distribution, the PMS indicated a minor difference in their size bin distributions. W410 had a slightly higher fraction of particles classified into larger bins (2.5 – 5 µm and 5 –10 µm). For all aerosols and all tested concentrations, the PMS categorized some small fractions of particles into larger size bins (2.5–5 µm and 5–10 µm), which is not consistent with the APS measurements (Figure 2.6). Overall, the PMS appeared to underestimate particle counts for the size bin 0.5–1 µm and 1–2.5 µm by a factor of 0.9 and 0.7, respectively. For larger size bins (2.5–5 µm and 5–10 µm), the PMS significantly overestimate the particle counts by a factor of 6 to 34 and 786 to 2097, respectively. The PMS also overestimated the counts in the 0.3–0.5 µm size range compared to the APS (all particles <0.523 µm). PMS reflects the overall trends in particle size distribution; however, the absolute number concentration and particle sizing do not agree with the reference instrument. Thus, calibrations based on various aerosol types and environmental conditions are needed if PMS is used for PM concentration assessment.

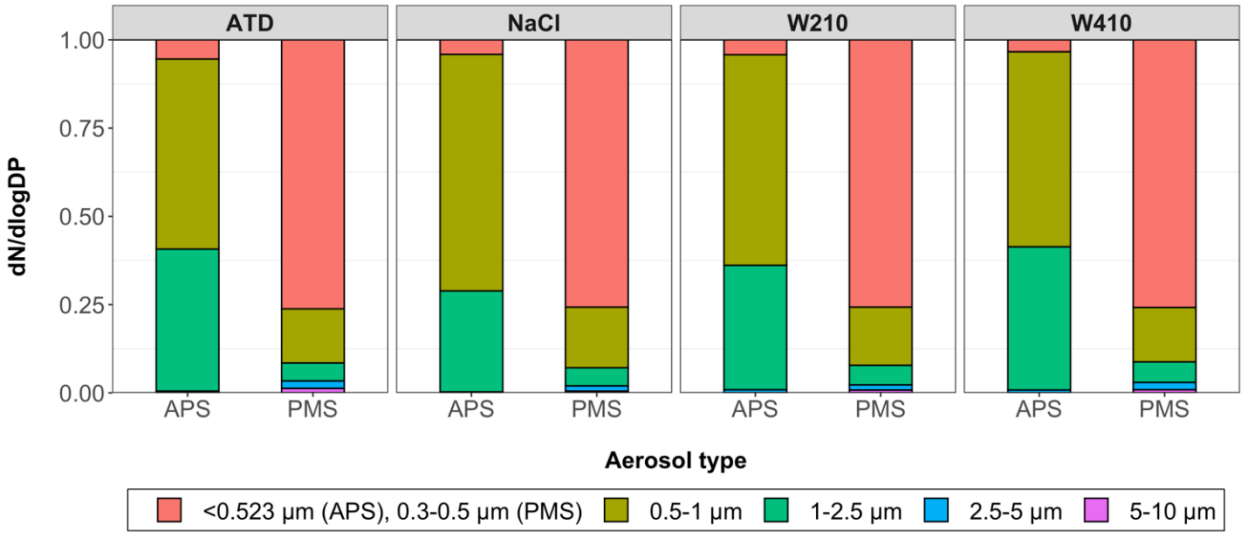

Figure 2.6. A comparison of the normalized size bin distribution measured by the PMS and APS before calibration. Typical data from one of the six PMS and APS experiments with ATD, NaCl, W210, and W410 particles 15 minutes after the aerosols were introduced into the chamber. APS data from bins is aggregated to reflect the size ranges reported by PMS.

2.1.2.3 Model Fit

Despite the apparent shift in size distribution in Figure 2.6, a matrix of Pearson correlations between the PMS number concentrations (before calibration) and the APS reference number concentrations for different size ranges suggests a good correlation between the matching size bins of the two instruments (Figure 2.7). Notably, the PMS number concentration data correlated well with the APS for size bin up to 2.5 µm ($r > 0.97$). For measurement of size bin larger than 2.5 µm, the PMS exhibited moderate correlation with the APS ($r < 0.78$). The worst correlation was observed for particles > 5 µm.

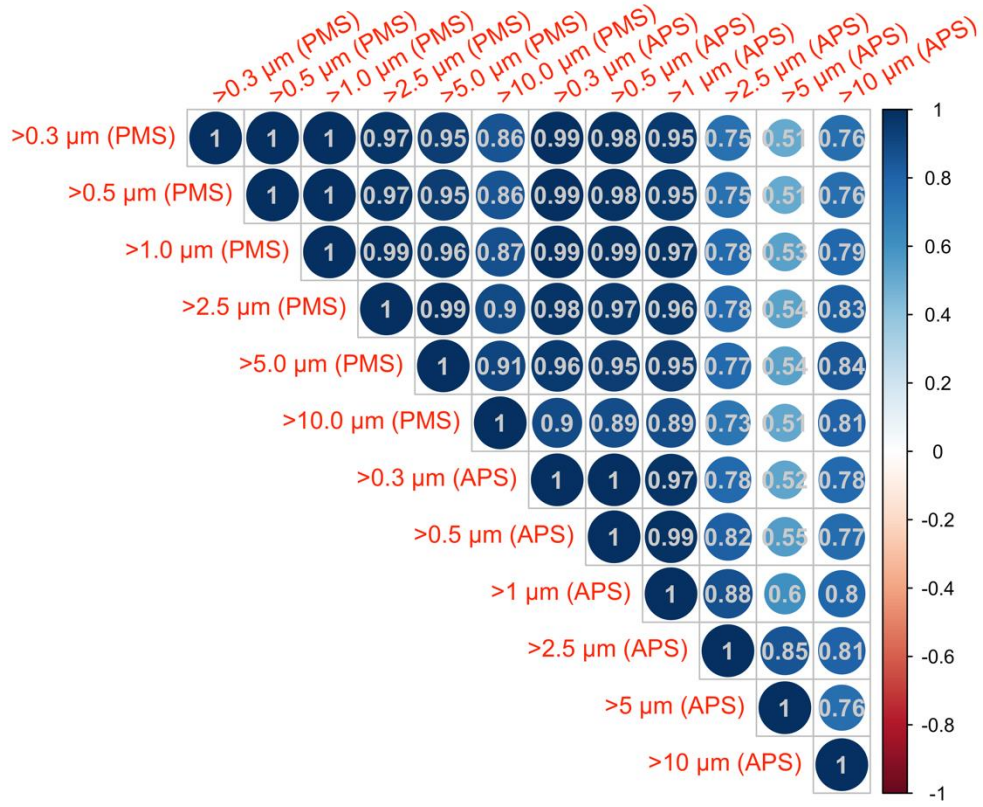

Figure 2.7. Pearson correlation between the uncalibrated PMS number concentration (6 sensors pooled together) and APS number concentration for different size ranges.

A similar Pearson correlation matrix comparing the mass concentrations measured by the pre-calibrated PMS and the APS for different particle size ranges suggests a good correlation

between matching sizes (Figure 2.8). The PM_1, $PM_{2.5}$, and PM_{10} measurements by the PMS all exhibited high correlations with their corresponding sizes measured by the APS (r >0.90).

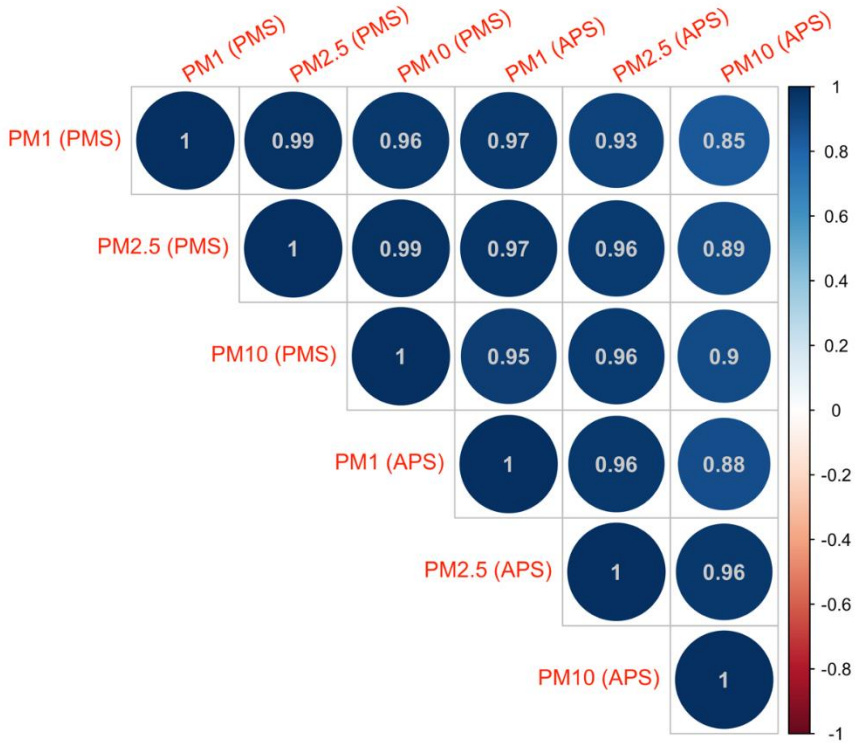

Figure 2.8. Pearson correlation between the uncalibrated PMS mass concentration (6 sensors pooled together) and APS mass concentration for different size ranges.

Because of the close correlations between corresponding APS and PMS size-specific measurements (Figure 2.7 and Figure 2.8), the sizes listed in Table 2 were chosen to develop calibration models for both PM number concentration and PM mass concentration. For example, APS size bin > 0.5 µm number concentrations was chosen as the reference (independent variable) for calibrating the PMS size bin > 0.5 µm number concentrations (dependent variable). Based on the same rationale, the corresponding APS mass concentration measurement was chosen as the reference for calibrating the PMS mass concentration index for mass concentrations. For example, APS $PM_{2.5}$ mass concentration was chosen as the reference (independent variable) for calibrating the PMS $PM_{2.5}$ mass concentration (dependent variable).

The assumed density for each testing aerosol in Table 2.1 was used to determine the APS mass concentration for the calibration of PMS. After fitting a set of alternative calibration model forms to the APS and PMS number concentration data, the results show excellent R^2 and low NMAE for >0.3 µm, >0.5 µm, and >1 µm size bins when the full range of concentrations from 0 – 1000 #/cm^3 was used for fitting (Table 2.4). However, the model performance was worse for larger size ranges, i.e., >2.5 µm, >5 µm, and >10 µm size bins. Based on the previous findings on the impacts of relative humidity on optical particle sensor output and particle optical properties, the models adjusted for CRI and RH were considered in addition to the linear model, see Table 2.4. Interestingly, for most size ranges, the relatively simple linear model without the CRI dependent term performed nearly as well as the models with the additional parameters. Although based on the BIC, the optimal models still included CRI and RH in some cases. The table also includes the performance of models based on the lower concentration data (data points with APS total number concentration <100 #/cm^3). These models do not perform as well even when applied to a lower range of particle concentrations. The summary of other number concentration models fitted in this study is included in the appendix of this dissertation (Table 6.1).

Table 2.4. Summary of the calibration model for number concentration, R^2, Bayesian information criterion (BIC), and the calibration model's normalized mean absolute error (NMAE).

Indices	Equation	Regression [a]	R^2	BIC	NMAE
Full concentration range (APS total number concentration 0 – 1000 #/ cm^3) (n = 4,134)					
>0.3 µm	Linear	y = 5.93 x	0.99	78723	2.20%
	Linear + CRI + RH	y = 6.00 x – 1090 CRI + 28.23 RH	0.99	78567	2.06%
>0.5 µm	Linear	y = 14.17 x	0.98	79716	2.92%
	Linear + CRI + RH	y = 14.40 x - 1434 CRI + 40.68 RH	0.98	79518	2.78%
>1 µm	Linear	y = 14.85 x	0.96	76002	2.88%
	Linear + CRI + RH	y = 14.98 x - 784.93 CRI + 26.40 RH	0.97	75884	2.89%
>2.5 µm	Linear	y = 2.20 x	0.66	62906	3.87%
	Linear + CRI + RH	y = 2.42 x - 156.71 CRI + 3.38 RH	0.68	62695	3.95%

>5 µm	Linear	y = 0.11 x	0.31	38958	2.71%
	Linear + CRI + RH	y = 0.14 x - 2.41 CRI - 0.06 RH	0.33	38848	2.83%
>10 µm	Linear	y = 0.11 x	0.70	8117	3.66%
	Linear + CRI + RH	y = 0.14 x - 2.41 CRI - 0.06 RH	0.71	8000	3.68%
Lower concentration range (APS total number concentration < 100 #/ cm^3) (n = 1,838)					
>0.3 µm	Linear	y = 4.84 x	0.97	30263	7.96%
	Linear + CRI + RH	y = 4.94 x - 358.12 CRI + 13.68 RH	0.97	30235	7.94%
>0.5 µm	Linear	y = 14.17 x	0.93	30285	10.39%
	Linear + CRI + RH	y = 10.83 x - 385.61 CRI + 18.91 RH	0.94	30234	10.23%
>1 µm	Linear	y = 14.85 x	0.92	26963	8.50%
	Linear + CRI + RH	y = 11.10 x - 105.04 CRI + 10.59 RH	0.93	26713	7.57%
>2.5 µm	Linear	y = 2.20 x	0.60	14298	7.73%
	Linear + CRI + RH	y = 0.45 x - 8.38 CRI + 0.48 RH	0.66	14018	7.22%
>5 µm	Linear	y = 0.11 x	0.35	-2612	11.52%
	Linear + CRI + RH	y = 0.003 x + 0.007 CRI + 0.002 RH	0.44	-2869	11.91%
>10 µm	Linear	y = 0.11 x	0.19	-5846	15.16%
	Linear + CRI + RH	y = 0.002 x + 0.003 CRI + 0.0003 RH	0.22	-5920	17.91%

[a] y: APS measurement; x: PMS measurement.
Definition of abbreviations: n = number of datapoints; CRI = complex index of refraction; RH = relative humidity; BIC = Bayesian information criteria; NMAE = normalized mean absolute error.

For fitting mass concentration data, an additional quadratic term was included, shown in Table 2.5. As with the number concentration models, restricting the mass concentration model to only lower concentrations resulted in worse performance than the entire concentration range. The optimal models include particle properties and environmental conditions (CRI, density, and RH). The improvements in NMAE for models with CRI, density, and RH terms compared to the relatively simple linear models without these added parameters tended to be larger than observed for the number concentration models. The summary of other mass concentration models fitted in this study is included in the appendix of this dissertation (Table 6.2).

Table 2.5. Summary of the calibration model for mass concentration a, R^2, Bayesian information criterion (BIC), and the calibration model's normalized mean absolute error (NMAE).

Indices	Equation	Regression [b]	R^2	BIC	NMAE

Full concentration range (APS total number concentration between 0 – 1000 #/ cm^3) (n = 4,134)					
PM_1	Linear	y = 1.06 x	0.96	25852	3.11%
	Polynomial	y = 0.76 x + 0.007 x^2	0.97	24480	2.41%
	Linear + CRI + density	y = 1.13 x + 13.88 CRI - 10.13 density	0.97	24181	2.84%
	Polynomial + CRI + density	y = 0.83 x + 0.01x^2 + 14.44 CRI - 9.58 density	0.98	23432	2.33%
$PM_{2.5}$	Linear	y = 2.29 x	0.94	42435	4.53%
	Polynomial	y = 1.55 x + 0.006 x^2	0.96	41341	3.41%
	Linear + CRI + RH	y = 2.51 x - 23.27 CRI + 0.36 RH	0.95	41565	4.07%
	Polynomial + CRI + RH	y = 1.80 x + 0.004 x^2 - 15.55 CRI + 0.42 RH	0.96	41152	3.44%
PM_{10}	Linear	y = 1.53 x	0.85	49963	3.56%
	Polynomial	y = 0.72 x - 0.003 x^2	0.88	48959	2.61%
	Linear + CRI + RH	y = 1.69 x - 39.14 CRI + 0.56 RH	0.87	49544	3.31%
	Polynomial + CRI + RH	y = 0.73 x + 0.003 x^2 - 17.94 CRI + 0.75 RH	0.88	48931	2.61%
Lower concentration range (APS total number concentration < 100 #/ cm^3) (n = 1,838)					
PM_1	Linear	y = 0.72 x	0.90	6211	10.10%
	Polynomial	y = 0.91 x - 0.02 x^2	0.91	6053	9.23%
	Linear + CRI + density	y = 0.57 x + 4.80 CRI - 2.68 density	0.93	5746	8.16%
	Polynomial + CRI + density	y = 0.80 x - 0.02 x^2 + 4.93 CRI - 2.95 density	0.93	5694	8.08%
$PM_{2.5}$	Linear	y = 1.10 x	0.91	11170	9.14%
	Polynomial	y = 1.34 x - 0.01 x^2	0.91	11087	8.80%
	Linear + CRI + RH	y = 0.97 x -1.87 CRI + 0.16 RH	0.92	10890	8.01%
	Polynomial + CRI + RH	y = 1.14 x - 0.006 x^2 - 2.43 CRI + 0.17 RH	0.92	10885	7.97%
PM_{10}	Linear	y = 0.63 x	0.89	11878	9.30%
	Polynomial	y = 0.86 x - 0.01 x^2	0.90	11686	8.53%
	Linear + CRI + RH	y = 0.54 x - 2.15 CRI + 0.20 RH	0.91	11627	8.01%
	Polynomial + CRI + RH	y = 0.78 x - 0.004 x^2 - 3.57 CRI + 0.21 RH	0.91	11461	7.75%

[a] APS mass concentration was obtained assuming aerosol densities mentioned in Table 2.1
[b] y: APS measurement; x: PMS measurement
Definition of abbreviations: n = number of datapoints; CRI = complex index of refraction; RH = relative humidity; BIC = Bayesian information criteria; NMAE = normalized mean absolute error.

Figure 2.9 shows a comparison between the pre-calibrated and post-calibrated PMS and APS particle number densities for full and lower concentration ranges. The pre-calibrated (OEM) number concentration vs. APS exhibits a linear trend over the entire range for all aerosols; however, the PMS underestimates the number of particles. The calibration significantly improves the agreement demonstrating the importance of calibration and the accuracy gains from applying

calibrations. The simple linear relationship shows excellent agreement over the entire range of particle concentration and properties, the fitting parameter are shown in Table 3.

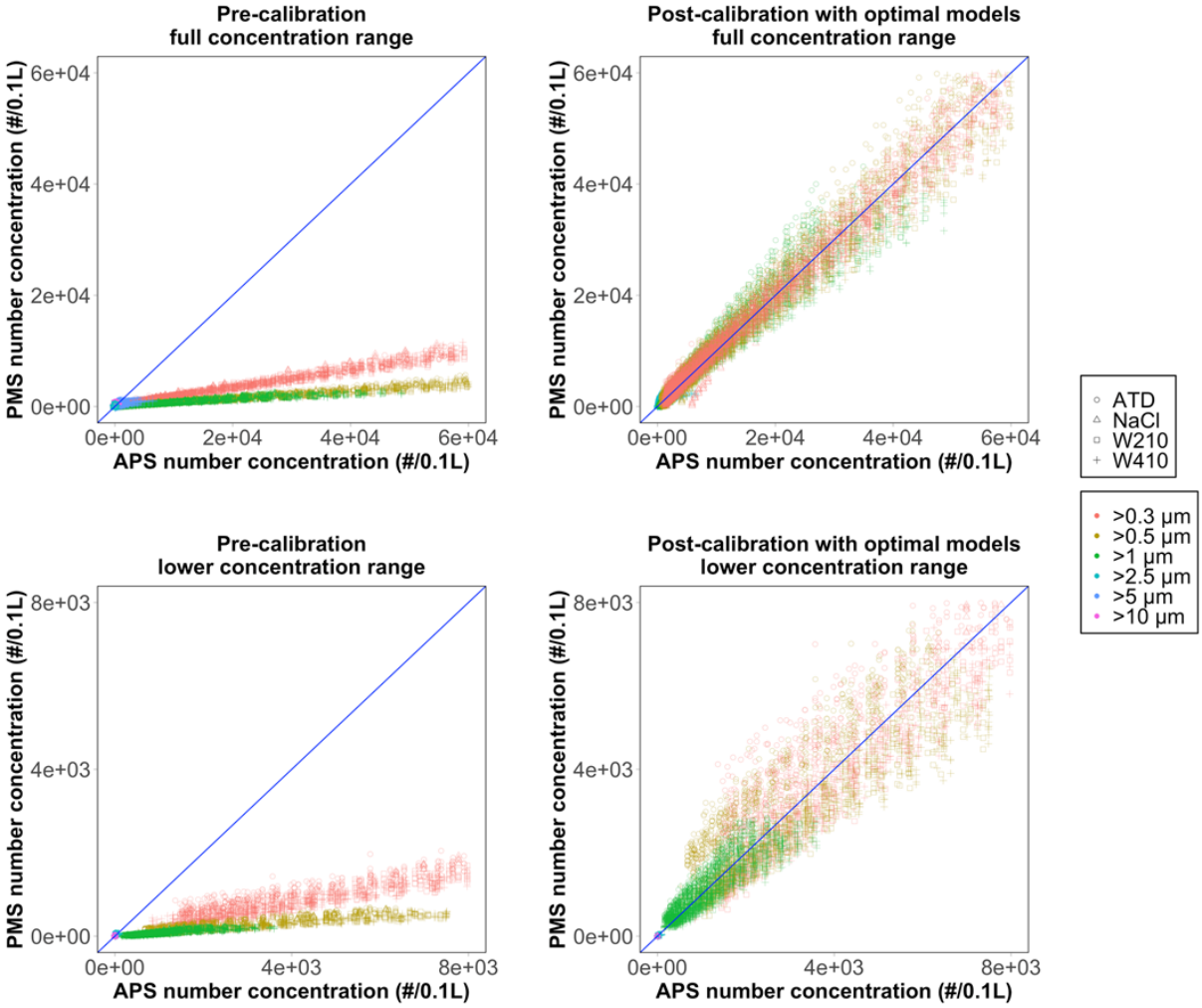

Figure 2.9. A comparison of the pre-calibrated and post-calibrated number concentration by full and lower concentration range. The blue line represents the 1:1 relationship between the PMS and APS concentration.

For mass concentration shown in Figure 2.10, the PMS mass concentration does not increase linearly, especially at higher concentrations. We do not have a satisfactory explanation for the non-linear trend when using the OEM calibration. Also, we observed a notable discrepancy in the PMS and APS relationship between ATD and other test aerosols, which may be related to a wide range of particle CRI in ATD. The graphical comparison is consistent with

our results from Table 4 that shows lower NMAE for the models with a quadratic term. Overall, the mass concentration models adjusted for particle and environmental specific properties such as CRI, density, RH, and adjustment for non-linearity, seem necessary.

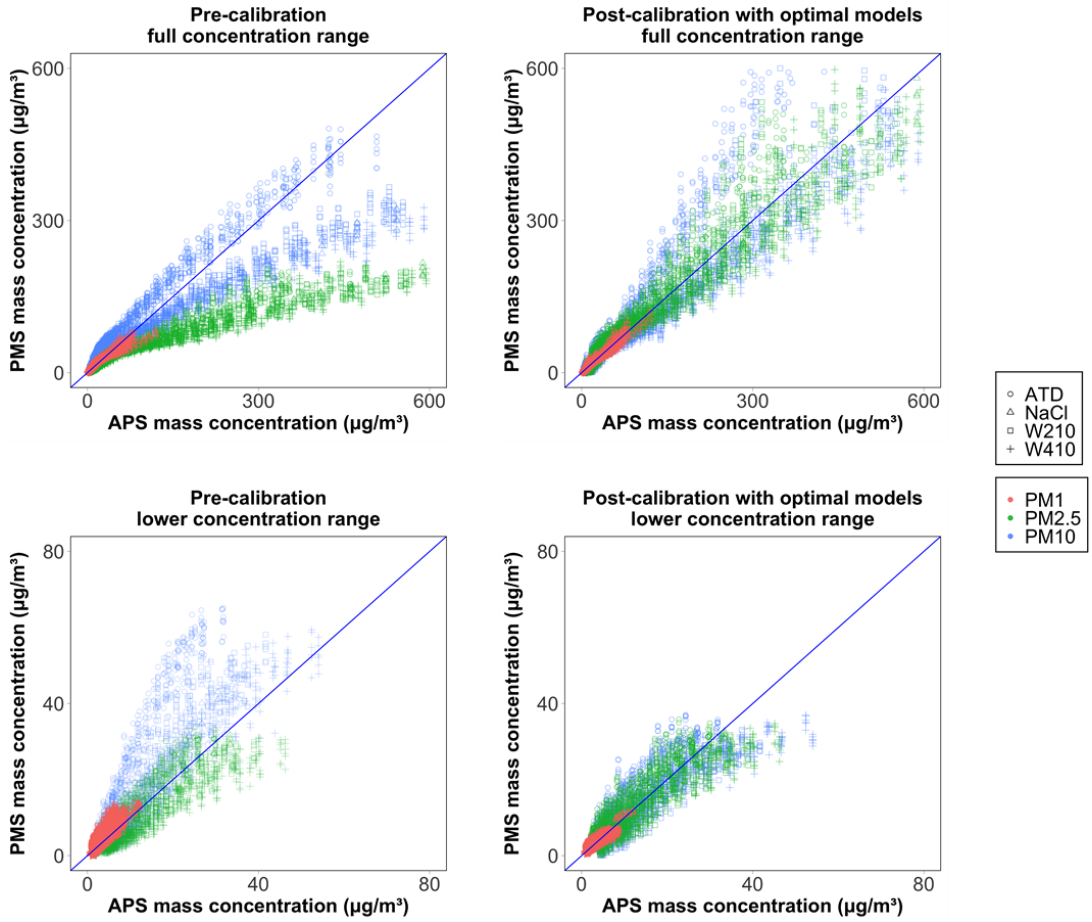

Figure 2.10. A comparison of the pre-calibrated and post-calibrated mass concentrations by full and lower concentration range. The blue line represents the 1:1 relationship between the PMS and APS concentration.

2.1.3 *Conclusions on PM Sensor Calibration*

This study evaluated the PMS sensors and reported the calibration algorithm for both number concentration and mass concentration. We found that the number concentrations can be corrected using a simple linear model, and mass concentrations can be better corrected using a polynomial model. However, the BIC indicates that the models with particle properties and

environmental parameters are technically superior. When restricting the fit to the lower concentration, the model's accuracy decreases for both number and mass concentration, and the larger size bins tended to have higher errors. In addition, environmental conditions related to real-world scenarios need to be considered when applying these models. We used particles in a relatively narrow range of CRIs, morphologies, and densities, and our RH was restricted within 20% - 80%. If the particle properties and environmental conditions of interest are significantly different from the tested scenarios, one may need to consider these effects. Despite these limitations, this study has significant implications, especially for using these sensors in high concentration environments, including indoor air quality monitoring, occupational/industrial exposure assessments, wildfire smoke, or near-source monitoring scenarios. Since the test aerosols used in this study are applicable for several occupational health scenarios, a better exposure assessment could be achieved. In applying near-source and indoor air quality monitoring where field calibration might be challenging, these low-cost sensors, along with the calibration algorithms developed within a higher concentration range applied, could substitute for the traditional gravimetric instruments to provide accurate results air quality data.

2.2 Network of Low-cost Air Quality Sensor for Monitoring Indoor, Outdoor, and Personal $PM_{2.5}$ Exposure: Seattle 2020 Wildfire Case Study

Exposure to wildfire smoke has been linked to an increased risk of cancer and cardiorespiratory morbidity and mortality. Typical epidemiological studies are not based on individual exposure data. Recently, low-cost air quality sensor networks have been used to identify pollution sources and hotspots, given their ability to capture high spatiotemporal

resolution data. The increased frequency of wildfires in the Western United States has raised public awareness of the impact of wildfire smoke on air quality. Evidence-driven interventions can alleviate the impact of wildfire smoke on human health. This feasibility study demonstrates the use of a network of low-cost air quality sensors to gather indoor and outdoor $PM_{2.5}$ data to determine indoor/outdoor (I/O) PM concentration ratios and personal exposure levels. During September 2020, we deployed seven pairs of indoor and outdoor PM monitors in households and office spaces in the urban Seattle area, along with a personal exposure monitor worn by a subject. The data collected from this study showed that households equipped with high-efficiency particulate air (HEPA) filters and HVAC filtration systems had significantly lower I/O PM concentration ratios compared to those without air filtration; median I/O ratio of 0.43 vs. 0.82, $PM_{2.5}$ reduction of 58 % vs. 20%, respectively. The outdoor PM sensors showed a high correlation to the nearby Puget Sound Clean Air Agency monitoring stations (R^2 = 0.93). The personal monitor showed high variance in PM measurements as the subject moved through different microenvironments and could not be fully characterized by the relatively sparse network of indoor or outdoor sensors. A researcher with the knowledge of personal PM took adjusted filters placement in residence based on the low-cost sensor data, which led to a 61% $PM_{2.5}$ reduction compared to the home-based outdoor monitor. The findings suggest that more effective wildfire smoke interventions might be developed with wearable personal exposure monitors and the space-resolved PM concentration data available to people.

2.2.1 *Materials and Methods for Sensor Network Wildfire Smoke Study*

2.2.1.1 PM Monitor

The PM sensor Plantower PMS A003 (Beijing Plantower Co., Ltd, China; referred to as PMS hereafter) was incorporated in each monitor. PMS is an optical-scattering-based PM sensor.

A photodiode positioned normal to the excitation beam measures the light scattered by the particles in the optical volume. The scattering light intensity is then converted to a voltage signal to estimate PM number concentration and mass concentration using a proprietary calibration algorithm. The PMS provides estimated particle number concentrations in six size bins for particles with the optical diameter in 0.3-10 μm (#/0.1L) range and mass concentrations ($\mu g/m^3$) for PM_1, $PM_{2.5}$, and PM_{10}.

PMS reports the mass concentrations for two conditions: "standard" and "atmospheric", which changes the assumed particle density. The standard condition is designed to be used in specific environments, such as an industrial setting. The "atmospheric" condition has been tuned to measure particles commonly found in the ambient environment. In this study, $PM_{2.5}$ concentration for the atmospheric condition was measured at a 10-second interval. The same hardware was also used as a wearable monitor. One lab member from our research group wore the monitor on the left arm during daily activities throughout the wildfire event, including the occasional commute to the workplace from home. GPS data was used to coordinate the personal monitor data to a specific location and attribute the PM exposures to the participant's microenvironment.

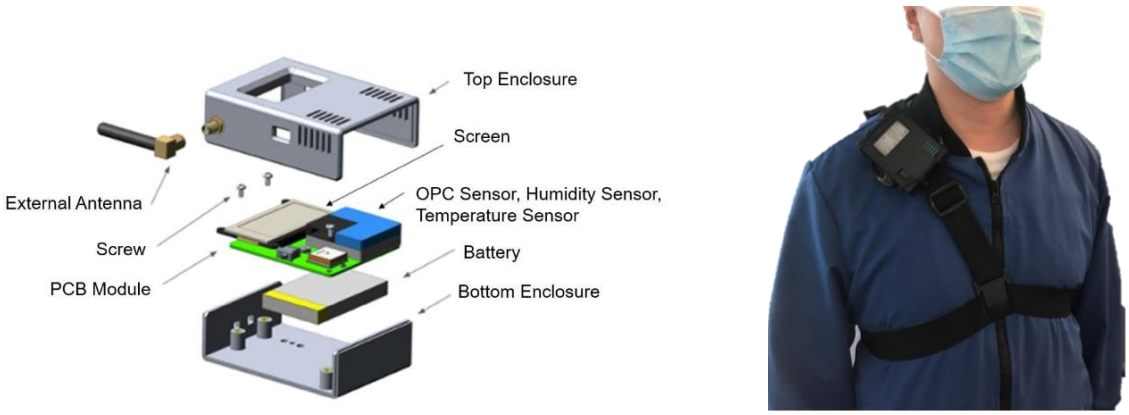

(a) **(b)**

Figure 2.11. a) Exploded view of the monitor, consisting of a PMS optical particle counter and other environmental sensors, PCB board, LiPo battery, and screen. The electronics are assembled in an ABS plastic enclosure. The device dimensions are (H) 100 mm × (W) 60 mm × (D) 25 mm and weigh 120 g; b) Personal monitor worn by a lab member.

2.2.1.2 Sampling Sites

To demonstrate the feasibility of using networked monitors to collect wildfire smoke-relevant PM measurements, we deployed monitors in different locations in Seattle, as described below. One lab member from our group also wore the monitor to measure the personal exposure to $PM_{2.5}$ during the wildfire event. The study was conducted between September 10 and September 30, 2020, covering the wildfire episode from September 10 to September 19 and the 11 days post the wildfire. The sampling sites included two University of Washington (UW) buildings and five residences in Seattle. Data from two nearby Puget Sound Clean Air Agency's (PSCAA) regional air monitoring stations was used for the data correction and comparison. Figure 2.12 shows the locations of the sampling sites in blue color and the two nearby regional air quality monitoring stations set up by PSCAA in green color. We collected information about the sampling sites such as housing type, size, HVAC, primary indoor PM sources, and locations of the sensors, see Table 2.6. Among the five residences, three (L1-L3) had either portable air purifiers or built-in non-HEPA air filtration in HVAC systems. Location 2 (L2) had two indoor

monitors in separate rooms. L4 and L5 did not have air filtration devices. Both UW buildings (L6 and L7) were largely unoccupied during the wildfire due to the shelter-in-place order and were not equipped with air filtration. The time-resolved indoor/outdoor PM concentration ratio (I/O ratio) was calculated to compare the effectiveness of each site's wildfire intervention strategy. No specific instruction was given to the participants.

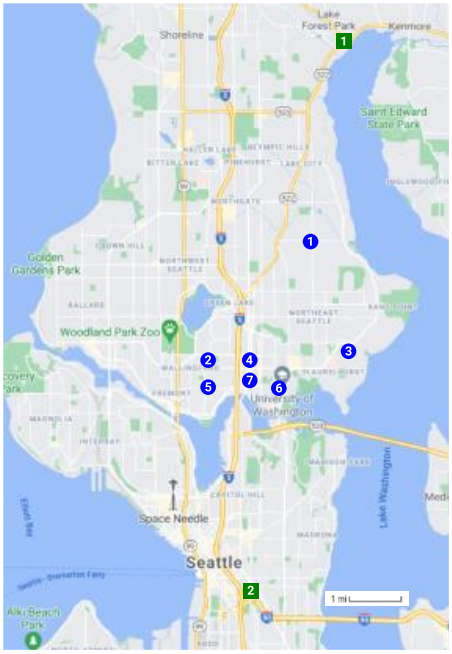

Figure 2.12. Locations of the sampling sites for this study in the urban Seattle area were marked in blue on the map; Two nearby public air quality monitoring stations from PSCCA were marked in green.

Table 2.6. General characteristics of the sampling sites.

Location ID	Housing Type	Size (sq.ft)	HVAC	HEPA	Window Opening	Indoor PM Sources [a]
L1	SFH	1000	Y	Y	Sometimes	Occasional cooking
L2-a L2-b	SFH	1200	Y	Y	No	Occasional cooking
L3	SFH	2000	Y	N[b]	No	Occasional cooking
L4	SFH	1300	Y	N	Always	Frequent cooking
L5	Apartment	500	N	N	Sometimes	Occasional cooking
L6	Office	135	Y	N	No	N/A
L7	Office	144	Y	N	No	N/A

[a] Self-reported information
[b] Electrostatic precipitator built in the HVAC
Definition of abbreviation: SFH = single-family home; Y = Yes; N= No; sq.ft = square feet

2.2.1.3 Analysis PM Data

We minimized the data discrepancy caused by the instrument difference by correcting the low-cost sensor data against the regional air quality monitoring stations. We corrected the data in this study against the PSCAA regional monitors using a subset of the data from the outdoor sensor outside a UW building (L6) during the wildfire event. We chose the data from this location for the correction because L6 had minimum local activities that may influence $PM_{2.5}$ measurement compared to the other sampling sites. The building was unoccupied during the wildfire due to the COVID lockdown (only essential personnel was allowed). It is located at least 200 meters from main streets with minimum local activities affecting local PM concentration. Our previous laboratory PMS sensor calibration study shows that the sensor to sensor accuracy is generally within 10% of each other when $PM_{2.5}$ metrics are used. [113] We aggregated the outdoor and indoor $PM_{2.5}$ data from the sensor network into hourly averaged data for the sensor correction and comparing it with the regional monitor data. We used 10-minute average data for personal exposure monitoring. Based on our previous calibration study on the PMS sensor, both linear model and quadratic model can be used to calibrate PMS sensors. In the study, a linear model and a quadratic polynomial model were fitted using the outdoor monitor data from L7:

$$\boldsymbol{Ref = \beta_0 + \beta_1 \cdot PMS} \tag{2.3}$$

$$\boldsymbol{Ref = \beta_0 + \beta_1 \cdot PMS + \beta_2 \cdot PMS^2} \tag{2.4}$$

where β_0 , β_1, and β_2 are the regression coefficients, Ref is the hourly reference $PM_{2.5}$ concentrations, and PMS and PMS^2 are the linear and quadratic coefficients, respectively. The fits with zero intercept ($\beta_0 = 0$) and non-zero intercept ($\beta_0 \neq 0$) were tested. The Bayesian Information Criterion (BIC) was used to select the correction model.

To compare the indoor and outdoor $PM_{2.5}$ concentrations during the wildfire period and post the wildfire event, the data was first divided into two subsets: the wildfire (September 10 00:00 – September 19 00:00, 2020) and the post-wildfire period (September 19 00:00, 2020 – September 30 00:00, 2020). We conducted the Wilcoxon signed-rank tests (for paired comparison) to compare the differences between the indoor and outdoor $PM_{2.5}$ concentrations during the wildfire period. In addition, the I/O ratios were calculated as the indicator of infiltration of wildfire smoke, the effectiveness of the interventions (for households with interventions), and indoor activities. The reduction rate of $PM_{2.5}$ during the wildfire period for each site and the personal exposure was calculated as

$$\boldsymbol{Reduction\ Rate} = \frac{\boldsymbol{O} - \boldsymbol{I}}{\boldsymbol{O}}\% \qquad (2.5)$$

where O is the outdoor $PM_{2.5}$ concentration during the wildfire event, and I is the indoor or personal $PM_{2.5}$ concentration during the wildfire event.

To evaluate the contribution of each microenvironment to total personal exposure, we attributed the personal daily $PM_{2.5}$ exposures to the microenvironments using GPS data. The raw $PM_{2.5}$ data from the wearable monitor was first aggregated into 10-min average data to reduce the data size without losing too much spatial resolution. The geocoordinates, recorded in conjunction with the $PM_{2.5}$ concentration', were grouped into three classifications: home, office, and other where the lab member spent most of the time during the wildfire event. We defined the

buffer zones encircled the home and the office building with a 10-meter clearance to minimize the classification error caused by the GPS drift. Records collected outside these two buffer zones were classified as "other locations". The $PM_{2.5}$ exposures attributed to each microenvironment of each day was calculated using the following equation:

$$\boldsymbol{AC_{k_j} = \frac{C_{k_j} \times F_{k_j}}{\sum_{k=1}^{n} F_{k_j}}} \quad \textbf{(2.6)}$$

where AC_{k_j} represents the attributable exposures of microenvironment k to the total personal exposure on day j; C_{k_j} is the hourly average $PM_{2.5}$ concentrations of microenvironment k on day j ; and F_{k_j} is the fraction of time spent in microenvironment k on day j.

2.2.2 *Results and Discussion for Sensor Network Wildfire Smoke Study*

2.2.2.1 Low-cost Sensor Correction

The data from the L6 outdoor sensor shows a good agreement with the regional monitors with the pre-calibration R^2 = 0.92. Similar to our previous calibration study for PMS with inorganic aerosol [113], the linear model shows the lower root-mean-square-error (RMSE) and BIC. The overall RMSE improves from 18.47 μg/m^3 to 14.35 μg/m^3 against the regional monitors. We did not observe a significant improvement from using a quadratic polynomial model. Thus, we chose the linear model for the $PM_{2.5}$ correction. The data from all the other sensors for the following analysis was corrected with this linear model. Note that while the $PM_{2.5}$ correction agrees with reference monitors using the linear model, the particle number density data from the sensor were not evaluated for wildfire smoke. The particle size-dependent data from low-cost optical sensors are significantly influenced by the particle index of refraction,

particle morphology, particle loading, sensor geometry, and environmental conditions [113, 119-123].

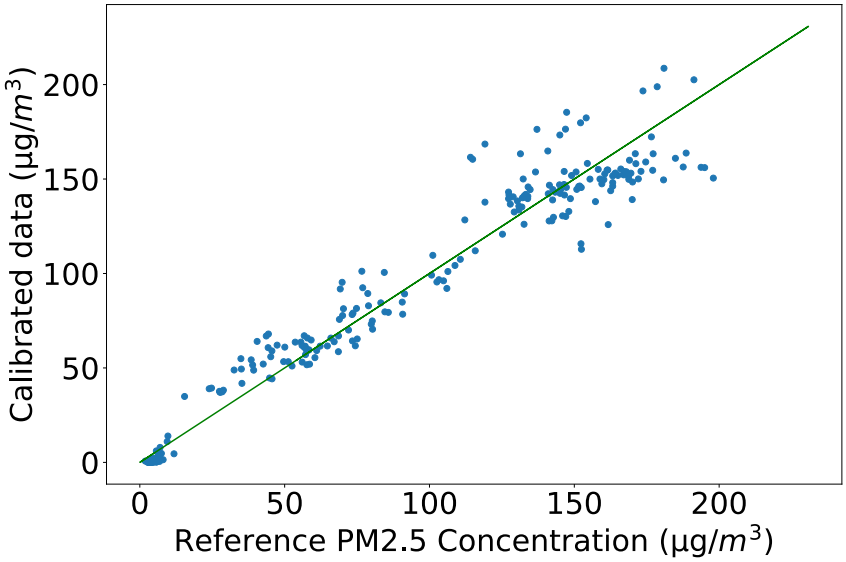

Figure 2.13. Scatter plot of the calibrated and reference $PM_{2.5}$ data. The green line represents the 1:1 relationship between the low-cost sensor and reference monitor concentration with the post-calibration R^2 = 0.94.

2.2.2.2 Time-resolved PM Concentrations

To observe differences between indoor, outdoor and regional monitor $PM_{2.5}$ concentrations, Figure 2.15 shows 1-hour averages of $PM_{2.5}$ concentrations measured by the calibrated PMS sensor network and the regional monitors during the wildfire. The data collected during the wildfire is divided into indoor and outdoor categories. The indoor data is further divided into HEPA (L1-L3) and Non-HEPA (L4-L7) subcategories to show the influence of interventions on $PM_{2.5}$ concentrations. The shaded areas represent one standard deviation (1σ) of the measurements. The data from the outdoor monitors closely match the reference monitors. The correlation between the outdoor PM concentration from the sensor network and the one form reference monitors is 0.92 when corrected by the calibration model. In some cases, the sensor network reported higher PM concentration likely due to the local activities near some sampling

sites, which the reference monitors could not detect. The discrepancy may also be caused by the instrument principle of operation (optical particle counter vs. nephelometer) or averaging in procedures. The sensor network sampling frequency was set to 10 seconds, while the reference monitors' reporting frequency was 1 hour. Though the 1-hour averages were compared, see Figure 2.15 the temporal spikes in the sensor network data may have contributed to these differences.

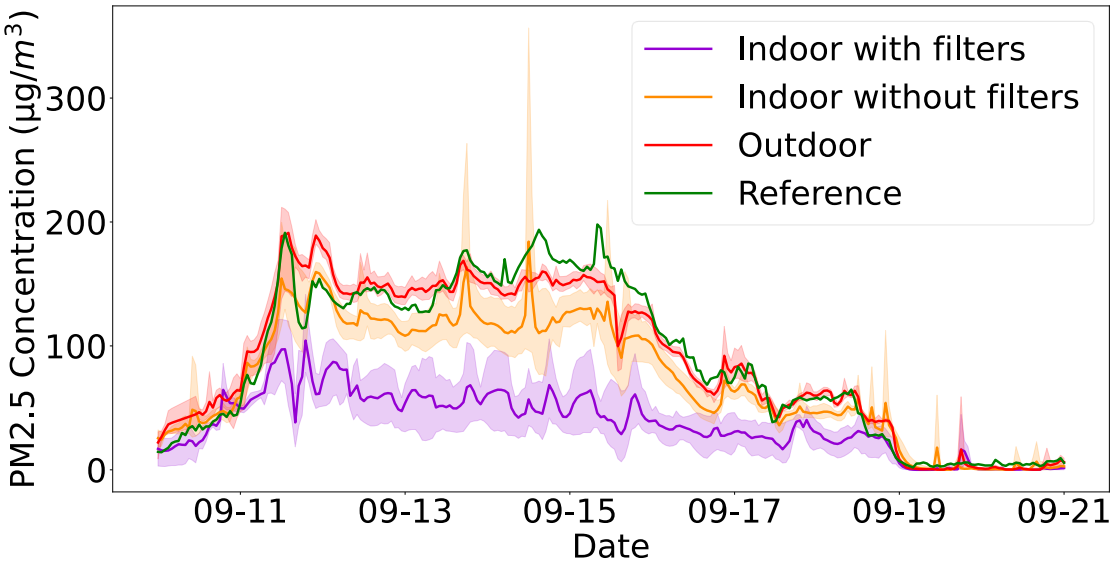

Figure 2.14. Time-series plots of averaged indoor and outdoor $PM_{2.5}$ concentrations across different sampling sites compared to the reference monitors during the wildfire event. The purple and orange lines illustrate the sensors' averaged indoor $PM_{2.5}$ concentrations measurements at sampling sites with and without HEPA filtration, respectively. The shading around each line shows the differences between the sensor measurements within each category.

The indoor monitors from the locations with active PM filtration showed a significantly lower indoor PM concentration. Indoor PM levels for the sites without filters were slightly lower than the outdoor values. Occasional spikes in PM concentration, above the already high baseline, were observed due to cooking activities. Note that even with the active PM control strategies implemented in several households, the average $PM_{2.5}$ is still above the typical (non-wildfire)

Seattle outdoor $PM_{2.5}$ concentration (<10 $\mu g/m^3$) or the EPA's recommendation for maximum particle exposure limit (35 $\mu g/m^3$) [124, 125].

2.2.2.3 Detailed PM Concentrations

A case-by-case analysis is presented below to provide insight into the effectiveness of aerosol mitigation strategies and the significance of sensor numbers and placement within the residence. Figure 2.15 shows the 1-hour average indoor and outdoor PM data for all sites during the wildfire with the average $PM_{2.5}$ from the two public monitors in green color for comparison. The post-wildfire $PM_{2.5}$ measurements show that many outdoor $PM_{2.5}$ concentration spikes were caused by local activities, which the regional monitors did not capture. The time-resolved $PM_{2.5}$ concentration for the post-wildfire period can be found in Figure 6.1 and Figure 6.2.

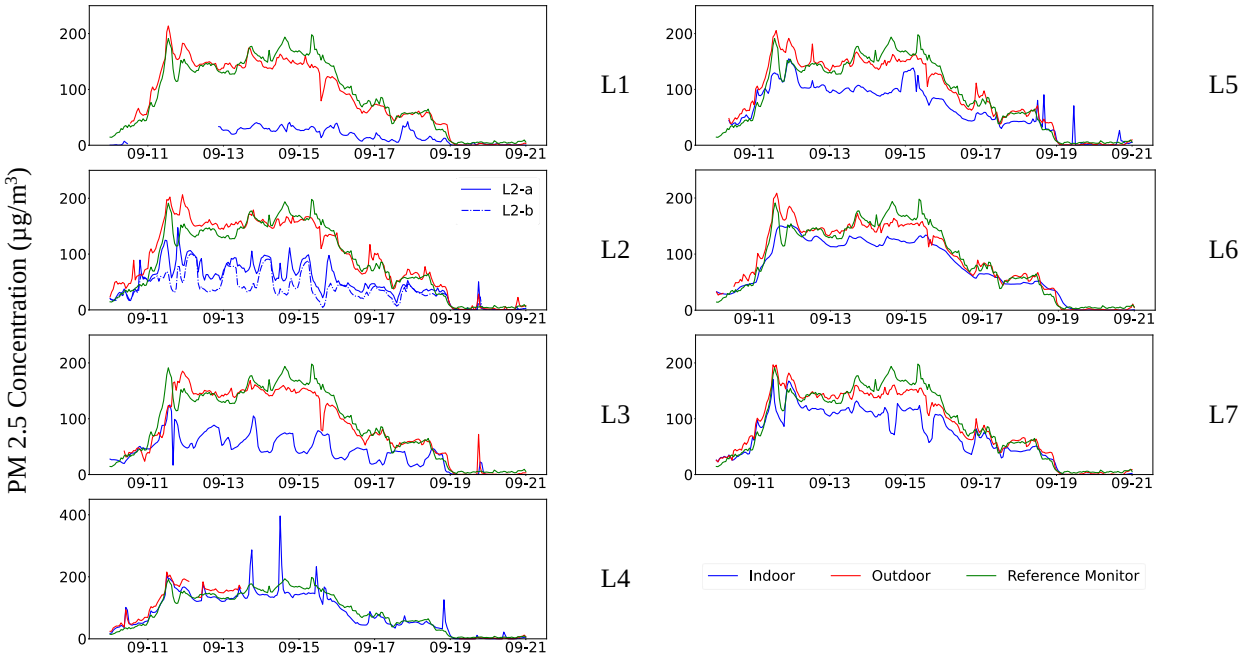

Figure 2.15. Time-series plots of indoor and outdoor $PM_{2.5}$ concentrations compared to the reference monitors for each sampling site during the wildfire. The blue and red lines illustrate the sensors' indoor and outdoor $PM_{2.5}$ concentrations measurements, and the green line illustrates the averaged $PM_{2.5}$ measurements from the nearby regional monitoring sites.

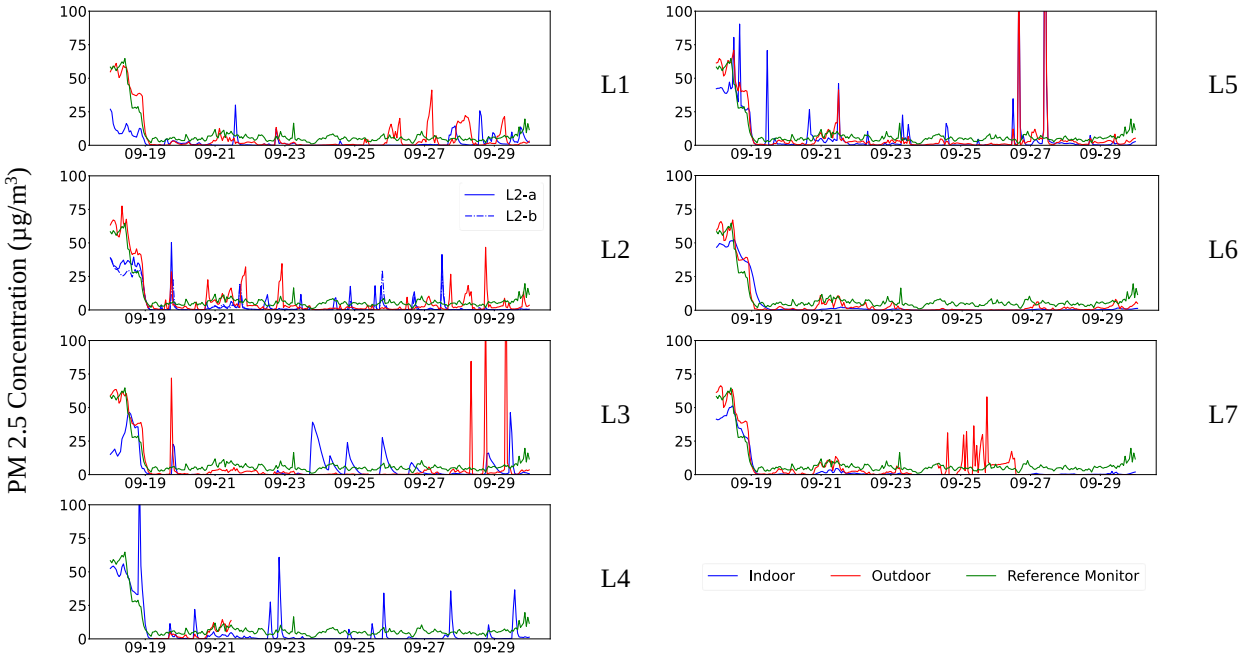

Figure 2.16. Time-series plots of indoor and outdoor $PM_{2.5}$ concentrations compared to the reference monitors for each sampling site post the wildfire. The blue and red lines illustrate the sensors' indoor and outdoor measurements, and the green line illustrates the averaged $PM_{2.5}$ measurements from the nearby regional monitoring sites.

Location L1 had the indoor monitor placed in a relatively small room (home-office ~150 ft^2) with a high-volume HEPA filter for the entire wildfire episode. This strategy resulted in the lowest local I/O ratio (0.1-0.2); however, data for other locations (e.g., bedrooms, living room) within the residence are not available, which is problematic for assessing overall personal exposure to PM. For I/O analysis, reference Figure 2.18.

The residents from L2 had the two monitors in separate rooms: L2a was placed in a large living room (~350 ft^2) and L2b - in the home office (120 ft^2). Two stand-alone HEPA filtration units were used: one in the living room, the other was moved from the office to the bedroom at nighttime. The data from the living room has relatively low variance; however, the larger room was not effectively cleaned by the undersized filtration unit, I/O stayed relatively constant ~0.5. When the filtration unit was positioned in the office, the I/O ratios drop significantly ~0.2;

however, when the filter was moved from the home office to the bedroom, the PM increased to the level of the adjacent living room. The fixed sensor did not monitor the bedroom; however, the wearable sensor has recorded significant PM reduction in the bedroom during the night periods (I/O~0.1), see Figure 2.18 and

Table 2.8. Summary of the indoor and outdoor $PM_{2.5}$ levels (µg/m3) during wildfire and post-wildfire period for each sampling site.

Location ID	Indoor (Wildfire)		Outdoor (Wildfire)		Indoor (Post-Wildfire)		Outdoor (Post-Wildfire)		Wildfire $PM_{2.5}$ Reduction [a] (%)
	Mean	Max	Mean	Max	Mean	Max	Mean	Max	
L1	23.09	46.63	120.9	236.55	1.22	4.94	1.36	10.48	77.22
L2-a	64.96	163.1	128.78	228.28	2.31	55.7	4.04	31.44	46.67
L2-b	46.85	110.79	128.78	228.28	1.7	25.84	4.04	31.44	59.48
L3	54.08	137.91	116.33	204.99	1.3	25.08	3.15	79.68	49.57
L4	115.44	438.35	143.52	238.63	2.2	24.34	2.24	13.43	13.3
L5	88.16	171.4	125.26	227.35	4.28	78.25	2.17	10.59	28.83
L6	100.52	166.93	121.82	230.82	2.98	31.78	1.59	12.19	15.7
L7	91.23	188.81	119.08	217.62	0.85	14.15	2.12	10.24	21.42

[a] Calculated using the indoor and outdoor $PM_{2.5}$ levels during the wildfire event.

.

The L3 had an electrostatic precipitator installed in the HVAC system. The HVAC system was controlled by a thermostat, which explains the periodic pattern of the PM concentration. The PM concentration (measured in the bedroom) dipped when the forced-air HVAC system was activated during the daytime. During the nighttime, the indoor PM levels went up. Note that if filtration units were placed in the bedroom, the overall exposure could be reduced significantly; however, the L3 residence relied on the central HVAC system to control temperature and the PM levels.

L4 site kept their kitchen windows open during the wildfires, which explains the highest background indoor PM level among all the sampling sites. L4 indoor monitor was placed in the kitchen where it detected the spikes from cooking activities in addition to the high background level from wildfire smoke intrusion. L4 outdoor sensor stopped working three days after the deployment because it was accidentally unplugged. I/O ratio for L4 was calculated using the data

collected before September 13 for the wildfire period and the data collected between September 19 and September 22 for the post-wildfire period.

L5 had the monitor placed in the apartment's kitchen/living room area (200ft^2), which had a low-grade filter in the HVAC system. PM concentration was lower than the outdoor level most of the time wildfire but higher than other residences with high-efficiency filtration units. L6 and L7 are two UW buildings with HVAC systems but low-grade filtration units. The data is similar to the L5 residential site. The buildings were largely unoccupied during the wildfire due to the COVID lockdown, and the windows were closed. The indoor $PM_{2.5}$ at L6 and L7 are lower than outdoor. The I/O ratios were very similar to L5 (~0.7-0.8).

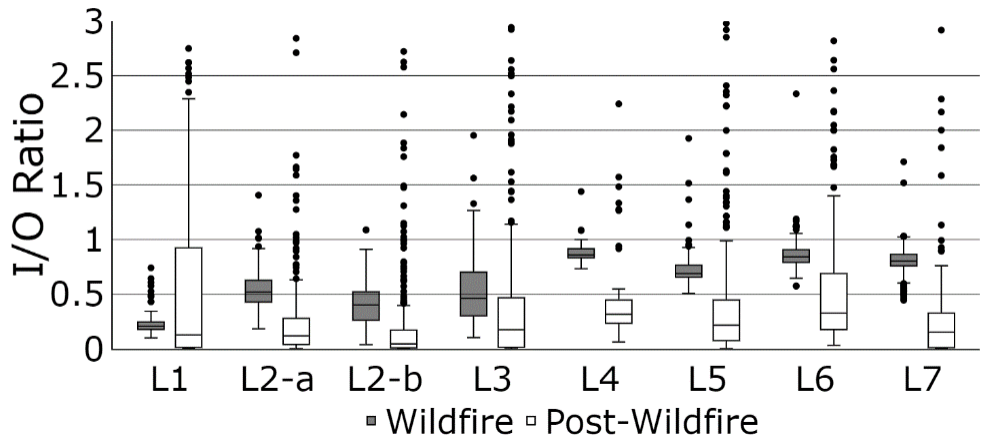

Figure 2.17. Boxplot of hourly $PM_{2.5}$ I/O ratios for each sampling site. The white and black boxes show the data from wildfire and post-wildfire periods, respectively.

Figure 2.17 compares the hourly $PM_{2.5}$ indoor/outdoor (I/O) ratios of different monitoring sites during and after the wildfire. During the wildfire episode, the average I/O ratio across all seven sites was 0.62. The mean and median I/O ratios were all < 1 during the wildfire and post-wildfire periods. Compared with the post-wildfire period, the I/O ratio during wildfire was higher by 36% on average ($p < 0.05$). Sites with air filtration (L1, L2-a, L2-b, and L3) and sites without air filtration (L4- L7) had an average I/O ratio of 0.43 and 0.82, respectively. Overall,

sites with air filtration had I/O ratios lower by 47% and 14% on average than those without it during and after a wildfire, respectively. See

Table 2.7. The maximum I/O ratios during the post-wildfire period were generally higher than those during the wildfire episodes due to the lower outdoor $PM_{2.5}$ concentrations and the change in residence behavior, e.g., (i) the filters were turned off (ii) door and window we open more often.

Table 2.7. Summary of the $PM_{2.5}$ I/O ratios during and post the wildfire for each sampling site.

ID	I/O ratios (Wildfire)				I/O ratios (Post-wildfire)			
	Min	**Median (IQR)**	**Mean (SD)**	**Max**	**Min**	**Median (IQR)**	**Mean (SD)**	**Max**
L1	0.1	0.21	0.23	0.74	N/A	0.13	0.54	193.38
L2-a	0.18	0.52	0.54	1.41	N/A	0.12	0.24	287.68
L2-b	0.04	0.40	0.41	1.09	N/A	0.05	0.22	49.08
L3	0.10	0.46	0.54	5.23	N/A	0.17	0.43	2599.18
L4	0.73	0.86	0.88	1.44	0.06	0.32	0.46	7.17
L5	0.51	0.69	0.73	1.93	N/A	0.22	0.40	880.27
L6	0.57	0.84	0.86	3.62	0.03	0.33	0.54	23.75
L7	0.44	0.80	0.80	1.71	N/A	0.15	0.27	2.92
Definition of abbreviations: IQR = interquartile range, SD = standard deviation								

Table 2.8 lists the mean and maximum $PM_{2.5}$ for each sampling site during and after the wildfires. $PM_{2.5}$ reduction was calculated for each site based on the difference between the average indoor and outdoor $PM_{2.5}$. The maximum $PM_{2.5}$ reduction observed in the study is 77% for L1, where the relatively small "clean room" environment was created and monitored. The L2b, also located in the small room, had a near 60% reduction in PM concentration; however, the air filter was removed to a different location was the room was not occupied. The L2a location had the filter on for the entire time, but the filtration rate did not match the room air volume. The PM reduction was ~50%, similar to the central air filtration HVAC system at L3. The sampling site L4 without any air filtration system and the windows open had only a 13% reduction. Only a moderate reduction in PM levels (16-29%) was observed when low-grade PM filers were used at L5, L6, and L7 sites.

Table 2.8. Summary of the indoor and outdoor $PM_{2.5}$ levels (µg/m3) during wildfire and post-wildfire period for each sampling site.

Location ID	Indoor (Wildfire)		Outdoor (Wildfire)		Indoor (Post-Wildfire)		Outdoor (Post-Wildfire)		Wildfire $PM_{2.5}$ Reduction [a] (%)
	Mean	Max	Mean	Max	Mean	Max	Mean	Max	
L1	23.09	46.63	120.9	236.55	1.22	4.94	1.36	10.48	77.22
L2-a	64.96	163.1	128.78	228.28	2.31	55.7	4.04	31.44	46.67
L2-b	46.85	110.79	128.78	228.28	1.7	25.84	4.04	31.44	59.48
L3	54.08	137.91	116.33	204.99	1.3	25.08	3.15	79.68	49.57
L4	115.44	438.35	143.52	238.63	2.2	24.34	2.24	13.43	13.3
L5	88.16	171.4	125.26	227.35	4.28	78.25	2.17	10.59	28.83
L6	100.52	166.93	121.82	230.82	2.98	31.78	1.59	12.19	15.7
L7	91.23	188.81	119.08	217.62	0.85	14.15	2.12	10.24	21.42

[a] Calculated using the indoor and outdoor $PM_{2.5}$ levels during the wildfire event.

2.2.2.4 Personal Exposure Measurement – A Case Study

We compared the personal data measured by the wearable and the home-based monitors' data to understand how personal exposure varied in different microenvironments. Figure 2.18 shows the 10-minute average of $PM_{2.5}$ concentration measured by the wearable and home-based sensors of the personal sensor's wearer. Wearable sensor $PM_{2.5}$ data show 10% lower exposure

than the home-base monitors' estimation and 61% lower than the reference monitors' estimation. The shaded areas mark the nighttime (10:00 pm - 6:00 am). The researcher's wearable monitor recorded significantly lower $PM_{2.5}$ concentration at night than the other two home-based monitors located in the living room and the home office, which can be explained by the colocation of the air purifier and the wearable monitor. The lab member is an aerosol science researcher who constantly adjusted his interventions based on his personal PM data. The difference in the personal exposures, measured by the wearable and the home-based monitor, indicates that access to personal real-time PM concentration data can enhance the efficacy of PM exposure interventions.

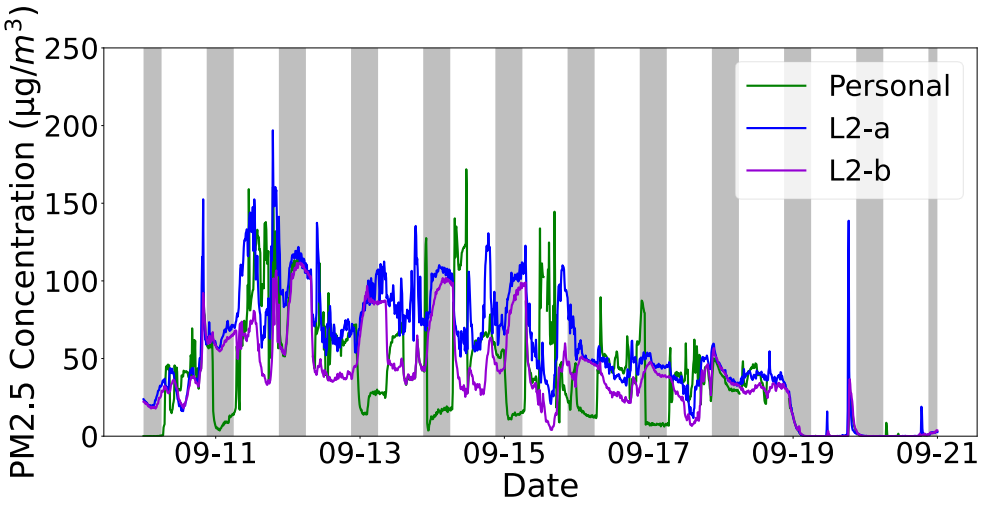

Figure 2.18. Profile of 10-minute averaged $PM_{2.5}$ concentrations by the personal monitor (green line) and the monitors in the two bedrooms (the blue and purple line) during the wildfire.

We also apportioned the lab member's exposure based on the location. Figure 2.19a shows the 10-minute average of $PM_{2.5}$ concentration measured by the subject's sensor color-coded based on the microenvironment. The lab member spent most of his time at home and less than 10% time in the workplace. Exposure outside the home and the workplace was categorized into other locations. The wearable monitor recorded higher $PM_{2.5}$ levels in the subject's

workplace and other locations than at the residence. The workplace did not have an air filtration system. Figure 2.19b shows the weighted daily average personal exposure in different microenvironments. The personal exposure contribution from the workplace and other environments was ~50%, while the time spent in these environments was ~ 30%. The attribution of personal exposure to microenvironments can help plan personal activities during wildfire seasons.

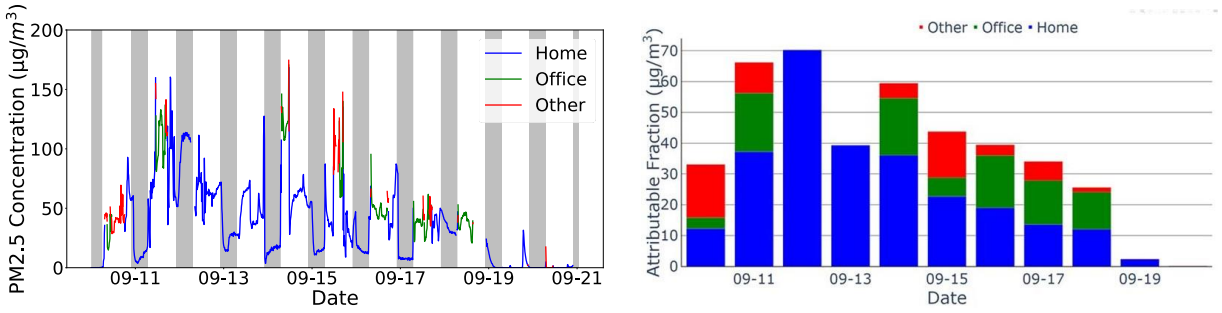

a **b**

Figure 2.19. a) Time-resolved $PM_{2.5}$ concentration measured by the personal monitor color-coded based on the microenvironment the participant was in; b) Weighted daily average personal exposure in different microenvironments

2.2.3 *Conclusions on Sensor Network Wildfire Smoke Study*

This study demonstrated the application of a low-cost sensor network for air quality monitoring during the wildfire. When used with corrections, the sensor data was comparable to the nearest regional monitor. The significance of this finding is that the calibration model allows for obtaining real-world data using low-cost sensors and developing a high-density sensor network for monitoring outdoor PM levels and indoor environments at a low cost. Our results showed that during the wildfire event, the outdoor $PM_{2.5}$ level was > 200 µg/m^3 in the Seattle area; Spatial variance for $PM_{2.5}$ in the urban area was low during the wildfire episode. Using portable air purifiers was associated with lower indoor $PM_{2.5}$ levels during the wildfire episode,

with a 50 - 77 % reduction among the sampling sites. However, the observed levels were still higher than the typical outdoor $PM_{2.5}$ level (< 10 $\mu g/m^3$) in the region. The analysis shows I/O ratio was driven by the outdoor concentration and occupants' activities, such as filtration units, keeping doors and windows closed or open, and PM generation activities, such as cooking. The personal monitoring results highlighted the influence of personal activities and microenvironments on an individual's exposure to $PM_{2.5}$. The hyperlocal activities significantly influenced personal exposure in the microenvironments. The exposure level measured by wearable monitors was lower than the exposure estimated by the home-based monitors due to the proactive behavior of the volunteer based on the available real-time personal PM data. Although this study is based on relatively small sample size, it demonstrated that personal action, such as staying indoors and using HEPA air cleaner, can potentially reduce personal exposure to wildfire smoke. Future studies with larger sample size and a collection of time-activity information are warranted to investigate the source of $PM_{2.5}$ exposure and estimate the consequent health effects.

Chapter 3. AEROSOL SAMPLING FOR IN-SITU CHEMICAL ANALYSIS

Aerosol sampling and identification are vital for assessing and controlling particulate matter pollution, airborne pathogens, allergens, and toxins and their effect on air quality, human health, and climate change. To date, a variety of devices using passive [126] and active[127] methods (i.e., filters, cyclones, and impactors) have been developed [128]. These methods are robust in capturing airborne particles but are not designed for in-situ chemical analysis preventing their usage in epidemiological studies and personal exposure assessment. This chapter presents the development and evaluation of the micro-well aerosol collection cartridge compatible with in-situ chemical analysis and other standard lab analyses. The work on the design of the microwell collection cartridge is published in Aerosol Science and technology [115]. The evaluation of the cartridge for the collection of biological aerosol is published in PlosOne [129].

3.1 FINE PM COLLECTION - DESIGN AND EVALUATION OF AN AERODYNAMIC FOCUSING MICRO-WELL AEROSOL COLLECTOR

In-situ analysis of aerosols' chemical and biological components on a conventional filter is challenging due to dilute samples in a large collection region. We present the design and evaluation of a micro-well (μ-well) aerosol collector to assess airborne particulate matter (PM) in the 0.5-to-3-micron size range. The design minimizes particle collection areas allowing for in-situ optical analysis. It provides an increased detection limit for liquid-based assays due to the high concentrations of analytes in the elution/analysis volume. The design of the collector is guided by computational fluid dynamics (CFD) modeling; it combines an aerodynamic

concentrator inlet that focuses the aspirated aerosol into a narrow beam and a µ-well collector that limits the particle collection area to the µ-well volume. Optimizing the collector geometry and the operational conditions results in high concentrations of collected PM in the submillimeter region inside the µ-well. Collection efficiency experiments are performed in the aerosol chamber using fluorescent polystyrene microspheres to determine the collector's performance as a function of particle size and sampling flow rate. The collector has the maximum collection efficiency of about 75% for 1-micron particles for the flow rate of 1 slpm. Particles bigger than 1 micron have lower collection efficiencies because of particle bounce and particle loss in the aerodynamic focusing inlet. Collected samples can be eluted from the device using standard pipettes, with an elution volume of 10-20 microliters. The transparent collection substrate and the distinct collection region, independent of particle size, allows for in-situ optical analysis of the collected PM.

3.1.1 *Materials and Methods*

3.1.1.1 Impactor Geometry Consideration

While CFD modeling can provide detailed simulations of complex flow structures and can be used to refine the geometry through an iterative process, it is possible to use one-dimensional analytical modeling as a first step to identify suitable geometry parameters. Analytical and numerical modeling is used to optimize the following geometry parameters: (i) dimensions of the aerodynamic inlet, (ii) dimensions of the µ-well, and (iii) distance between the nozzle and the impaction plate.

The design of the AF inlet is based on the optimal Stokes number calculations for focusing particles in the 1-5 µm size range. The base operating flow rate of the collector is 0.75-

2 slpm at standard conditions (293 K, 101 kPa). In the preliminary calculations for the AF inlet geometry, the optimum Stk*=1 required for focusing 2-micron particles is used:

$$\boldsymbol{Stk^{*} = \frac{\tau}{D_c/U} = \frac{C_c \rho_p d_p^2 U}{18 \eta D_c} \cong 1} \qquad \textbf{(3.1)}$$

where: C_c is the Cunningham slip correction factor, ρ_p is the particle density, d_p is the particle diameter, U is the area-averaged axial velocity magnitude at a well's upstream location, η is the gas viscosity, and D_c is the characteristic dimension which, in this case, is the diameter of the nozzle. As a first step in selecting AF inlet geometry, the diameter of the nozzle is calculated based on the designed flow rate of 1 slpm. The diameter is set to be 0.8 mm to maintain the laminar flow regime. This diameter selection also satisfies the practical considerations of compatibility with standard pipette tips for sample elution. As the second step, the first stage inlet diameter is calculated based on the Stokes number calculation for focusing on the particles with aerodynamic diameters of 1-5 microns. For non-compressible flow, the velocity magnitude in Eq. **(3.1)** can be written as:

$$\boldsymbol{U = \frac{4Q}{\pi D^2}} \qquad \textbf{(3.2)}$$

where Q is the volumetric flow rate, then the optimal inlet diameter can be calculated as of the inlet for a given particle size as:

$$\boldsymbol{D^{*} = \sqrt{\frac{4 C_c \rho_p d_p^2 Q}{18 \eta D_c \pi Stk^{*}}}} \qquad \textbf{(3.3)}$$

An analytical model, based on Eq. 3, shows that a single value of D^* cannot cover the entire range of operating conditions and particle sizes. In the numerical model, the D/W ratio of 1.5 and 2 are considered for the aerodynamic inlet. D/W = 2 is used in the final design, as this

ratio has a better overall focusing effect for particles in the 1-5 µm diameter range at a lower flow rate (1 slpm), which is similar to Deng et al. [79].

Effects of the micro-well wall angle and the distance between the nozzle and the impaction plate are not examined analytically due to the complexity of the parameter field; instead, these effects are examined using CFD simulations. The well angles 30, 45, and 60-degree and the nozzle-to-plate distances (S = 0.75 mm and 0.5 mm) are studied using CFD simulations. As expected, similar to Grinshpun (2005), the low ratio of S/W shows a low size cutoff. Although the range of values is tested, we only present data for the nozzle to plate distance of 0.5 mm. Note that for the µ-well designs, the nozzle to plate distance is not the same as the particle travel length related to the particle stopping distance, as the particle needs to penetrate the recirculation zone inside the µ-well sufficiently.

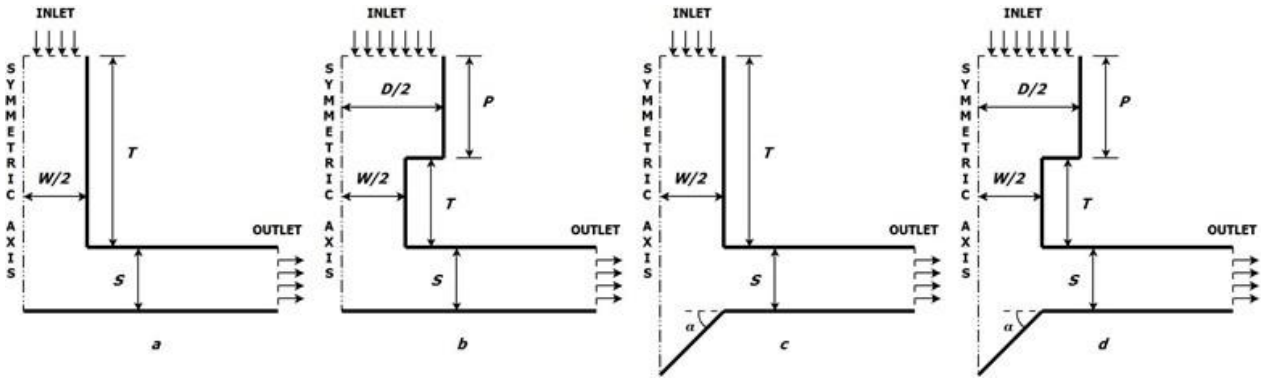

Figure 3.1. Schematics of the computational domain for four inertial impactors: (a) base geometry: no focusing, flat collection plate; (b) flat plate collector with AF inlet; (c) µ-well collector without AF inlet; (d) µ-well collector with AF inlet. (Note: schematics are not to scale).

The numerical and experimental results for each geometry are compared to the base case - a flat plate impactor without AF inlet and with a ratio of nozzle diameter to impaction distance of two (W/S=2). Figure 3.1 shows the geometries considered in the study: Figure 3.1a - the base-collector, Figure 3.1b - AF inlet with a flat plate impactor, Figure 3.1c - the µ-well impactor without AF inlet, and Figure 3.1d - µ-well with the AF inlet. The diameter of the nozzle is

denoted as W, the length of the nozzle as T, the diameter of the first stage of AF inlet as D, the length of the first stage as P, the impaction (nozzle-to-plate) distance as S, and α is the angle of the well cone. Detailed dimensions used in the simulations are listed in Table 3.1.

Table 3.1. Dimensions of geometries used in the simulations (unit: mm).

Parameter	Case			
	a	***b***	***c***	***d***
D	N/A	1.6	N/A	1.6
W	0.8	0.8	0.8	0.8
P	N/A	3.25	N/A	3.25
T	6.5	3.1	6.5	3.1
S	0.5	0.5	0.5	0.5
α	N/A	N/A	30°, 45°, 60°	45°

3.1.1.2 Numerical Modeling of the Micro-well PM Collector

The analytical calculations used in the preliminary design help select the operating parameters and estimate collector performance; however, they do not provide information about the flow field inside the collector and cannot be used to calculate particle collection efficiency. CFD simulations provide insight into the particle trajectories in the complex flow field; the simulations are performed using a commercial software package (Fluent™ 15.0). The steady-state, laminar, double precision solver is used to obtain the flow field. As described earlier, the range of flow rates is limited to the laminar flow regime (Re < 2300) in all cases. A second-order upwind convergence scheme is used to avoid the numerical viscosity associated with first-order convergence schemes in the CFD simulations. The primary use for the calculations is to examine the behavior of the flow and the particle trajectories near the impaction region. A coupled pressure-velocity solver scheme is used in all simulations. The boundary conditions are set as uniform inlet velocity profiles as calculated to match the target flow rate and pressure outlet with zero-gauge pressure. The walls are modeled as a no-slip boundary. Dry air properties at 293 K

and 101 kPa are used in the simulations. Although the design of the collector is based on the flow rates in the range 0.75-2 slpm, only the results for 1 slpm are presented here.

The flow field is calculated using a 2D structured mesh; the mesh is refined near the AF inlet, near the impaction plate, and in the μ-well region to obtain mesh independence in the CFD solution. The resulting model contains about 30,000 quadrilateral cells; further refinement in the mesh density did not affect the flow behavior, boundary layer profiles, or particle collection efficiency. Simulations are run until all residuals reach their plateau at levels of at least ten orders of magnitude below the initialization level.

Particle trajectories are calculated using the Discrete Phase Models (DPM) after the flow field is obtained. Stoke-Cunningham drag law is used in particle trajectory calculation. In this Lagrangian approach, the particles are treated as a discrete phase dispersed in the continuous fluid flow. This particle tracking technique was chosen due to its ability to handle the relevant forces acting on the particles and accurately model particle behavior near the wall. Due to the dilute nature of atmospheric aerosols, the particles do not appreciably affect the fluid flow, so two-way coupling is not considered. The DPM model uses 100 liquid water particles (particle density ρp=998.2 kg/m^3). To model uniform particle concertation at the collector inlet in the axisymmetric simulation, the geometry inlet is divided into five equally spaced sections, representing concentric rings in 3 dimensions. The number of particles introduced in each section is proportional to the area of the ring (injection plane). The particles of the prescribed diameter are released with zero velocity, which allows for the tracking of individual particles, the correlation of their trajectories with the initial injection point, and assessing the effectiveness of the aerodynamic focusing. In this work, only aerodynamic drag is considered in the analysis of particle motion. Other mechanisms, such as gravitational settling, electrostatic forces, Brownian

diffusion, and thermophoretic and Safman forces, are neglected due to their insignificance compared to the aerodynamic drag. Particles are assumed to be trapped upon contact with the μ-well or the 1 mm diameter collection area for the flat plate case. In the AF inlet cases, particles that contact the forward-facing step of the AF inlet are considered to be lost. The wall condition elsewhere is set to the "bounce" boundary condition. The number of particles trapped in the well or the collection area is recorded for each particle size. The collection efficiency (ε) is determined by the fraction of particle trajectories intercepted by the impaction plate or the μ-well.

3.1.1.3 Micro-well Collection Efficiency Testing

The experimental study to assess the collection efficiencies of the design is performed for several geometries and the range of operating conditions. The inlet and outlet manifold of the collector prototypes are fabricated using 3D printing techniques, and the μ-well is fabricated by the precision drilling of a microscope slide (see Figure 3.2a). Figure 3.2b shows the critical dimensions of the optimized collector used in the experiments. To precisely control the final dimensions and the surface roughness of the collector nozzle, an additional finishing step is required; the dimensions of the nozzles are checked using optical microscopy for proper tolerances. The μ-well is fabricated in a standard 75 mm × 25 mm × 1 mm microscope slide using diamond cutting tools with the specified cutting angle. The wells are examined for reproducibility to confirm the dimensions. While several different geometries are tested in the preliminary study, the final choice for the μ-well is a cone shape with a diameter of 1 mm and a depth of 0.5 mm (45-degree angle), as shown in Figure 1. A 0.5 mm thick silicone gasket provides the proper nozzle to plate distance, the seal between the nozzle, and the impaction plate. All collectors are checked for vacuum seal before conducting the experiments.

The assembled collectors are tested in the aerosol chamber, as shown in Figure 3.3. All reported experiments are performed at 1 slpm sampling flow rate with fluorescent monodisperse polystyrene latex (PSL) particles (Fluoresbrite® YG Microspheres, Polysciences, Inc., Warrington, PA); particle sizes are 0.5, 0.75, 1, 2, and 3 µm (density 1.05 g/cm^3). There are three reference filters (Spectrum Poretics® polycarbonate membrane filters, 47mm, 0.1, 0.6 um pore sizes) in open face aerosol filter holders (EDM Millipore, Billerica, MA, model XX5004710) collect particles in each experiment.

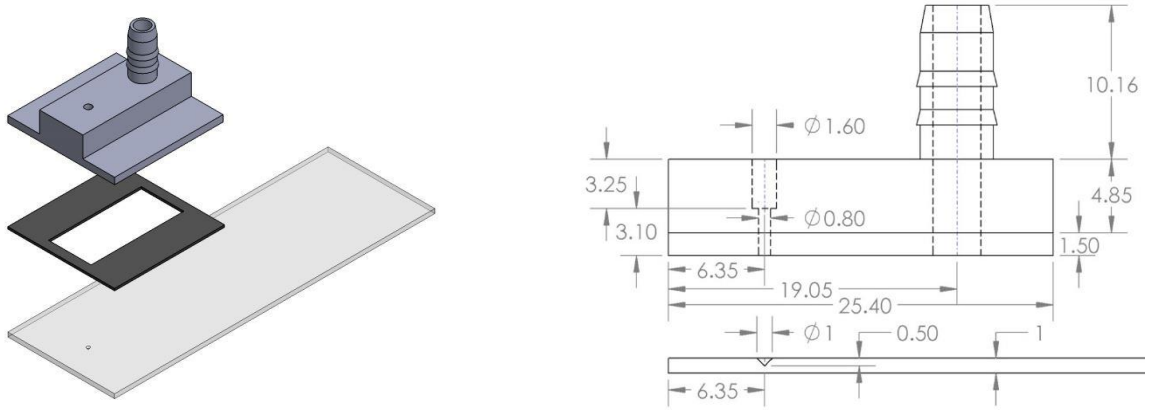

a **b**

Figure 3.2. (a) 3D assembly of the µ-well collector used in the experiment and (b) drawing of the collector with AF inlet used in the study (unit: mm).

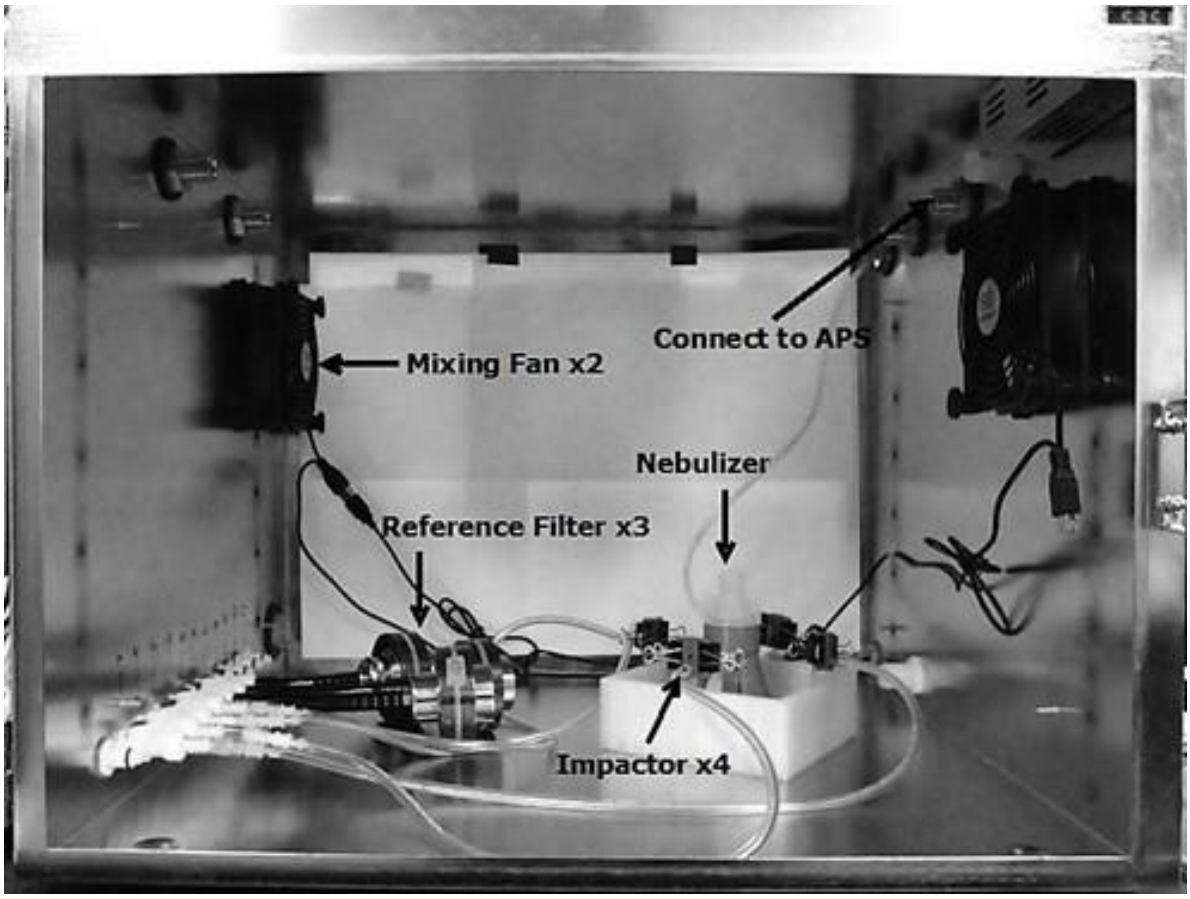

Figure 3.3. Photograph of the assembled impactors and reference filters in the aerosol chamber.

A stock particle solution (typically 2-3% solid fraction) is diluted 100x in distilled water. During the experiment, about 5 ml of the prepared solution is nebulized from the liquid suspension using the MADA Up-Mist™ Medication nebulizer (MADA Products, Carlstadt, NJ) inside the chamber. The aerodynamic particle sizer (APS 3321, TSI, Shoreview, MN) is used to verify the particle size and monitor the particle concentration in the chamber. APS measurements confirm that there is no significant aerosol agglomeration during the experiment. The typical particle concentration for particles smaller than 2 μm is between 5000 and 7000 particles/cm3.

Two mixing fans inside the chamber maintain uniform particle distribution; the humidity inside the chamber is set to be 50%.

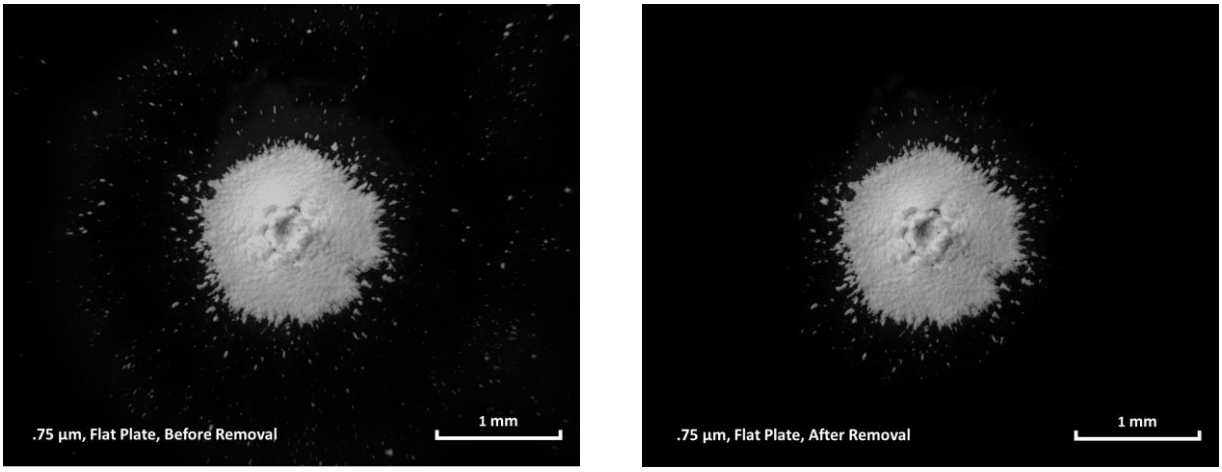

a **b**

Figure 3.4. Collection sites for 0.75 µm particles. The particles are collected on the flat plate, the particles collected outside the prescribed area (diameter of the micro-well) are removed by wiping. (a) as collected; (b) after removing particles from outside the collection area.

The collection efficiencies are calculated by comparing the bulk fluorescence of particles captured on the reference filters and in the collector, similar to Kesavan, et al. [130]. In all cases, only the particles collected in the µ-well for µ-well cases and the defined area (about 1.5 mm in diameter) for flat plate cases are considered. To eliminate the influence of particles impacted outside the µ-well, the area around the µ-well and the defined area are cleaned with the pointed tip wet cotton swab (22CW73, LSS, Lake Forest, IL). A typical collection site for the flat plate collector before and after wiping can be seen in Figure 3.4, which shows that most of the particles were preserved from wiping. Although wiping can introduce some human error, the results show very high repeatability. Particles in µ-wells as well as on the reference filters are first eluted with 10 mL of 0.05% Tween 20 solution using 50 mL centrifuge tubes. The centrifuge tubes containing microscope slides and reference filters are first placed in an ultrasonic bath for 5 minutes, followed by 5-minute shaking in a vortexer. Additional elution

steps do not produce any significant increase in fluorescent signal. A 2 mL volume aliquot of 10 mL volume is then transferred into a 12 mm × 75 mm borosilicate glass cuvette, and the solution fluorescence is measured with the spectrofluorometer (Sequoia-Turner model 450). The calibration of the spectrofluorometer and the flow meters is confirmed before and after each experiment.

3.1.2 *Results and Discussion*

3.1.2.1 Numerical Results for the Effect of Micro-well Angle

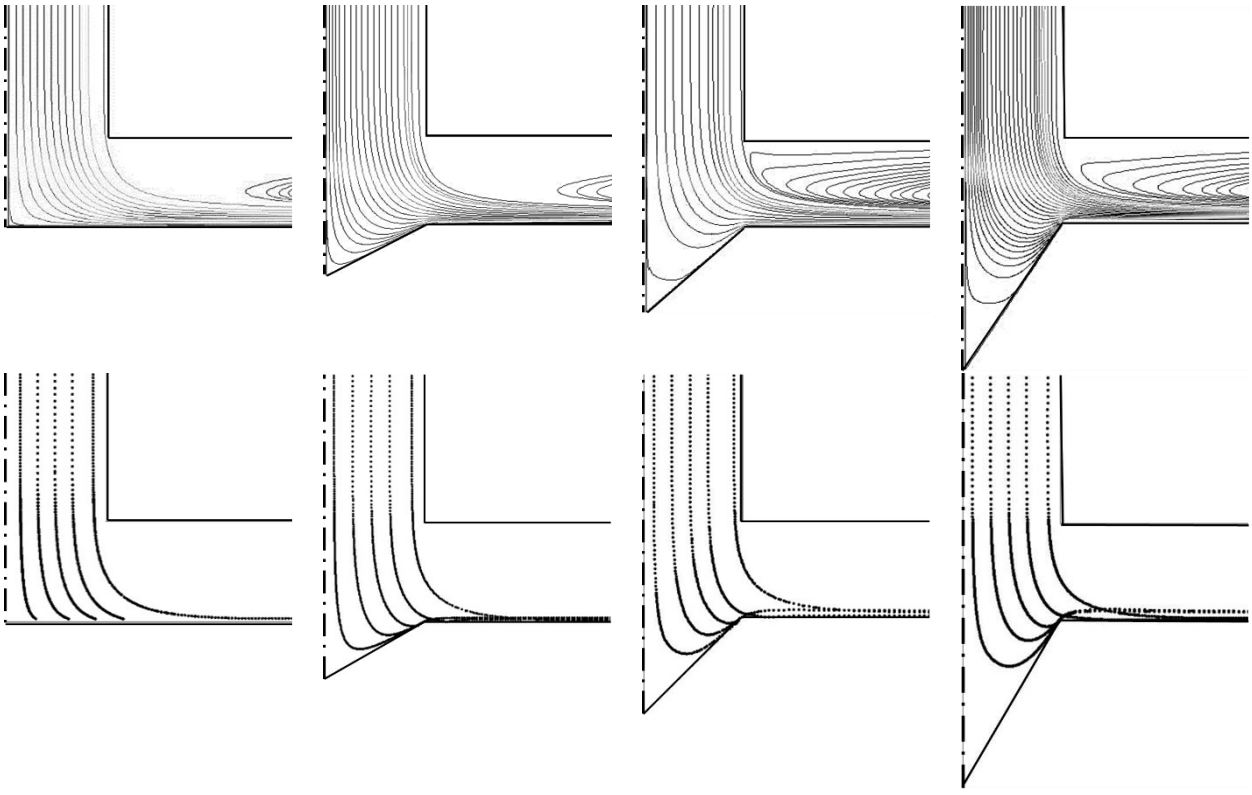

a **b** **c** **d**

Figure 3.5. Top: Streamlines; Bottom: Trajectories of 1.5 μm particles released from same locations for different impactors, flow rate is 1slpm: (a) Flat impactor; (b) 30 degree; (c) 45 degree; (d) 60 degree μ-well impactor. Note: only half of the geometry is shown; dash lines are axial-symmetric axes (Nozzle diameter: 1 mm; Re=1815).

The flow recirculation zones and the uncertainty about the particle position in the flow field significantly hamper the ability to study the effect of the μ-well angle on the particle

trajectories using analytical methods. One can gain insight into the details of particle behavior using CFD simulations. The optimization study is performed for µ-well angles of 30, 45, 60 degrees, and the flat collector. Figure 3.5 shows that the flow streamlines do not penetrate to the bottom of the well, indicating the presence of the recirculation zone at the bottom of the geometry. The upper boundary of the recirculation zone is further from the nozzle for greater well angles. Figure 3.5 also shows an example of the 1.5 µm particles trajectories; for clarity, only the region near the impaction plate is shown. For a particle to impact the surface, it has to gain enough momentum in the acceleration region to overcome the drag caused by the decelerating flow approaching the impaction plate. In the µ-well, the physical dimension that the particle needs to travel increases with the well angle. This explains the similarity of particle trajectories in Figure 3.5c and Figure 3.5d. Figure 3.6 shows the air velocity magnitude at the collector axis of symmetry. The flow starts deaccelerating at the exact location regardless of the angle of the µ-well. This implies that the large well angle is likely to have a lower collection efficiency or larger particle cut-off size.

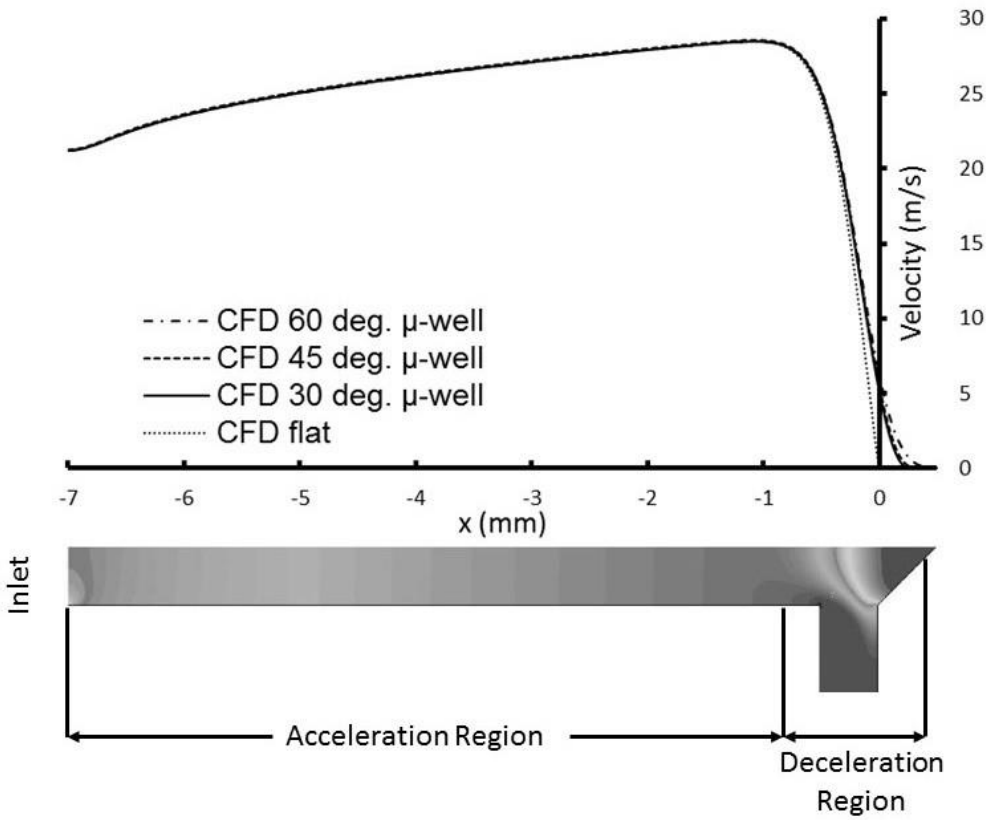

Figure 3.6. The air velocity magnitude along the axis of impactors with different angles. The contour plot of the 45-degree impactor is shown on the bottom to indicate different regions.

Figure 3.7 shows the comparison of the collection efficiencies from the numerical simulation for different micro-well angles. As expected, the CFD simulation shows that the addition of the μ-well does not increase the collection efficiency due to the increased distance that particles need to travel to impact. Without considering the particle bounce and the particle trapping in the recirculation zone, the μ-well increases the cutoff size of the impactor. The collectors with 30-degree and 45-degree angles show very similar trends, while the 60-degree collector has significantly lower collection efficiency. The data are plotted as the function of the square root of the Stokes number in Figure 3.7b. The distances from the nozzle to the bottom of the μ-well are used as the characteristic dimension in the Stokes number calculations. The data

collapse onto a sigmoid curve as a function of the particle Stokes number, which validates the use of the impaction distance as the characteristic dimension in the Stokes number calculation.

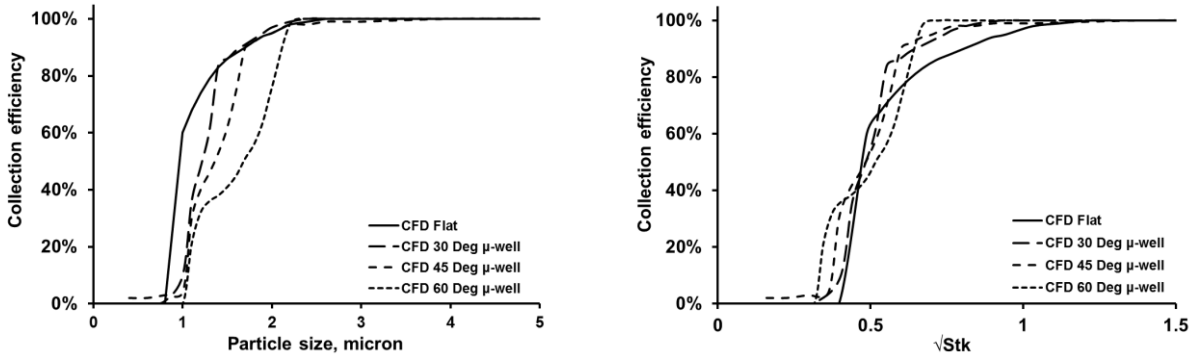

a **b**

Figure 3.7. Calculated collection efficiencies of µ-well impactors with different well angles at a flow rate of 1 slpm (Nozzle diameter: 0.8 mm; Re=1815).

3.1.2.2 Numerical Results for Micro-well Impactor with the Aerodynamic Focusing Inlet

The µ-well impactor is coupled with an AF inlet to improve the collection and concentration of the collected sample in the small region. Focusing particles into the centerline of the jet allows the particles to accelerate to a higher speed, which enhances particle impaction or trapping in the recirculation zone inside the µ-well. The series of CFD simulations are used to study the effect of the AF inlet on the performance of the µ-well collector. The µ-well angle is chosen to be 45 degrees based on the previous well angle study. The collection area is set to be 1 mm in diameter. Other dimensions of the geometry used in the simulations are listed in Table 3.1. The flow rates in both cases are set to be 1 slpm. The uniform velocity profile and pressure outlet boundary conditions are used in the simulation. The particle size range in the simulations is 0.4-5 µm. Figure 3.6 shows a typical result for the air streamlines in the impactor. The colormap represents the air velocity magnitude in m/s. Figure 5 shows the trajectories of particles released from the inlet for the different impactors. The AF inlet focused particles into

the center of the nozzle, which increases their speed and the collection probability. However, some larger particles (Dp >2 µm) injected near the wall can be lost on the forward-facing step of the AF inlet, reducing the collection efficiency. This can be addressed by incorporating another focusing step, which is beyond the scope of this paper.

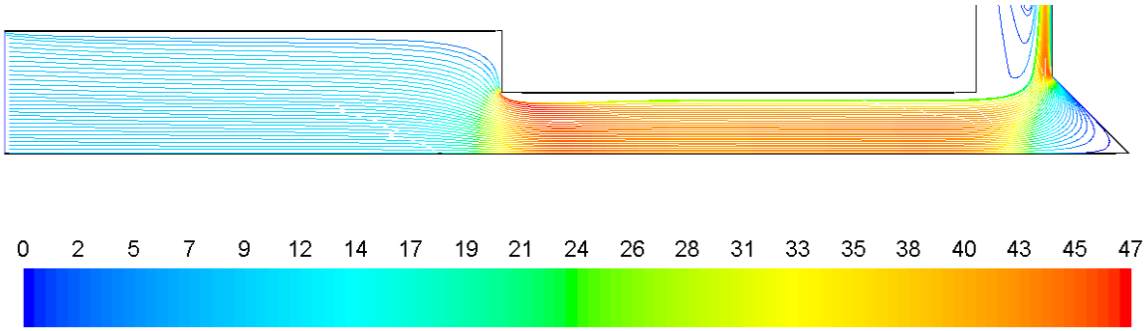

Figure 3.8. Gas streamlines; The colormap represents the air velocity magnitude in m/s (Nozzle diameter: 0.8 mm; Re=1815).

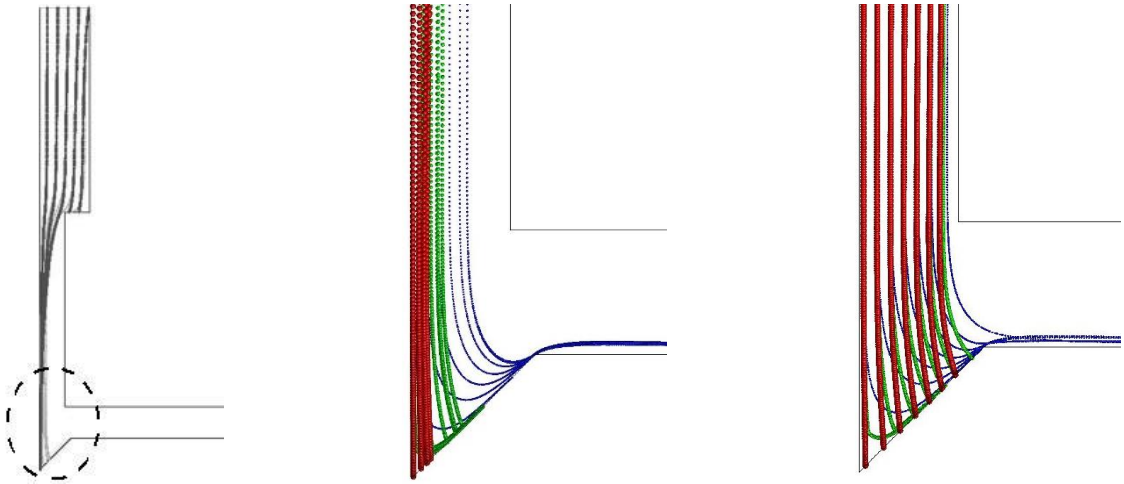

a **b** **c**

Figure 3.9. Trajectories of particles in different impactors at 1 slpm. (a) particle trajectories in the AF µ-well impactor. The dashed area is expanded in (b) to show the details; (c) a detailed view of the particle trajectories for the µ-well impactor with a straight nozzle. Particle size: red line – 3 µm, green line – 2 µm, blue line – 1 µm (Nozzle Diameter: 0.8mm; Re=1815).

Figure 3.10 shows the plot of the calculated collection efficiencies for all four collectors. The boundary conditions and particles used in the simulations are the same as mentioned before. Particles larger than 1.5 µm have 100% collection efficiencies for the non-AF flat plate impactor.

The AF flat plate impactor and non-AF flat plate impactor have nearly the same cut-off size of around 0.8 µm. However, due to the particle loss in the AF inlet, the collection efficiency decreases for particles larger than 1.5 µm. On the other hand, the AF inlet reduces the cutoff size of the µ-well impactor from 1 µm to .8 µm due to the increased particle speed in the nozzle centerline. The AF losses are the same as for the flat plate collector. Again, these are the results without considering particle bounce. In real life, particle bounce plays a significant role in the aerosol collection, demonstrated in the following section.

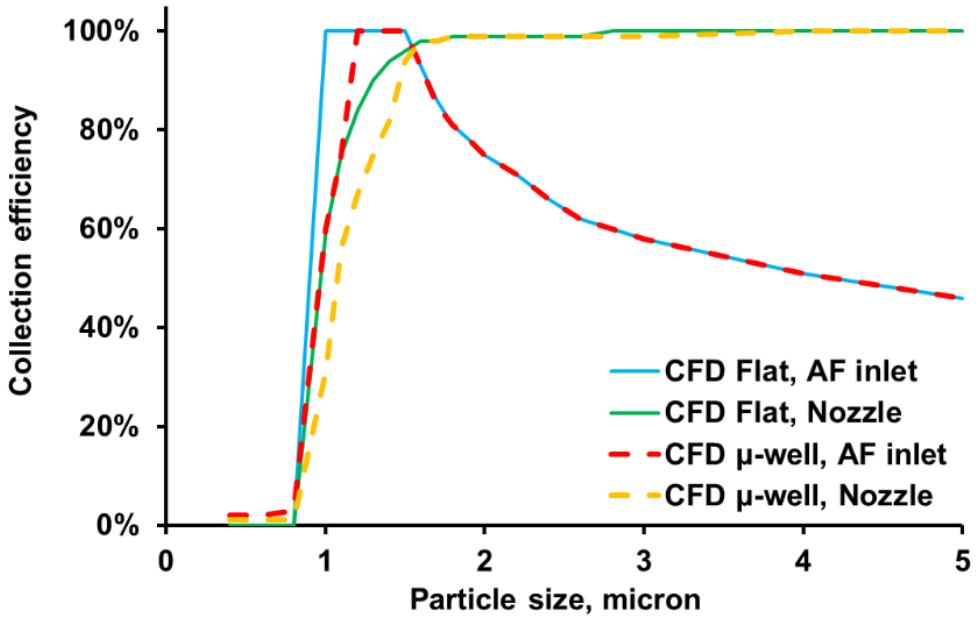

Figure 3.10. Calculated collection efficiencies as the functions of the particle size. The AF inlet improves the collection efficiency for the µ-well impactor and the flat plate impactor (Nozzle diameter: 0.8 mm; Re=1815).

3.1.2.3 Experimental Results for Particle Collection

The experimental results are presented for four geometries, as seen in Figure 3.1. The results are compared with the numerical simulations described above. Notably, the flow field in the experiments is not perfectly axisymmetric as it is in the simulation, which may change the

behavior of the flow around the µ-well. However, the effect of the non-axisymmetric flow behavior outside the collection region was found insignificant. Four impactors of the same geometry are tested in each experiment. Because the experiments focus on verifying the performance of the AF µ-well collector, the AF µ-well collection experiment is repeated at least three times to obtain 12 independent measurements for each condition. At least four independent measurements are made for other geometries to compare with the AF µ-well case.

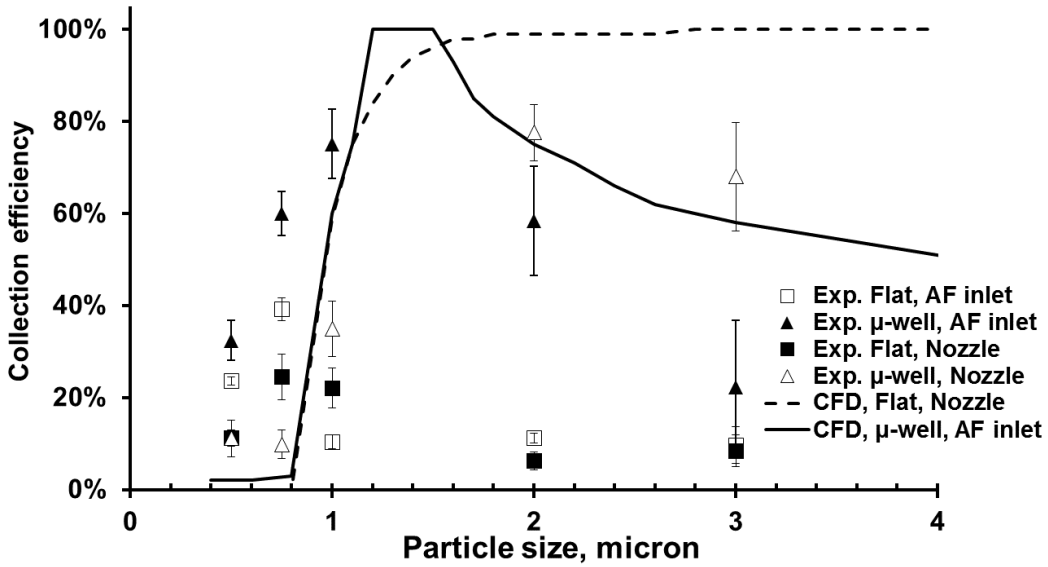

Figure 3.11. Comparison of the experimental and calculated collection efficiencies of µ-well inertial impactors and the flat impactor (Nozzle diameter: 0.8 mm; Re=1815).

The experimental results follow the trend of the numerical prediction for the µ-well cases. The actual collection efficiencies for the flat plate collector are dramatically different from the simulation results because of particle bounce. Figure 3.11 compares the efficiencies from the CFD modeling and experimental data from the aerosol chamber experiments as a function of particle size. The experimental collection efficiency is higher than predicted for particles smaller than 1 µm and is lower than those larger than 2 µm. The experimental 50% cutoff is between 0.5 and 0.74 microns, lower than the simulated CFD results, which shows the cutoff of about 1

micron. The maximum combined collection/elution efficiency is recorded for 1-micron particles (the average values are 75%). The difference in the collection efficiency between the CFD and the experiments may be due to several factors, including the possible slight misalignment of the inlet with the µ-well during the assembly, potential flow instabilities that cause the flow to hug one wall, and for a particle to miss the µ-well. Interestingly, the experimental efficiency for smaller particles is higher than when simulated by the CFD. The CFD model is likely not equipped to predict the particle-flow interaction; the turbulent dispersion-driven particle capture, which is not included in the CFD model, may also play a role if local turbulence and instabilities exist in the flow. The collection efficiency of the nozzle µ-well collector is higher than that of the AF µ-well collector. The difference can be attributed to the particle loss on the forward-facing step in the AF µ-well collector. 3 µm particles have enough inertia to penetrate through the low-speed zone in the well, which makes the AF inlet act negatively on the particle collection. However, the AF inlet is necessary for µ-well to collect smaller particles.

The primary goal of the collector design is to enable the optical interrogation of the collected aerosol in-situ. The high particle density and knowledge of their location on the collection substrate are significant. While the CFD simulation of the particle trajectories and their interaction with the free flow is relatively straightforward, it is challenging to model particle surface interaction because of the limitation of particle tracking schemes. The preliminary simulation that included the particle bounce model has shown that the location of particle capture is highly dependent on the bounce characteristics: angle of and particle energy lost during the bounce process. These characteristics depend on the particle and the surface properties and would not be the same for all aerosols and surfaces. Thus, in this research, we have experimentally compared the collection region for the µ-well impactor and the collection

region of the flat impactor. As in the collection efficiency experiments, PSL microspheres are used. The experiments are performed in the aerosol chamber; the humidity in the chamber did not exceed 50% to ensure that the liquid menisci form at the particle deposition sites.

From the simple geometric considerations, a 45-degree of the well wall and a specular particle collision assumption result in the particle being reflected towards the center of the well. Any loss of the particles would be a result of a particle impacting on the outside of the well or if the well is overfilled with the collected aerosol. The latter scenario is unlikely due to the dilute nature of the atmospheric aerosols and not important from practical considerations since enough signal can be obtained if the well walls are fully coated. Figure 3.12 shows the comparison of particle collection sites of the flat plate impactor with the nozzle and AF μ-well impactor for 0.5, 1, and 2-micron particles at a 1 slpm flow rate.

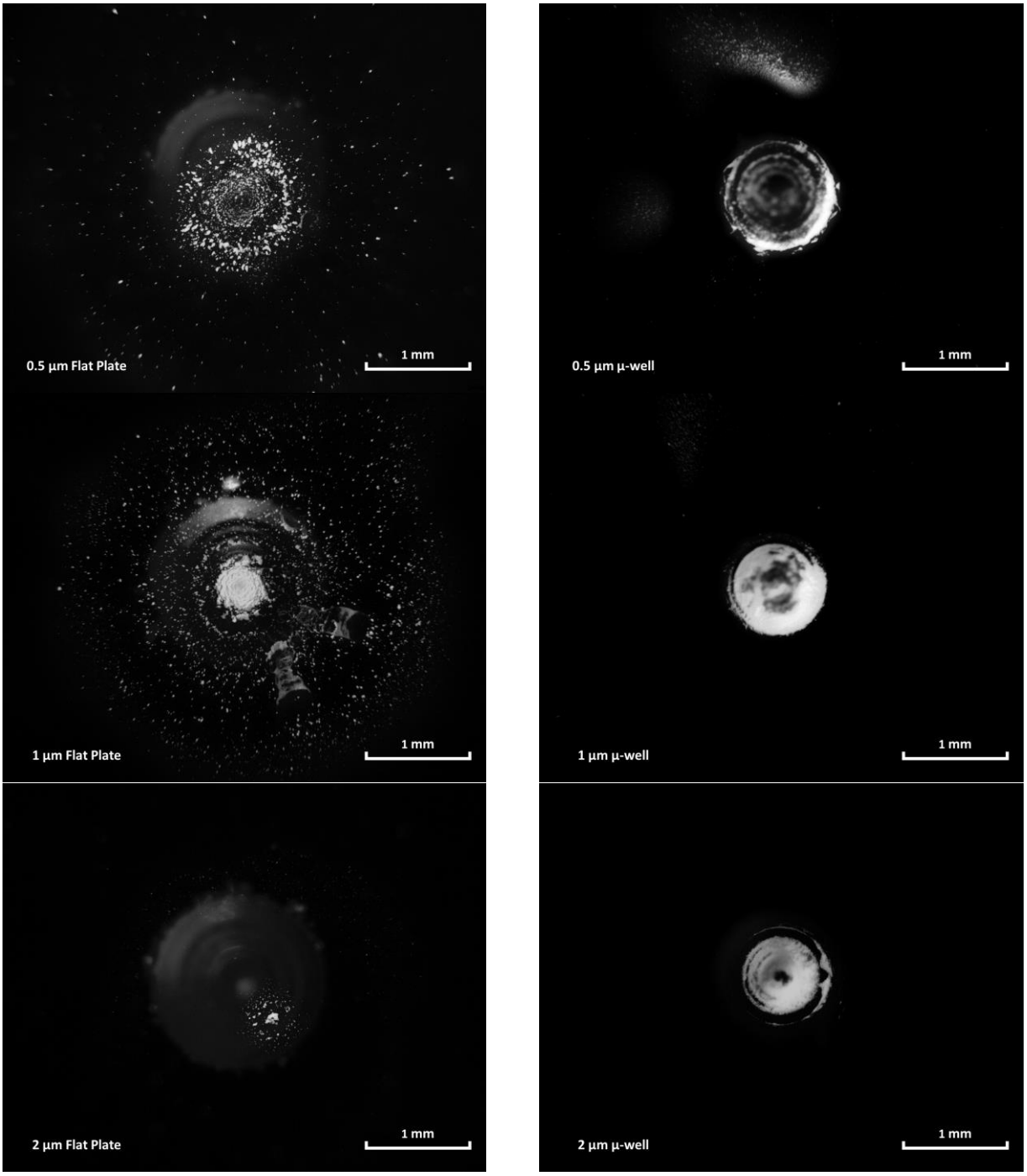

a **b**

Figure 3.12. Particle collection sites for 0.5 µm (top), 1 µm (middle), 2 µm (bottom) at 1 slpm flow rate. (a) flat plate impactor with the nozzle; (b) µ-well impactor with the AF inlet. (1 mm scale).

These tests compare particle deposition characteristics; PSL spheres are used. However, we expect that the trend would hold for the other particle type. Environmental and operational

conditions, such as flow rate and humidity, may influence the deposition patterns. From the experiments with PSL particles, two major observations can be made:

(i) As designed, the combination of the AF inlet and the angle of the µ-well wall enables trapping the aerosol inside the well structure. The µ-well feature collects nearly all the particles, regardless of their size in its submillimeter diameter region, while the flat impactor has a significant dispersion of the collected aerosol.

(ii) The dispersion of the particles collected on the flat collector slide depends on the particle size. The 0.5 µm particles have a collection region of 1 mm diameter and significant dispersion from the center of the jet due to the bounce and jet spreading near the plate. Most of the 1 µm PSL spheres are collected in the middle, likely due to a sweet spot in the operation of the inlet; however, some dispersion is observed. The 2 µm particles show the lowest collection density, which can be explained by the increased bounce of the 2-micron particles due to their impaction velocity.

3.1.2.4 Stoke Analysis of the Collection Efficiencies

Impactor performance can be characterized by the Stokes number, which relates the particle stopping distance to the characteristic dimension of the geometry. In general, particle trajectories for curvilinear motion have been described in Hinds [1], which uses the nozzle radius in the Stokes number calculation. Using the nozzle radius rather than the characteristic dimension of an obstacle is based on the argument that the jet expands only slightly until it reaches within about one jet diameter of the impaction plate. This argument is probably valid for impactors with a larger nozzle-to-plate distance. However, if the impactor with the nozzle is placed close to the impaction plate, the nozzle-to-plate distance can be directly compared with the particle stopping distance, and it is more appropriate to use the nozzle-to-plate distance in the

Stokes number calculation. In this work, we use nozzle-to-plate distance for the flat plate case, and the distances from the nozzle to the bottom of the μ-well are used for the μ-well cases. For AF cases, the calculated magnitudes of the particle velocity on the centerline of the nozzle are used in the Stokes number calculation. The velocity choice is based on the observation that most of the particles are focused into the center of the nozzle by the AF inlet. Figure 3.13 shows the collection efficiency as a function of the square root of the Stokes number. The simulation data collapse onto a sigmoid curve with the cut-off $\sqrt{Stk} \sim 0.4$ for μ-well collectors vs. $\sqrt{Stk} \sim 0.49$ for flat plate collectors. The shift of the cut-off curve is caused by the increase of the physical dimension particles need to travel before impaction.

The experimental particle Stokes number is calculated in the same way as the simulation data. The flat collector exhibits reduced particle collection for the $\sqrt{Stk} > 0.4$ due to the particles' bounce. This result agrees with Rennecke and Weber [131], who demonstrated the increase in a bounce for particles with a greater Stokes number. In addition to the particle Stokes number, the bounce characteristics depend on the particle and surface properties and the environmental conditions [132]. The μ-well collector does not have a sharp cutoff for particles with the larger Stokes numbers (higher impaction velocity magnitude); the particle bounce is redirected towards the bottom of the well, resulting in particle trapping inside the μ-well structure.

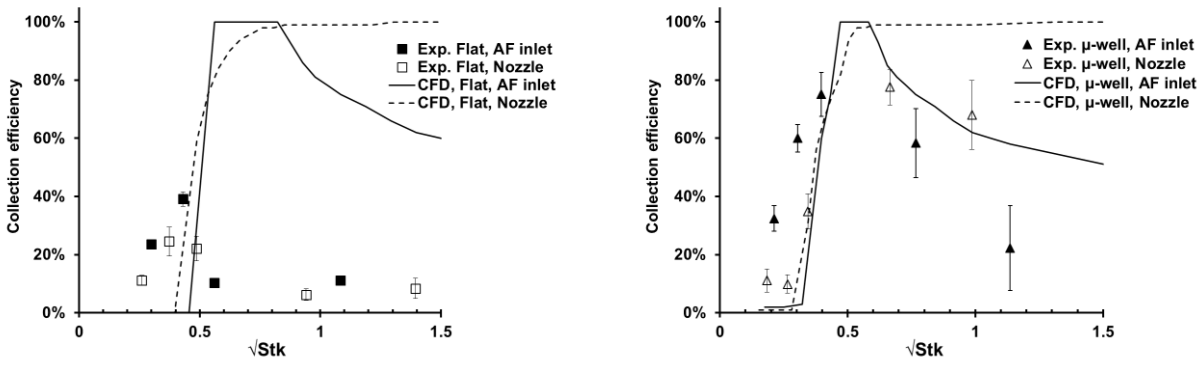

a **b**

Figure 3.13. Comparison of calculated and experimental collection efficiencies of impactors as a function of the square root of Stokes number. (a) flat plate impactor; (b) μ-well impactor.

3.1.2.5 μ-Well Collector Pressure Drop

To estimate the power consumption and aid with the pump's selection, we have evaluated the μ-well collectors for pressure drop as a function of the flow rates. Figure 3.14 shows the measured pressure drops for straight nozzle impactors and AF inlet impactors. In both cases, the diameters of the nozzles are 0.8 mm. Note that the straight nozzle has a 45-degree funnel (3.25 mm in depth) before it. The length of the straight nozzle is equal to the length of the second stage of the AF inlet. Three impaction plate geometries are tested for each inlet geometry. The inlet geometry mainly determines the pressure drop difference. The pressure drop is measured using a Magnehelic gauge (Series 2100 Magnehelic® Differential Pressure Gage, Dwyer, Michigan City, IN). Three measurements are performed per operating condition; the measurement error did not exceed 5%. The error bars are not plotted to remove the clutter. The pressure drop in the straight nozzle geometry is primarily due to the friction losses in the nozzle and the abrupt change of the flow direction at the impaction plate. The additional pressure drop in the AF inlet results from the friction loss associated with the vena contract region. The pressure drop is

consistent for the μ-well and flat plate collector; this indicates that significant collector loading does not increase the pressure drop, unlike filter collection, see Payet, et al. [133].

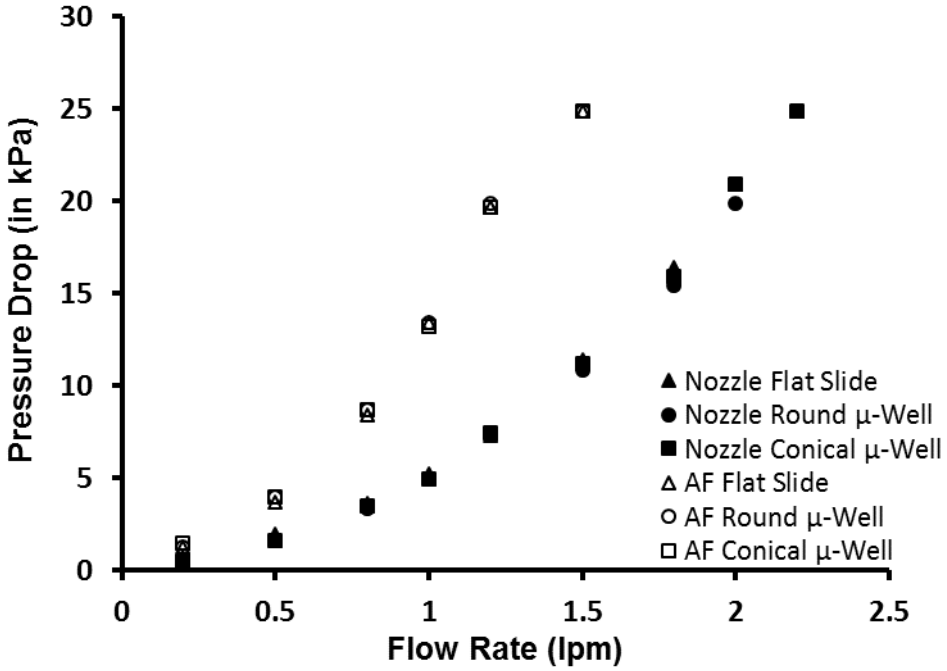

Figure 3.14. Measured pressure drop of different impactors.

3.1.3 *Conclusions on the microwell collector design*

We designed and evaluated a novel μ-well aerosol collector combined with an AF inlet to collect fine PM fraction. The iterative CFD simulations are used to guide the design and optimization of the device. The modification in the collector geometry is compared with the base case of flat collection plates and straight inlet nozzles. The introduction of the μ-well by itself does not increase the performance of the collector. The effect of the μ-well angle on particle collection is studied; the simulations show that the increase of μ-well angle passed 45 degrees resulted in adverse effects on particle collection due to the increased impaction distance. The particles on the centerline of the nozzle are more likely to be collected due to their higher magnitude of particle velocity. Thus, the addition of the aerodynamic particle focusing before the

aerosol exits the nozzle yields significant improvements in device performance. The 45-degree conical-µ-well coupled with the AF inlet is elected to be the final collector prototype geometry. The design of the device is also based on practical considerations for sample analysis; the inlet dimensions are compatible with the pipette tip allowing for ease of sample elution.

The CFD simulations show that the AF µ-well collector has 50% collection efficiencies for 1 µm particles and close to 100% for particles larger than 1.5 µm particles. However, the collection efficiency decreases at about 2 µm because of the particle loss in the AF inlet. Laminar flow CFD simulations under-predict the experimentally determined collector performance for smaller particles, possibly due to inadequacies in the particle tracking models and the presence of unsteady flow characteristics in the µ-well.

The AF µ-well collector can collect highly concentrated particle samples in a 1 mm in diameter collection site. Particles stay in the well because their bounce is redirected toward the center of the well, increasing the sample collection density. The collection efficiency of the µ-well collector shows a minor dependency on the particle bounce when compared to the flat impactor. The flat collector exhibits the reduced particle collection for the $\sqrt{Stk} > 0.4$ due to the particle bounce. In addition to the particle Stokes number (or impaction velocity magnitude), the bounce characteristics depend on the particle and surface properties and the environmental conditions. The roughness of the µ-well surface may contribute to the particle collection by modifying the particle bounce characteristics. Further studies are needed to quantify the effect of surface roughness on particle collection. The sampling efficiency of the µ-well impactor is tested under relatively low particle loading scenarios. Therefore, additional work may be required to estimate collector overloading/fouling characteristics. However, our laboratory test in the highly-concentrated aerosol environment (about 8000 particle/cm^3 for 1 µm particles) and the

preliminary environmental tests did not show significant overloading. The total volume of the µ-well is 0.13 mm^3, which translates to the µ-well capacity of 130 µg. Assuming the sampling flow of 1 slpm, the collection efficiency of 50%, the aerosol concentration of 10 $\mu g/m^3$, and the density of the water particle, the sample time required for filling the µ-well is more than 400 hours of sampling. The particle packing density in the collector is not considered in the order of magnitude analysis.

3.2 FINE PM COLLECTION - DESIGN AND EVALUATION OF AN AERODYNAMIC FOCUSING MICRO-WELL AEROSOL COLLECTION CARTRIDGE

Bioaerosol sampling and identification are vital for assessing and controlling airborne pathogens, allergens, and toxins. In-situ analysis of chemical and biological particulate matter can significantly reduce the costs associated with sample preservation, transport, and analysis. The analysis of conventional filters is challenging due to dilute samples in large collection regions. A low-cost cartridge for collecting and analyzing aerosols is developed for epidemiological studies and personal exposure assessments. The cartridge collects aerosol samples in a micro-well, reducing particles losses due to the bounce and not requiring any coating. The confined particle collection area (diameter~1.4 mm) allows reducing the elution volume for subsequent analysis. The performance of the cartridge is validated in laboratory studies using aerosolized bacterial spores (Bacillus subtilis). Colony-forming unit (CFU) analysis is used for bacterial spore enumeration. Cartridge collection efficiency is evaluated by comparison with the reference filters and consistent with tested flow rates. Sample recovery for the pipette elution is ~80%. Due to the high density of the collected sample, the cartridge is compatible with in-situ spectroscopic analysis and sample elution into the 10-20 µl liquid volume providing a significant increase in sample concentration for subsequent analysis.

3.2.1 *Materials and Methods for µ-well Cartridge Design*

3.2.1.1 Micro-Well Cartridge Design and Fabrication

The micro-well (µ-well) particulate collection cartridge consists of two injection-molded UV-transparent parts. The top half of the cartridge includes an aerodynamic focusing (AF) inlet to accelerate and focus the particles and an outlet to connect to the vacuum pump. The conical µ-well on the bottom half captures particles into a small collection area. Figure 3.16 shows the 3D rendering of the assembled cartridge and the drawing of the cartridge with the dimensions of the AF inlet and the µ-well. The diameter of the AF inlet is chosen based on the calculation of the Stokes number, as well as compatibility with the standard pipette tip. The angle of the µ-well cone of 35 degrees is selected to reduce the effect of particle bounce at the collection location.

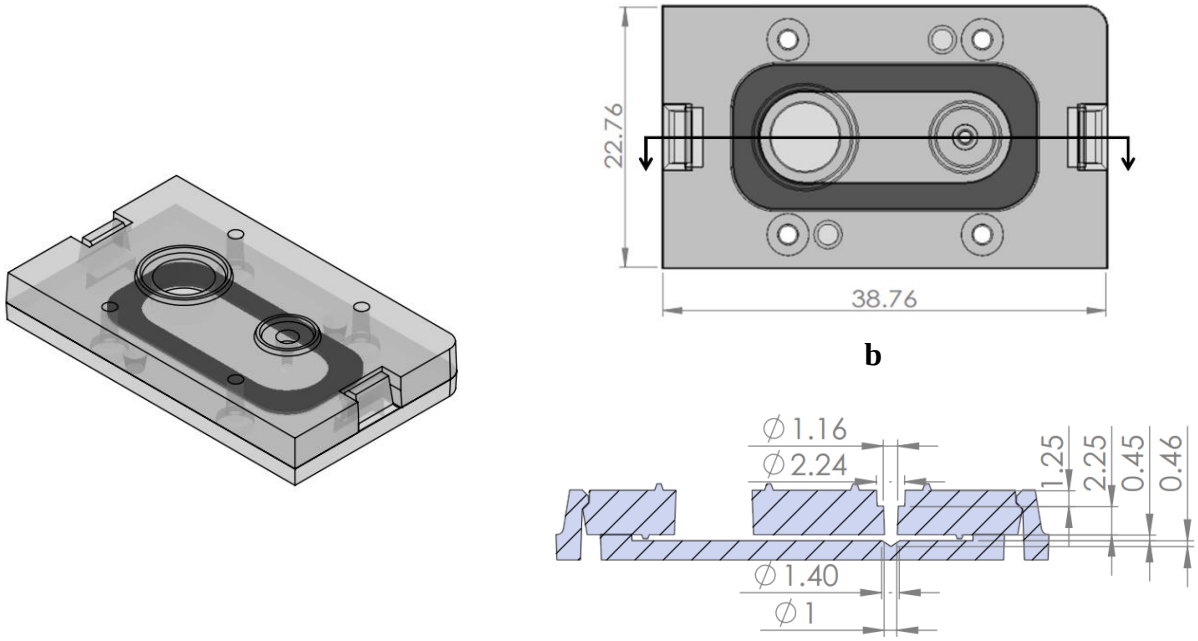

a **b** **c**

Figure 3.15. (a) The µ-well aerosol collection cartridge and (b) the dimensions of the cartridge; (c) the critical dimensions of the AF inlet and the µ-well (unit: mm)

The design of the low-cost µ-well collection cartridge is based on the methodology outlined in our previous work [134]. The range of the operating flow rate for the cartridge is

0.75-2 slpm at standard conditions (293 K, 101 kPa). The principle of operation has been previously described; typical flow field and particle behavior are shown in Figure 3.8 and Figure 3.9. The Stokes number analysis is used to guide the inlet design. If the particle Stokes number of the AF inlet is smaller than the optimum Stokes number, the particles that follow the flow streamlines cannot be effectively focused into the well. In contrast, if the Stokes number is near the optimum value, the particle is focused by the AF inlet and projected into the μ-well. The optimum Stokes number *Stk** was selected to be 1, based on the previous studies [79, 135] and our own work based on the CFD simulations of several focusing inlet geometries and flow rates [134]. *Stk* ~ 0.55 – 0.85 has been reported for aerodynamic focusing using parallel slit geometries [136, 137]. The optimizing parameter is used as the design guidance; it does not account for the variation of the Stokes number in a non-uniform velocity field; in reality, the Stokes number may vary significantly depending on the particle position, its size and density, and the device flow rate. *Stk** is calculated as:

$$\boldsymbol{Stk^* = \frac{\tau}{D_c/U} = \frac{C_c \rho_p d_p^2 U}{18 \eta D_c} \cong 1} \qquad \textbf{(3.4)}$$

where C_c is the Cunningham slip correction factor for the particle, ρ_p is the particle density, d_p is the particle diameter, U is the area-averaged flow axial velocity magnitude at a micro-well upstream location, η is the gas viscosity, and D_c is the characteristic dimension, which, in this case, is the diameter of the nozzle.

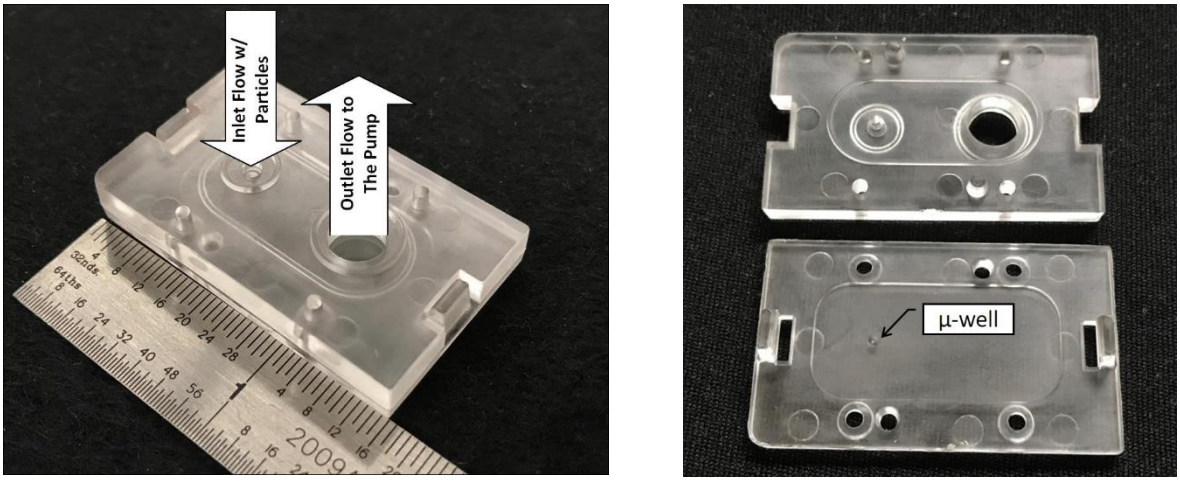

a **b**

Figure 3.16. (a) The photograph of the assembled μ-well aerosol collection cartridge and (b) the cartridge in a disassembled state.

The geometry of the inlet also satisfies the practical considerations of compatibility with a standard pipette tip for the sample elution. The diameter of the inlet is chosen based on the calculation of the Stokes number, as well as compatibility with the standard pipette tip. The angle of the μ-well cone of 35 degrees is selected to reduce particle bounce at the collection location. Our previous study shows that larger angles are more effective for mitigating particle bounce; however, they are less efficient for collecting smaller particles. Figure 3.16a shows the photograph of the cartridge with arrows indicating the flow direction. Figure 3.16b shows the cartridge in a disassembled state to reveal the μ-well on the bottom half of the cartridge.

The μ-well cartridges are fabricated using the injection molding technique. The cost of each cartridge is under $5 for a low production run (n=500) with the aluminum mold used. Each collector is assembled from two molded parts, with a gasket between them. A 0.5 mm thick silicone gasket is used to provide the proper nozzle-to-plate distance; the gasket thickness can be changed to vary the distance between the nozzle and the μ-well, which, in turn, changes the cartridge collection characteristics. The seal between the nozzle and the impaction plate is

achieved by applying compression force from the two snap-on tabs. All collectors are checked for a vacuum seal before conducting the experiments. The dimensions of a collector are about 40 mm × 23 mm × 5 mm. Both the inlet and outlet of the µ-well cartridge are located on the same side of the geometry to permit the easy integration of the collector array and the vacuum manifold, as well as to ensure proper sealing to avoid sample contamination during storage and handling. The overall quality of the injection-molded µ-well cartridge was excellent: the production parts did not have the defects often associated with injection molding, such as sinking, burning, flashing, or short shot. All tested collector assemblies fit together well and provided a good seal for all tested operating pressures. The pressure drop through the collectors was consistent for any given flow rate within the accuracy of the measuring instruments (~5%).

3.2.1.2 Aerosol Chamber Testing

The collection efficiency of the cartridge was evaluated by collecting aerosolized single-organisms *B. subtilis* (ATCC® 31578™ Strain Designation: RUB331) compared to the collection of the reference filters. The collection experiments were performed in a custom 0.3 m^3 stainless steel, well mixed aerosol chamber (see Figure 3.17) for a range of flow rates of 0.75-2.0 slpm. The large volume of the chamber with mixing fans provides well-mixed conditions and allows for the evaluation of multiple collectors simultaneously. The aerosol concentration in the chamber was found to be spatially uniformed with the operation of the mixing fans. Typically an array of six collectors and three reference filters were used in the experiments. The collectors are fluidically connected via an adapter to the mass flowmeters (HONEYWELL, Morristown, NJ, AWM5102VN). The reference filter housed in the filter housing similarly connected house vacuum through the same type flow meters. Three reference filters (Spectrum Poretics® polycarbonate membrane filters, 47mm, 0.6 µm pore sizes) in open face aerosol filter holders

(EDM Millipore, Billerica, MA, model XX5004710) collect particles at 1 slpm in each experiment. All flowmeters are located outside the chamber, allowing for individual control of the flow rate during the experiment. The flowmeters are calibrated before and after each experiment using Gillibrator (Sensidyne, Clearwater, FL, Gilibrator 2). All experiments were performed at the room temperature of 20-25°C and relative humidity in the chamber of 40-60%. Operating flow rates for the cartridges were 0.75, 1, 1.5, and 2 slpm.

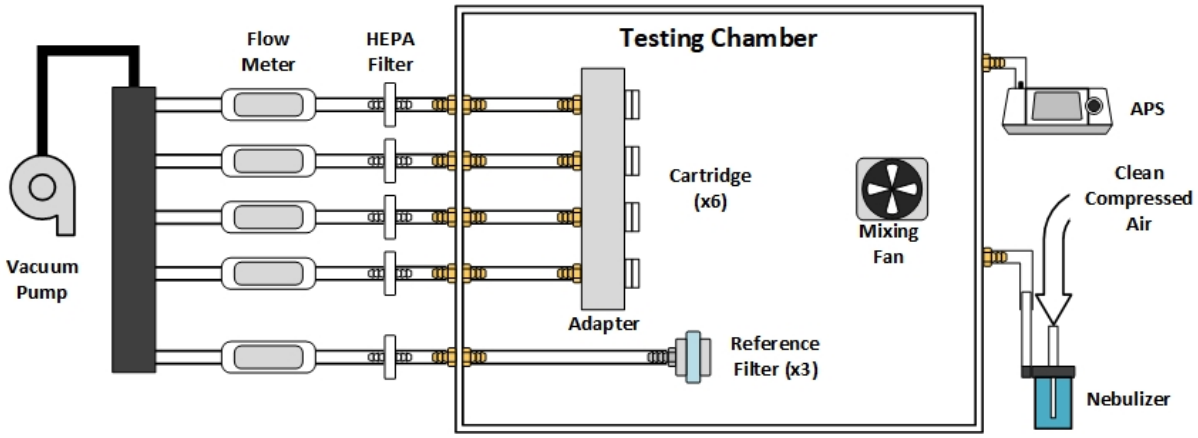

Figure 3.17. The configuration of the aerosol chamber experiment for µ-well cartridge collection efficiency testing.

A *B. subtilis* spore stock was prepared by initially growing the *B. subtilis* overnight in Luria-Bertani Broth (LB) at 37º C in an incubator shaker. The overnight culture was spread on AK#2 sporulating agar, and the plates were incubated for 48 hours at 37º C. The growth was scraped off the plates, and the stock was stored in water at 4º C. The stock was purified by centrifuging at 10,000 G for 10 minutes and washed in cold, sterile water; this procedure was repeated three times. Subsequently, the pellet was shaken overnight at 125 rpm and 4º C, centrifuged for 20 minutes at 20,000 g, and resuspended in the new cold, sterile water. This procedure was repeated for several days until the pellet formed a homogeneous layer. The stock was checked for purity with microscopy using a malachite green spore stain. The purified stock

was stored at 4º C. The prepared bacterial spore suspension was diluted 100x in the distilled water right before the experiment. During the experiment, 4 mL of prepared solution was nebulized from the liquid suspension with 20 psi clean air using a Lovelace nebulizer (In-Tox Products, Moriarty, NM). An aerodynamic particle sizer (APS 3321, TSI, Shoreview, MN) was used to verify the particle size and monitor the particle concentration in the chamber. The aerodynamic diameter of the *B. subtilis* spores was measured by the APS to be about 0.75 μm. APS measurements also confirm that no significant particle agglomeration occurs inside the chamber during the experiment. Figure 3.18 shows a typical particle size distribution during the experiments.

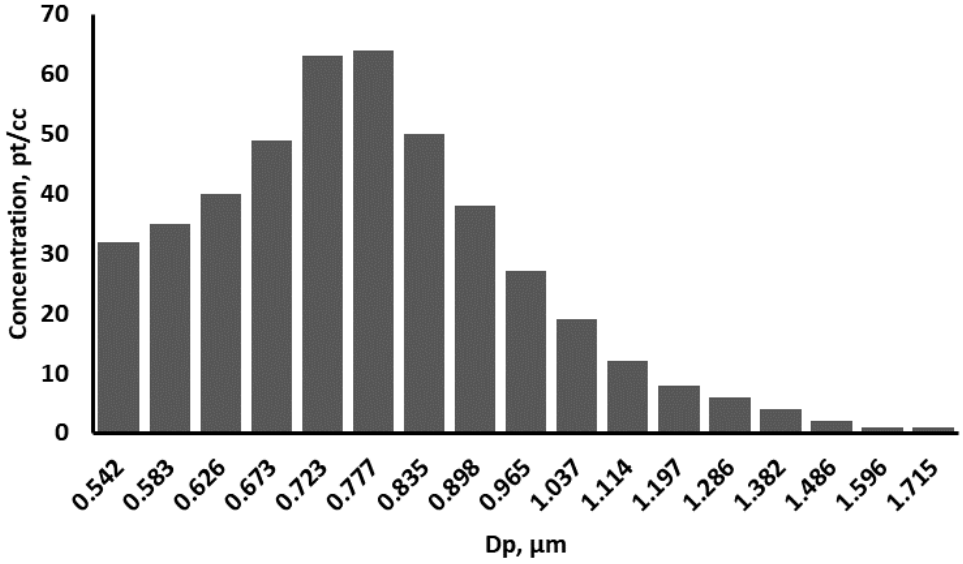

Figure 3.18. The size distribution of airborne particles during one experiment.

Following the collection experiment, two elution steps were performed to remove *B. subtilis* from the collectors. The efficiency of each elution procedure was quantified. The first elution step quantifies the sample collected in the μ-well and the close vicinity (1-2mm) around the well. The second step is used to elute all the particulate matter collected elsewhere inside the

cartridge during the experiment; these include the particles lost on the upper collector part, the gasket, and around the outlet of the cartridge. Small liquid aliquots were used for the first elution: 2 × 10 µl of Phosphate Buffered Saline (PBS) with 0.05% Tween 20. Each 10 µl was added to the collector and immediately pipetted up/down ten times, after which the droplet was placed in a microcentrifuge tube containing 980 µl of PBS and vortexed for 1 minute before diluting in PBS. A second elution consists of disassembling and submerging the entire cartridge in a centrifuge tube with 10 ml of PBS with 0.05% Tween. The centrifuge tube undergoes 10 minutes of shaking on a shaker table, followed by 5 minutes of sonication in a 60 Watts ultrasonic cleaner bath (model #gb928). After the collection, the reference filters were submerged in 10 ml of PBS with 0.05% Tween and underwent a 10-min shaking period, followed by 5 minutes of sonication. While sonication is a recognized method of spore recovery [138, 139], experiments plating dilutions of the *B. subtilis* spore stock show that the sonication step may reduce the spore stock titer by up to 30%.

The elution efficiency and the collection efficiency were calculated by comparing the *B. subtilis* colony-forming unit (CFU) for the cartridge and the reference filter elution; the flow rate adjustments were made to account for differences in sampling rates. The collection efficiencies are calculated based on at least 6 data points from three runs for each flow condition. Mean and one σ error bars are presented in the collection efficiency plot. CFU was quantified on nutrient agar plates by plating 100 µl of the relevant dilutions in duplicate and incubating at 37º C overnight, after which the CFU captured at each flow rate were enumerated. The undiluted sample and a 10x dilution were plated for the first elution of the cartridge; the undiluted samples were plated for the second elution. Both the undiluted and the 10x dilution were plated for the reference filters. In the analysis, the CFU counts were adjusted for the difference in elution

volumes between the first, the most concentrated eluent, the reference filters, and the second elution step.

3.2.2 *Results and Discussion for μ-well Cartridge Design*

3.2.2.1 Pressure Drop

To estimate the power consumption and aid with selecting the pump for the personal exposure monitors, we evaluated the cartridge for pressure drop as a function of the flow rates. Figure 3.19 shows the measured pressure drop for the cartridge and the pressure drop predicted by the computational fluid dynamics (CFD). The pressure drop was measured using a Magnehelic gauge (Series 2100 Magnehelic® Differential Pressure Gage, Dwyer, Michigan City, IN). Three measurements are performed for each operating condition; the measurement error did not exceed 5%. The experimental pressure drop of the low-cost cartridge was compared to the results of the computational fluid dynamics study performed during the design stage [134]. The results show excellent agreement between the computational and experimental pressure drop measurements. The cartridges are evaluated for potential failure due to the collection overloading. The pressure drop of an overloaded cartridge was consistent with the blank one; this indicates that loading of the collector does not increase the pressure drop, unlike filter collection [133].

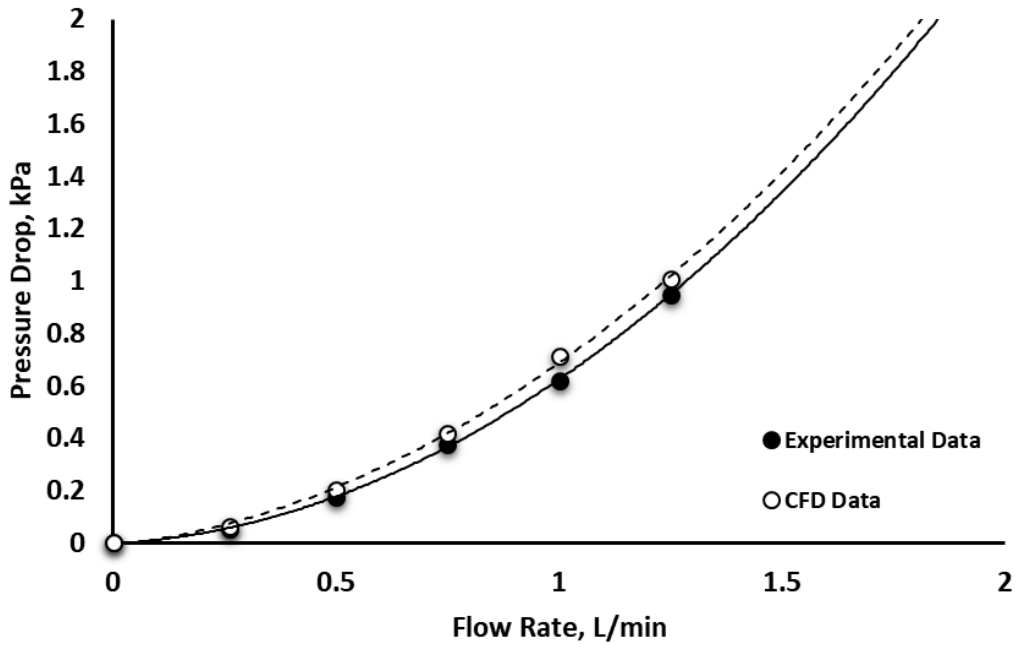

Figure 3.19. The measured pressure drop of the collection cartridge at different flow rates.

3.2.2.2 Bacillus Subtilis Collection Efficiencies and Analysis

The collection efficiencies are presented in Figure 3.20. The results show that the collection efficiency for the B. subtilis spore increases with the flow rate. At a flow rate of 0.75 slpm, the cartridge collects about 35% of the B. subtilis spores as compared to the number collected by the reference filter. The maximum collection efficiency observed is ~80% at the highest flow rate tested (2 slpm). The results are consistent with the inertial mechanism of particle capture. The particle with the lower Stokes number, associated with the low velocities in the focusing inlet, cannot reach the μ-well wall [134]. Higher sampling rates are desired to improve the capture efficiency of single-organism bioaerosols. Unlike conventional impactors without coating, no significant collection efficiency drop associated with particle bounce is observed in the collection of B. subtilis as most of the spores were recovered from the direct well elution (elution 1). Less than 25% was recovered during the second elution when the cartridge was disassembled and sonicated. The limited particle loss from the targeted collection area can

be attributed to the µ-well angle, which redirects the bounce toward the bottom of the well and dramatically eliminates the particles from re-entering the primary flow.

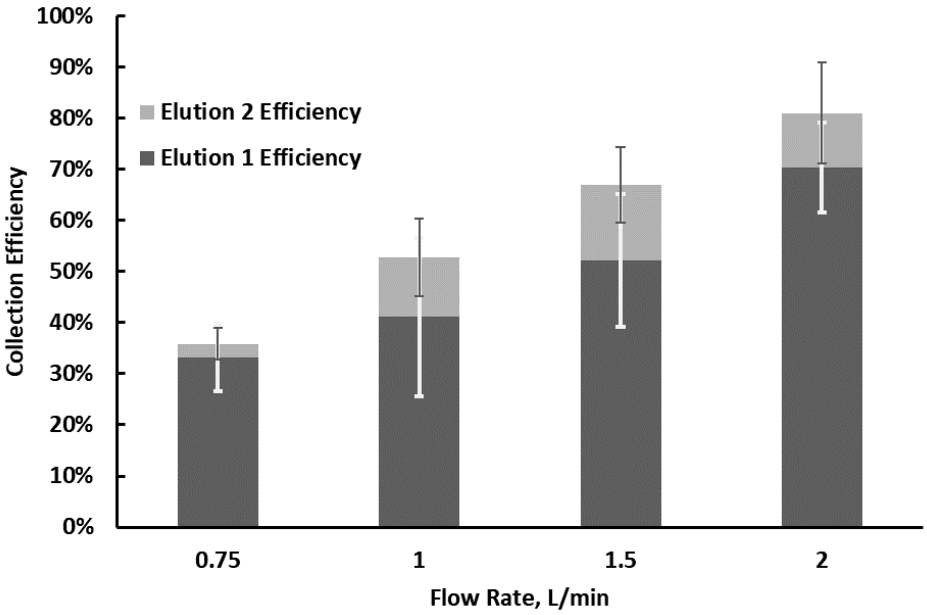

Figure 3.20. *B. subtilis* collection efficiencies in µ-well inertial impactors as a function of the collector flow rate.

The μ-well cartridges were tested for their usability in a pilot field study, in which the PM samples were collected from users for the assessment of the health risks related to PM exposure. Figure 3.21 illustrates the differences in PM collected for two of the users, with high versus low exposures. Though the preliminary results from the chamber experiments and the pilot indoor and outdoor sampling show significant sample accumulation in the μ-well, the bounce mechanisms for biological and other particles need further investigation. A single pipette elution extracts more than 75% of the B. *subtilis* collected in the μ-well cartridge for all tested conditions. The small elution volume is beneficial for bioaerosol sampling providing two to three order magnitude preconcentration of the analysis volume.

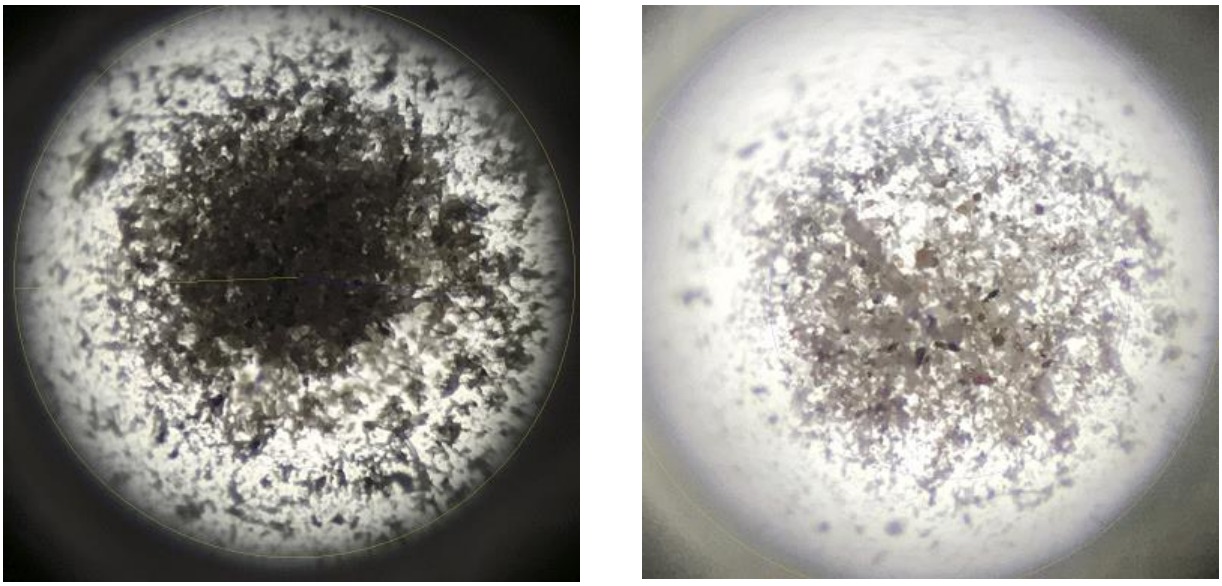

Figure 3.21. Microscopic images of PM collected in the cartridges during the one-week usability study.

In a proof-of-concept experiment to test cartridge's compatibility of the in-situ optical analysis, the fluorescence measurement of polystyrene latex (PSL) microspheres was performed. Figure 3.22a shows the schematics of the fluorescence measurement setup and the fluorescence spectrum from the PSL particles. The 2 μm fluorescent particle (Polysciences Inc.) were aerosolized in the hermetically sealed chamber and collected at 1 slpm, which results in a dense

cluster of particles as shown in Figure 3.22b. The sample collected in the µ-well was then excited with the 440 nm light from the bottom at the 45-degree incident angle. The excitation light was generated by passing the DH-2000-BAL deuterium halogen light (Ocean Optics, Dunedin, FL) through a linear variable bandpass filter (Ocean Optics, Dunedin, FL). The Flame NIR spectrometer (Ocean Optics, Dunedin, FL) was used to analyze the emission light from the sample collected through an optical fiber probe placed above the µ-well. The yellow-green PSL particle has the maximum excitation at about 440 nm and the maximum emission at about 490 nm. We compared the fluorescence spectrum acquired from the cartridge sample to the spectrum from the liquid sample measured in a quartz cuvette (see Figure 3.22c). The liquid sample fluorescence measurement was performed in the CUV-ALL-UV Cuvette Holder (Ocean Optics, Dunedin, FL) at a 90-degree angle. Most of the scattering signal from the blank cartridge and the solvent was filtered from the spectra; however, some excitation signal is still apparent in the recorded spectra. The spectrum from the in-situ fluorescence measurement on the cartridge shows a good agreement with the spectrum acquired from the liquid sample.

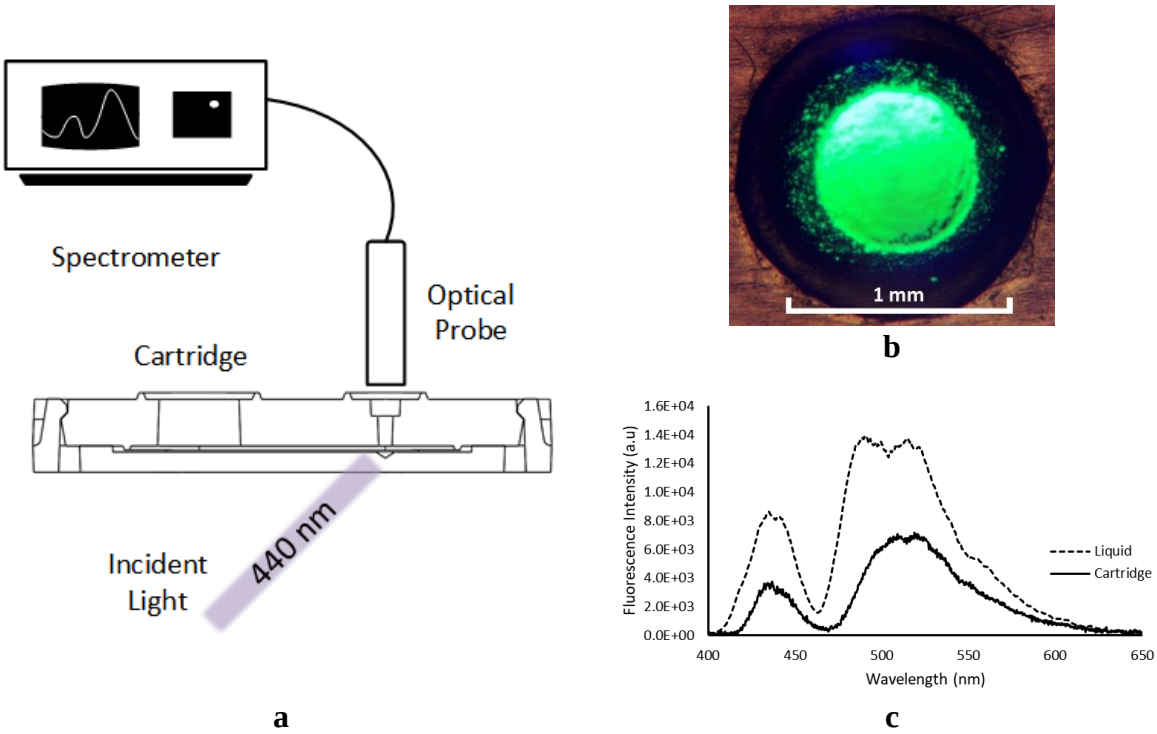

Figure 3.22. (a) The cartridge fluorescence measurement setup and (b) the fluorescent PSL particle collection site; (c) the fluorescence spectrum for the liquid and solid sample.

3.2.3 *Conclusions on µ-well Cartridge Design.*

The performance of a low-cost µ-well aerosol cartridge is evaluated for collection and analysis of single-organism B. subtilis spores. The design of the device is based on practical considerations for sample analysis; the inlet dimensions are compatible with the pipette sample elution and integration with personal exposure monitors. The cartridge collects highly concentrated particle samples in a 1 mm diameter spot. The sample is retained in the well because the particle bounce is redirected toward the center of the well, increasing the sample collection density. Collection efficiency is consistent for each flow condition. Sample recovery for the pipette elution is more than 75%. The elution volume used to recover the collected sample from the cartridge is in the range of 10-20 µl, which provides a high preconcentration of

the aerosol sample for liquid assays; based on the cartridge geometry, the volume can be further reduced if the procedure is automated or microfluidic analysis is desired.

In this study, we used the standard laboratory analysis method, the optically transparent collection substrate, and the well-defined collection region to allow the in-situ optical analysis of the collected aerosols. This in-situ spectroscopic analysis may provide non-destructive orthogonal data such as fluorescent measurement and a significant reduction in analysis cost for monitoring exposure to chemical and biological aerosols, toxic compounds. Our analysis demonstrated the in-situ detection of fluorescent 2 μm PSL spheres collected in the aerosol chamber experiments. Optimizing the optical cell geometry is required to minimize the scatter and reflection from the cartridge surfaces. One promising approach is to use fiber-optic excitation and collect the signal in a backscatter probe configuration; this would significantly minimize the sensor footprint. Multiple reviews on bio and chemical detection using fiber-optic sensors exist, e.g., [140, 141]. Raman backscatter probes are well-developed for in-situ analysis of chemical and biological compounds, e.g., [142-148], and can be readily used with the cartridge without significant hardware modification. Fiber-optic probes for surface-enhanced Raman [149] and anti-stokes Raman [150] have been demonstrated for analysis for the detection of bioaerosols. Sample collected in the μ-well can be an analysis based on native fluorescence of the bioaerosols such as UV LIF [151, 152], though the application of this technique using fiber-optic bundles needs further development.

Chapter 4. EXCITATION EMISSION MATRIX FLUORESCENCE SPECTROSCOPY FOR ESTIMATION OF REACTIVE OXYGEN SPECIES FROM COMBUSTION-GENERATED PARTICULATE MATTER SAMPLES

Particulate matter (PM) in the environment can lead to adverse health impacts, like, cardiopulmonary diseases, neurological diseases, and lung cancer. While the epidemiological link between PM exposure and adverse health effects is clear, there is a lack of information regarding source-specific differences in PM toxicity. Thus, there is a clear need to quantify PM in the environment and identify its sources and toxicity. Sources of combustion generated PM range from wildfires, residential wood burning, traffic emission, etc. Flame temperatures have been linked to changes in particle composition and hence the toxicity. Also, the capacity of combustion-generated PM to produce reactive oxygen species (ROS) has been proposed as one surrogate metric for the toxicity of PM. Currently, the composition of the organic fraction of PM is analyzed using mass spectrometry (MS) methods, which are expensive and time-consuming. Excitation emission matrix (EEM) spectroscopy has been proposed as a low-cost, reliable method for analyzing the organic fraction of PM and source apportionment. This preliminary study investigates the correlation between EEM signatures and ROS measurements for smoke aerosols. PM samples collected from cookstoves and wildfire smoke were analyzed by EEM and the dithiothreitol (DTT) assay for ROS. The results suggest that the fluorescence EEM spectra correlate with ROS level in PM, suggesting that EEM can be an alternative method to evaluate the ROS level in combustion-generated aerosols. This work was performed in collaboration with

Prof Simpson, UW DEOHS; his group performed ROS analysis of the samples. This analysis is presented here for completeness.

4.1 MATERIAL AND METHODS

4.1.1 *Sample Collection and Preparation*

We took 18 samples for three types of smoke sources: (a) 6 samples for the natural-draft cookstove smoke; (b) 6 for the forced-draft cookstove smoke; (c) 6 samples for the wildfire smoke from the 2020 Washington wildfire event, within which three were collected outdoors and 3 -- indoors. All the samples were collected onto 1.0 µm pore PTFE membrane filters (Fluoropore® membrane filters, # FALP03700, 37 mm, MilliporeSigma, Burlington, MA, USA) housed in the Harvard impactor (Cat. # HP2518, BGI, Butler, NJ, USA) sampling cassettes placed in the sealed chamber. The sampling flow rate was set to 1.8 lpm using the portable vacuum pumps (AirChek XR5000 pump, SKC Inc., Eighty Four, PA, USA). Flowrates were verified using a flow calibrator (Gilian Gilibrator PN# 800268, Sensidyne, St. Petersburg, FL, USA). The woodsmoke samples were collected by burning 1½ by ¾ inch Douglas fir sticks cut from dimensional lumber in side-feed, natural-draft, or forced-draft cookstoves.[91] The sampling devices were placed in a sealed chamber connected to the exhaust duct at the sampling point. The wildfire samples were collected in September 2020 inside a University of Washington building and from the backyard of one lab member of our research group.

The gravimetric analysis was performed to measure total PM mass. Following collection, filters are removed from the samplers and placed in a chamber with 37% (SD = 4%) relative humidity for 24 hours. The filters were then weighed using a micro-balance with 0.5 µg resolution (Mettler-Toledo UMT-2, Greifensee, Switzerland). Initial weights of the filters were recorded in the same manner, and the difference in weights was used to calculate the amount of

$PM_{2.5}$ collected. Filters were then submerged in 7 mL methanol (Sigma Aldrich, HPLC grade) and sonicated for 60 minutes. We prepared a filtered extract and an unfiltered extract for each sample. For a filtered extract, 3.5 mL of solution was pushed through a 0.2 μm syringe filter (VWR Cat. #28145-491) into a 4 mL glass vial to remove insoluble particles. The remaining portion of the solution was transferred into another 4mL glass vial as an unfiltered extract. PM extracts were stored in the vials until analysis. See Figure 4.1

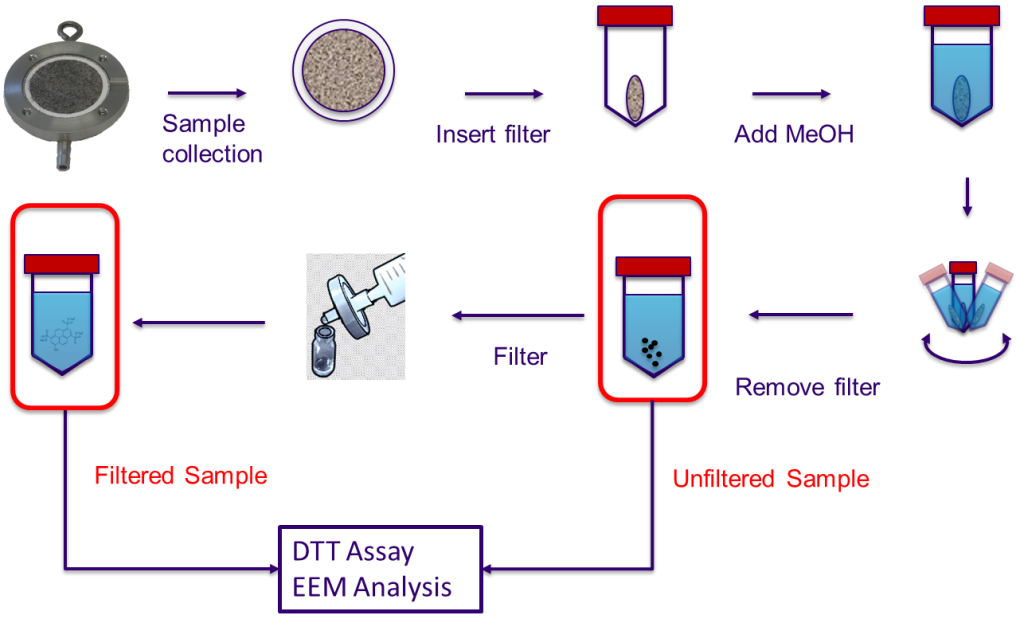

Figure 4.1. Sample preparation for the EEM analysis and DTT assay.

4.1.2 *DTT Assay for Oxidative Potential of ROS*

We measured the oxidative potential of both filtered samples and unfiltered samples using DTT assay. The DTT assay measures the presence or formation of ROS via the formation of the DTT-disulfide [107]. Unreacted DTT is detected calorimetrically after reaction with 5,5'-dithiobis-(2-nitrobenzoic acid) (DTNB), producing 5-mercapto-2-nitrobenzoic acid. The rate of disappearance of DTT is proportional to the oxidant activity. The assay uses 1,8-

phenanthraquinone as a positive control and methanol extracts of blank filters as a negative control.

We adapted the procedure of Li et al. [107] for use with a microplate reader to improve sample throughput, sensitivity, and precision. PM samples on PTFE filters were extracted by sonication in methanol (7 mL) for 60 minutes. Following sonication, the filters were removed from the extracts and discarded. Particle-containing and particle-free extracts were prepared for DTT analysis as follows: The samples were well mixed, and 150 µL aliquots, including solvent and suspended particles, were removed for analysis. The remaining portion of each extract was concentrated to 2 mL under a flow of nitrogen at 50°C in a Turbovap evaporative concentrator, vortexed, a second 150 µL aliquot was removed for possible analysis if the unconcentrated extract showed low activity. Finally, to prepare a particle-free portion of the extract, the remaining 1.85 mL of extract was filtered through 0.2 µm PTFE syringe filters into new Turbovap tubes. The filtered extracts were reduced to dryness and reconstituted in 150 µL of methanol. After vortexing, water and phosphate buffer were also added to the samples. To measure DTT reactivity, the extracts were then incubated in the presence of DTT in a 96-well plate. At designated time points (0, 10, 20, 30, 40, 50 minutes), aliquots of the reaction mixture were withdrawn and added to microplate wells containing tris HCl in 20 mM EDTA and DTNB (5,5'-dithiobis-(2-nitrobenzoic acid)). Absorption at 412 nm was recorded. The rate of DTT consumption is calculated from a plot of absorbance vs. time, and this value is corrected for atmospheric oxidation of DTT calculated from a blank filter extract time series run with each microplate.

4.1.3 *Excitation Emission Matrix (EEM) Analysis*

The EEM spectra of PM extract samples were obtained using a spectrofluorometer (Aqualog-880-C, HORIBA Instruments Inc. Edison, NJ, USA). For EEM spectroscopy, ~ 3 ml of PM extract was transferred to a 1 cm × 1 cm quartz cuvette (Item # CV10Q3500FS, Thorlabs Inc., Newton, New Jersey) loaded to the spectrofluorometer. The spectra were recorded in the range of excitation wavelength λ_{ex} = 200 - 600 nm with a 2 nm resolution. For each excitation wavelength, the instrument records emissions using a Charge Couple Device (CCD) array in the range of λ_{em} = 246 - 826 nm with a 0.58 nm resolution. The spectra were normalized to Raman units (R.U.).[95] Daily solvent blanks were recorded and used for blank subtraction to minimize the effect of Rayleigh and Raman scattering. To further reduce the effects of Rayleigh scattering, EEM values within 10 nm of the first and second-order Rayleigh scattering bands were excised, followed by replacing the values using 2-dimensional interpolation [153]. The processed EEMs were then passed through a Gaussian filter (sigma=2), and negative values were removed numerically in Python 3.6.0 to smooth the data (see Figure 4.2)[112].

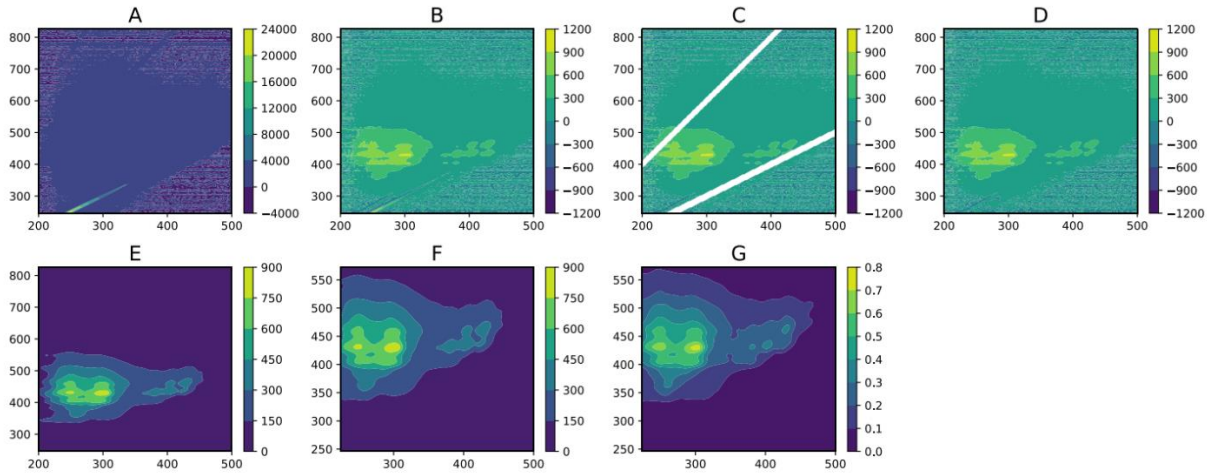

Figure 4.2. EEM of wood smoke extract showing data processing steps: Starting with the raw data (a), the solvent blank is subtracted (b), then values are excised for scatter removal (c), the excised values are interpolated (d), negative values are replaced with zero, and 2D-Gaussian smoothing is applied (e), the EEM is cropped (f) and normalized to Raman units (g).

4.1.4 *EEM Principal Component Regression (PCR) Analysis*

We used PCR analysis of the EEM spectra to evaluate the correlation between the EEM spectra and the DTT consumption rates. PCR is a two-step process in which predictors are transformed into a lower-dimensional representation by principal component analysis (PCA), and linear regression is performed on a chosen number of the principal components (PCs) and DTT consumption rates from the ROS analysis. 18 EEM spectra were split into 15 training spectra and 3 test spectra. In the case of the EEM data in this work, there are ~22,000 fluorescent values (predictors) in each data matrix. Linear regression could be performed using all values in the EEM independently but would result in overfitting. Instead, linear regression is performed on the PC representation of the data. The number of PCs used is smaller than the number of original predictors and is selected to capture nearly all the variance in the data, give the best possible model fit, and avoid overfitting.

In the first step of PCR, each EEM 2D matrix (1000 × 201) was unfolded into a 1D row vector (1 × 20100). 15 EEM row vectors of the training samples were stacked to create a training data matrix C (15 × 201000). The data matrix C was reduced with principal component analysis (PCA) using the scikit-learn library in Python 3.6.0. The number of PCs (d) required to represent the data in the data matrix C was varied from 1 to 15. The data matrix C can be represented as the matrix product of s and v and a residual matrix E, shown in

$$\boldsymbol{C = sv + E} \qquad \textbf{(4.1)}$$

where s (15 × d) is the scores matrix and v (d × 201000) is the loading matrix having d PC vectors. The scores matrix s is a reduced form of data matrix C; the operation reduces the number of data points required to represent each EEM from 20100 to d. The value of d is chosen to minimize the number of PCs that account for the maximum variance in the EEM dataset.

For the second step of PCR, the scores matrix s (15 × d) is used to fit linear models for estimating DTT consumption rates. We used the ordinary least squares method in the scikit-learn library in Python 3.6.0 to perform multiple linear regression (MLR) to fit two linear models between the EEM scores matrix and the DTT consumption rates for filtered samples unfiltered samples, respectively. The mean squared error (MSE), representing the error in correlation for each model, was calculated using the "leave one out cross-validation" (LOOCV) method.[98]

The models for estimating ROS concentrations trained on the smoke samples were tested using three random samples from the 18 samples. The EEM row vectors of the test samples were stacked to create a test data matrix C_{test} (3 × 201000), where 3 is the total number of test samples. The test data matrix C_{test} was reduced along the PCs obtained for the training samples to obtain a test scores matrix (3 × d). The coefficient of determination (R^2) for both models are reported.

4.2 Results and Discussion

4.2.1 *EEM Analysis*

PM extracts from natural-draft cookstove smoke, forced-draft cookstove smoke, and wildfire smoke show unique EEM spectra, as shown in Figure 4.3. Natural-draft cookstove smoke has spectra consisting of four peaks in the region from 400 – 475 nm emission and 225 – 275 nm excitation. Some fluorescence can also be observed in the region from 400 – 475 nm

emission and 350 – 450 nm excitation. Forced-draft cookstove smoke has significantly different spectra consisting of two peaks at ~350 nm emission wavelength from 350 – 450 nm excitation. The indoor and outdoor wildfire smoke spectra are similar, with a single primary peak located from 350 – 400 nm emission with some fluorescence surrounding the peak. Natural-draft cookstove smoke shows fluorescence over the broadest region and generally at higher emission wavelengths than forced-draft cookstove smoke and wildfire smoke. The spectra from the different sources have overlapping regions, so there can be some difficulty in identifying individual sources from mixed samples.

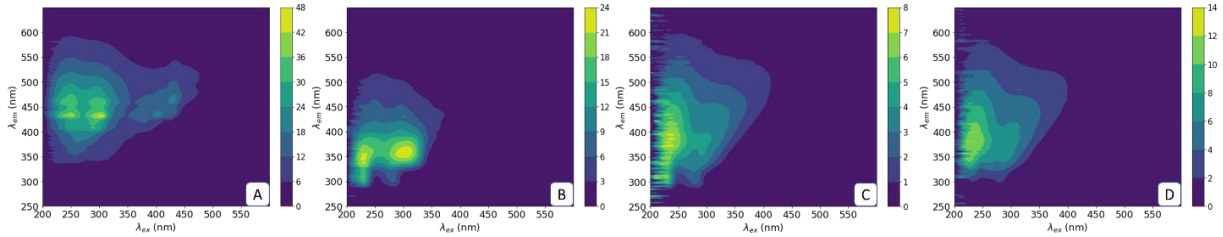

Figure 4.3. EEM spectra of four types of smoke: (a) natural-draft cookstove smoke, (b) forced-draft cookstove smoke, (c) 2020 Washington wildfire smoke collected indoors, (d) 2020 Washington wildfire smoke collected outdoors. The EEM spectra are from the extract in methanol. The spectra were normalized to Raman units (R.U.).

We also compared the spectra from filtered and unfiltered samples to see how insoluble material affects EEM spectra. Figure 4.4 shows the EEM spectrum of a filtered natural-draft cookstove smoke sample (A) and the spectrum of an unfiltered sample. The spectra have the primary peaks at exact locations. The peak fluorescence intensity of the unfiltered extract is three times higher than the filtered extract from the same sample. No significant difference in fluorescence contour can be observed from these two spectra.

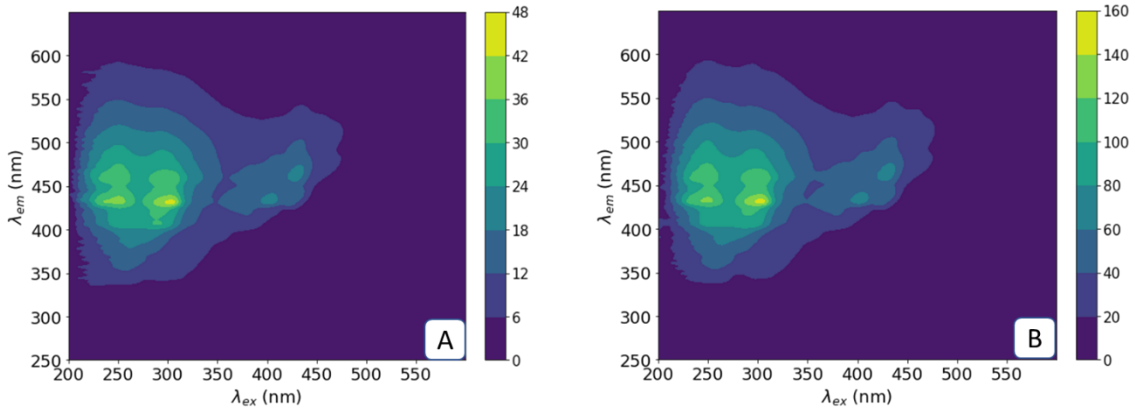

Figure 4.4. EEM spectra of natural-draft cookstove smoke from (a) a filtered extract, (b) an unfiltered extract. The EEM spectra are from the extract in methanol. The spectra were normalized to Raman units (R.U.).

4.2.2 *ROS Analysis*

We measured the oxidative potential of both filtered samples and unfiltered samples using DTT assay. Sample mass and DTT consumption rate for the smoke samples are summarized in Table 4.1. To evaluate the correlation between DTT consumption rate and sample mass, The DTT consumption rates of both filtered and unfiltered extracts are plotted against the sample mass in Figure 4.5. DTT consumption rate for the unfiltered natural-draft cookstove smoke samples is higher than the filtered samples. A filtered extract shows a similar DTT consumption rate as an unfiltered extract for the forced-draft cookstove smoke and the wildfire smoke. Note that one indoor wildfire smoke sample outlier was excluded for the following

analysis due to the mislabeled mass. For the normal samples, we did not observe a strong correlation between DTT consumption and sample mass.

Table 4.1. Summary of sample mass and DTT consumption rate for the smoke samples.

Sample Name	Sample Mass (mg)	DTT Consumption (ng/min/ug)	
		Unfiltered	Filtered
Cookstove Smoke	0.11	1.8	2.12
Cookstove Smoke	0.135	1.64	1.73
Cookstove Smoke	0.151	2.01	1.21
Cookstove Smoke	0.118	2.8	1.88
Cookstove Smoke	0.146	2.1	1.78
Cookstove Smoke	0.157	0.94	0.9
Indoor Wildfire Smoke	0.325	4.76	5.04
Indoor Wildfire Smoke	0.234	4.75	5.83
Indoor Wildfire Smoke (outlier)	0.297	12.03	9.93
Outdoor Wildfire Smoke	0.371	4.88	4.75
Outdoor Wildfire Smoke	0.392	4.65	4.32
Outdoor Wildfire Smoke	0.425	4.74	4.4
Forced-draft Cookstove Smoke	0.114	7.84	5.58
Forced-draft Cookstove Smoke	0.122	7.56	5.87
Forced-draft Cookstove Smoke	0.132	6.35	4.71
Forced-draft Cookstove Smoke	0.132	7.36	5.4
Forced-draft Cookstove Smoke	0.126	6.85	5.58
Forced-draft Cookstove Smoke	0.125	8.42	5.43

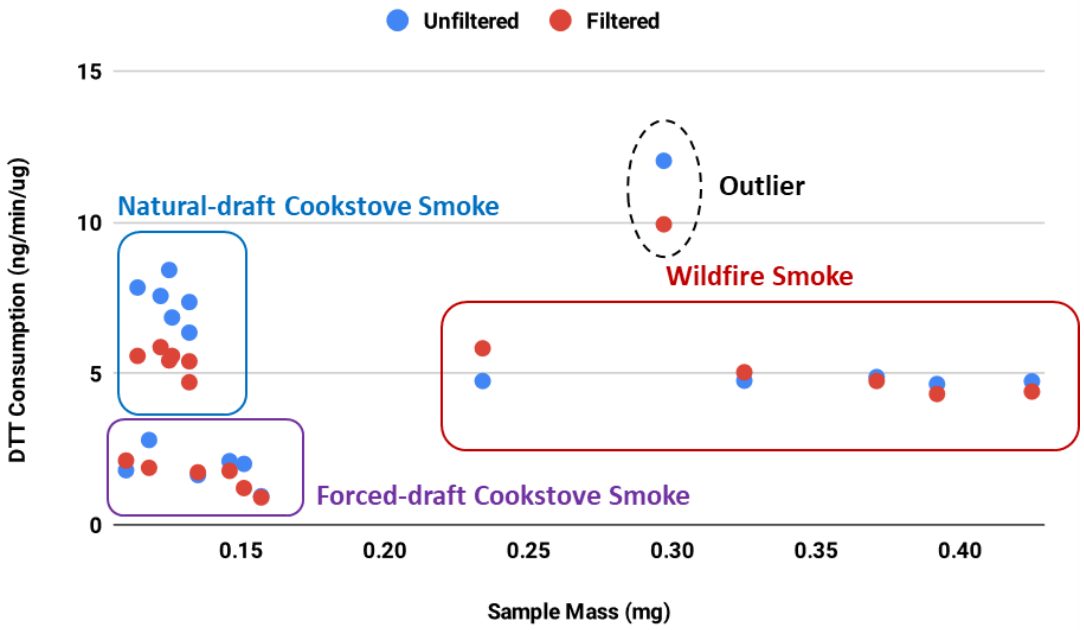

Figure 4.5. The DTT consumption rate for the filtered and unfiltered extracts of the smoke samples vs. sample mass. Natural-draft cookstove smoke samples are enclosed in the blue box; Forced-draft cookstove smoke samples are enclosed in the purple box; 2020 Washington wildfire smoke samples are enclosed in the red box with one outlier outside.

4.2.3 *EEM Integrated Fluorescence Intensity and ROS*

To investigate the correlation between EEM spectra and ROS, we first plotted the integrated fluorescent intensity of the EEM data against the DTT consumption rate for each sample. Integrated fluorescence was calculated by adding all the fluorescence intensity values in a 2D EEM matrix. Figure 4.6 shows the integrated fluorescent intensity measurement vs. DTT consumption rate for the filtered and unfiltered smoke samples. Samples from the same group cluster with the natural-draft cookstove smoke samples have higher integrated fluorescence intensity than others. We observed no strong correlation between integrated fluorescence intensity and DTT consumption rate for the filtered and unfiltered smoke samples.

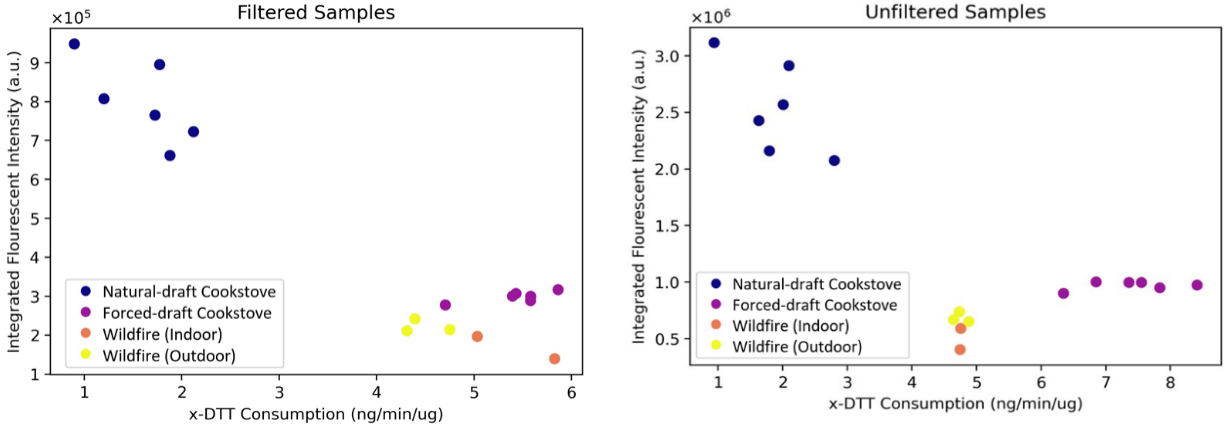

Figure 4.6. Integrated fluorescent intensity vs. DTT consumption rate for filtered and unfiltered smoke samples.

4.2.4 *PCR Analysis*

The PCR analysis was performed on the dataset to evaluate the correlation between the 2D EEM spectra and DTT consumption rates. PCA was performed on the 15 training spectra to generate the PCs. The first three PCs for the filtered and unfiltered smoke samples are shown in Figure 4.7. The first three PCs account for 99% of the variance (see Figure 4.8) in the dataset

showing that although the original data contain over twenty-thousand fluorescent values, the spectra can be effectively represented in a lower-dimensional space.

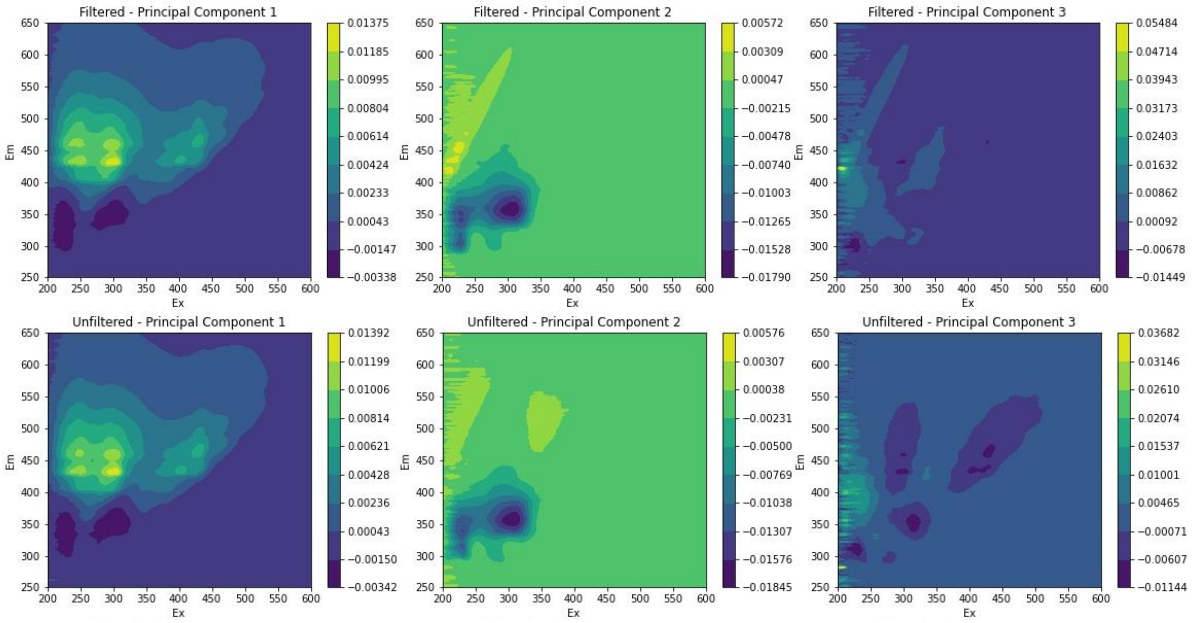

Figure 4.7. The first three principal components of the 15 training EEM spectra for filtered (top) and unfiltered (bottom) smoke samples. These three PCs shown here account for 99% of the variance in the dataset.

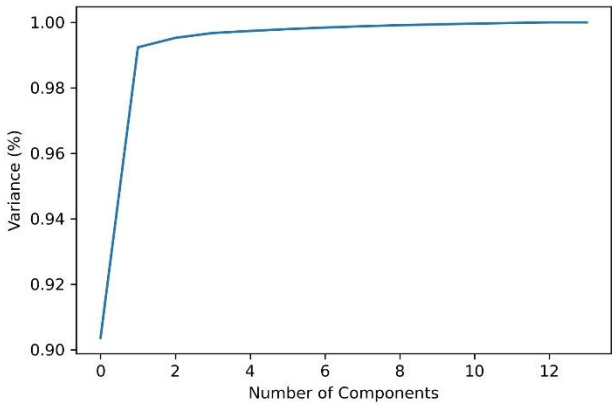

Figure 4.8. Contribution of PC to the variance of the EEM dataset.

We performed PCR using from one to fifteen PCs. The ordinary least squares method was used in the scikit-learn library in Python 3.6.0 to perform multiple linear regression to fit two linear models between the EEM scores matrix and the DTT consumption rates for filtered

and unfiltered samples, respectively. Figure 4.9 plots the R^2 values for filtered and unfiltered samples vs. the number of PCs used for PCR. As the number of PCs increases from one to fifteen, the fit to the training data continually improves where the fit to the filtered sample data is always better than the fit to the unfiltered sample data. Based on the variance in the EEM data for d=1-15 PCs and the R^2 values, $d = 5$ for unfiltered samples and $d = 4$ for filtered samples were chosen for fitting the linear models for DTT consumption rate, as these PCs accounted for more than 99% variance. The PCR model shows a good correlation between EEM PCs and DTT consumption rate for the unfiltered samples with training and test R^2 values of 0.98 and 0.76, respectively. DTT consumption rate can also be successfully predicted for filtered samples with (train, test) R^2 values of (0.95, 0.97).

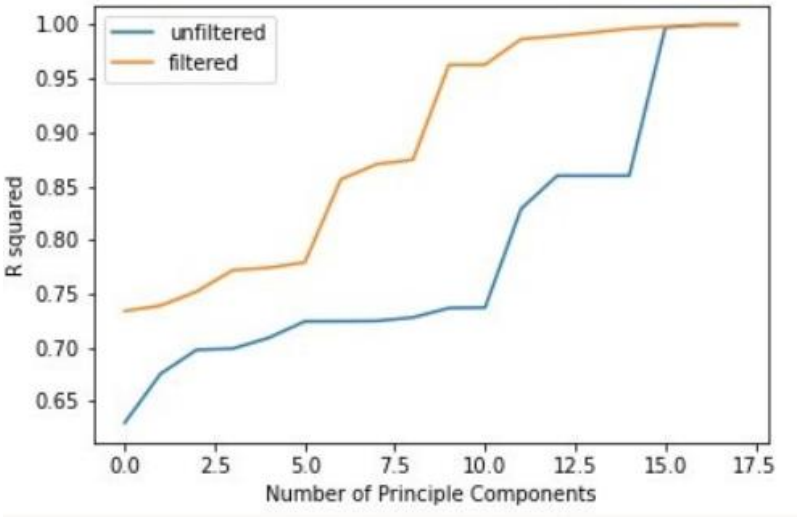

Figure 4.9. PCR R^2 vs. number of PCs used in PCR for DTT consumption rate. As the number of PCs is increased from one to fifteen, the fit to the training data continually improves. The fit to the filtered sample data is always better than the fit to the unfiltered sample data.

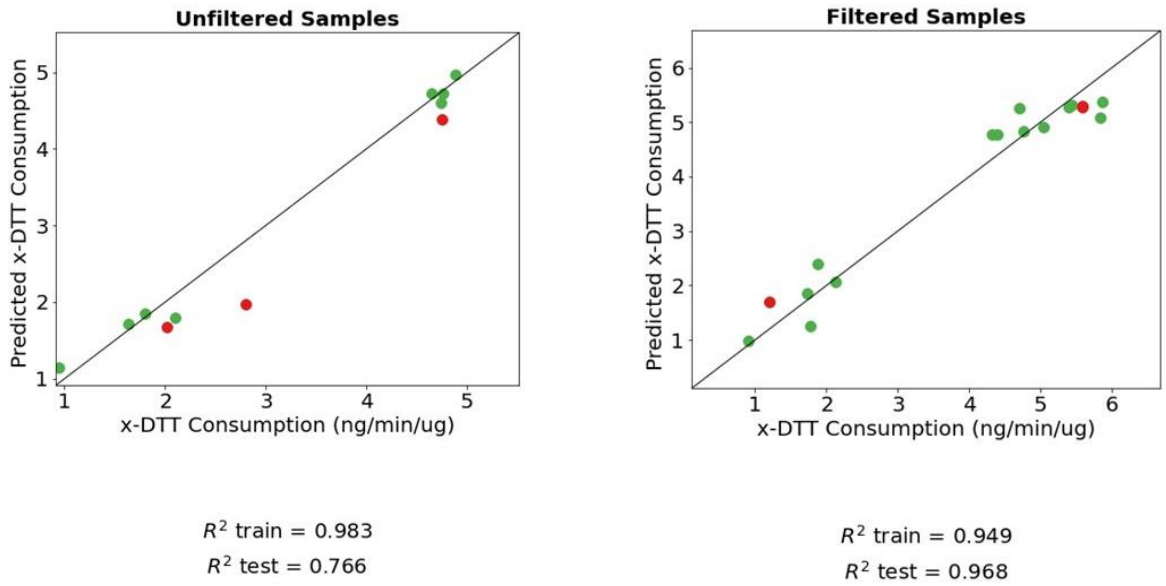

Figure 4.10. Parity plots showing results of PCR with 5 PCs for unfiltered samples and 4 PCs for filtered samples. Green points show training samples, and test samples are shown in roe points. The PCR model shows a good correlation between EEM PCs and DTT consumption rate for the unfiltered samples with training and test R^2 values of 0.98 and 0.76, respectively. DTT consumption rate is also successfully predicted for filtered samples with (train, test) R^2 values of (0.95, 0.97).

4.3 CONCLUSIONS

In this study, we investigated the correlation between EEM signature and ROS measurements. PM collected from the cookstove and wildfire smoke were analyzed by EEM and the DTT assay. Using principal component regression (PCR) analysis of the EEM spectra, we drew the correlation between the EEM spectra and the DTT measurements. The results suggest that the PCA of EEM spectra can be correlated to DTT consumption and that EEM can be an alternative method to evaluate the ROS level in combustion-generated aerosols.

Chapter 5. THESIS CONCLUSIONS AND FUTURE WORK

5.1 AEROSOL MONITORING USING SENSOR NETWORK

This dissertation evaluated the PMS sensors and reported the calibration algorithm for both number concentration and mass concentration. We found that the number concentrations can be corrected using a simple linear model, and mass concentrations can be better corrected using a polynomial model. We used particles in a relatively narrow range of CRIs, morphologies, and densities, and our RH was restricted to 20% - 80%. If the particle properties and environmental conditions of interest are significantly different from the tested scenarios, one may need to consider these effects. Despite these limitations, this study has significant implications, especially for using these sensors in high concentration environments, including indoor air quality monitoring, occupational/industrial exposure assessments, wildfire smoke, or near-source monitoring scenarios. Since the test aerosols used in this study are applicable for several occupational health scenarios, a better exposure assessment could be achieved. In applying near-source and indoor air quality monitoring where field calibration might be challenging, these low-cost sensors, along with the calibration algorithms developed within a higher concentration range applied, could serve as a substitute for the traditional gravimetric instruments to provide valuable assessment of air quality.

We also demonstrated the application of an IoT-enabled low-cost sensor network for air quality monitoring during the wildfire. When used with corrections, the outdoor sensor data was comparable to the nearest regional monitor. The significance of this finding is that the calibration model allows for obtaining real-world data using low-cost sensors and developing a high-density sensor network for monitoring outdoor PM levels and indoor and outdoor environments. The

personal monitoring results highlighted the influence of personal activities and microenvironments on an individual's exposure to $PM_{2.5}$. The hyperlocal activities significantly influenced personal exposure to PM. Although this study is based on a relatively small sample size, it demonstrated that personal action, such as staying indoors and using HEPA air cleaner, can potentially reduce personal exposure to wildfire smoke. Future studies with a larger sample size and a collection of time-activity information are warranted to investigate the source of $PM_{2.5}$ exposure and estimate the consequent health effects.

While current off-the-shelf sensors provide an estimation of PM concentration information, better particle sensors that can measure particle size are needed to enrich the data the sensor network collects to get more accurate exposure profiles and accurate environment information.

5.2 Aerosol Sampling Cartridge and Device

We designed and evaluated a novel μ-well aerosol collector combined with an AF inlet to collect fine PM fraction. The AF μ-well collector can collect highly concentrated particle samples in a 1 mm in diameter collection site. Particles stay in the well because their bounce is redirected toward the center of the well, increasing the sample collection density. The collection efficiency of the μ-well collector shows a minor dependency on the particle bounce when compared to the flat impactor. The roughness of the μ-well surface may contribute to the particle collection by modifying the particle bounce characteristics.

Further studies are needed to quantify the effect of surface roughness on particle collection. The sampling efficiency of the μ-well impactor is tested under relatively low particle loading scenarios. Therefore, additional work may be required to estimate collector overloading/fouling characteristics.

The performance of a low-cost µ-well aerosol cartridge is evaluated for collection and analysis of single-organism B. Subtilis spores. The design of the device is based on practical considerations for sample analysis; the inlet dimensions are compatible with the pipette sample elution and integration with personal exposure monitors. The cartridge collects highly concentrated particle samples in a 1 mm diameter spot. The sample is retained in the well because the particle bounce is redirected toward the center of the well, increasing the sample collection density. Collection efficiency is consistent for each flow condition. Sample recovery for the pipette elution is more than 75%. The elution volume used to recover the collected sample from the cartridge is in the range of 10-20 µl, which provides a high preconcentration of the aerosol sample for liquid assays; based on the cartridge geometry, the volume can be further reduced if the procedure is automated or microfluidic analysis is desired.

5.3 EEM FOR ESTIMATION OF ROS ON COMBUSTION GENERATED AEROSOLS

We investigated the correlation between EEM spectra and ROS measurements. PM collected from cookstoves and wildfire smoke was analyzed by EEM and the DTT assay. Using PCR analysis of the EEM spectra, we drew the correlation between the EEM spectra and the DTT measurements. The results suggest that the principal components of the EEM spectra correlate well with the DTT consumption rate for ROS, suggesting that EEM can be an alternative method to evaluate the ROS level on combustion-generated aerosols. This study's sample size is relatively small. The preliminary results indicate a low-cost, short turnaround method for ROS estimation. Future studies with larger sample sizes on different types of combustion-generated aerosols are needed to confirm the results.

Chapter 6. APPENDIX

6.1 SUMMARY OF OTHER MODELS FITTED IN THE SENSOR CALIBRATION STUDY

Table 6.1. Summary of the R^2, Bayesian information criterion (BIC), and the normalized mean absolute error (NMAE) of the calibration models for number concentration.

Indices	Equation	Regression [a]	R^2	BIC	NMAE
Full concentration range (APS total number concentration between 0 – 1000 #/ cm^3) (n = 4,134)					
>0.3 µm	Linear	y = 5.93 x	0.99	78723	2.20%
	Linear + CRI	y = 6.02 x - 516.26 CRI	0.99	78603	2.07%
	Linear + RH	y = 5.99 x - 13.72 RH	0.99	78684	2.12%
	Linear + density	y = 6.00 x - 244.83 density	0.99	78659	2.09%
	Linear + CRI + density	**y = 6.06 x - 7924 CRI + 4709 density**	**0.99**	**78134**	**2.02%**
	Linear + CRI + RH	y = 6.00 x - 1090 CRI + 28.23 RH	0.99	78567	2.06%
>0.5 µm	Linear	y = 14.17 x	0.98	79716	2.92%
	Linear + CRI	y = 14.52 x - 605.95 CRI	0.98	79584	2.83%
	Linear + RH	y = 14.39 x - 14.59 RH	0.98	79682	2.85%
	Linear + density	y = 14.46 x - 322.64 density	0.98	79618	2.83%
	Linear + CRI + density	**y = 14.59 x - 5054 CRI + 2828 density**	**0.98**	**79462**	**2.81%**
	Linear + CRI + RH	y = 14.40 x - 1434 CRI + 40.68 RH	0.98	79518	2.78%
>1 µm	Linear	y = 14.85 x	0.96	76002	2.88%
	Linear + CRI	y = 15.15 x - 243.6 CRI	0.97	75950	2.91%
	Linear + RH	y = 14.99 x - 4.28 RH	0.96	76000	2.89%
	Linear + density	y = 15.08 x - 121.37 density	0.96	75973	2.90%
	Linear + CRI + density	**y = 15.23 x - 3476 CRI + 2064 density**	**0.97**	**75789**	**2.87%**
	Linear + CRI + RH	y = 14.98 x - 784.93 CRI + 26.40 RH	0.97	75884	2.89%
>2.5 µm	Linear	y = 2.2 x	0.66	62906	3.87%
	Linear + CRI	y = 2.48 x - 86.58 CRI	0.68	62717	3.95%
	Linear + RH	y = 2.43 x - 2.79 RH	0.67	62808	3.84%
	Linear + density	y = 2.46 x - 52.33 density	0.67	62737	3.93%
	Linear + CRI + density	y = 2.48 x - 343.19 CRI + 164.55 density	0.68	62699	3.93%
	Linear + CRI + RH	**y = 2.42 x - 156.71 CRI + 3.38 RH**	**0.68**	**62695**	**3.95%**
>5 µm	Linear	y = 0.11 x	0.31	38958	2.71%
	Linear + CRI	y = 0.14 x - 3.72 CRI	0.33	38843	2.83%
	Linear + RH	y = 0.14 x - 0.16 RH	0.32	38849	2.78%
	Linear + density	y = 0.14 x - 2.27 density	0.32	38853	2.82%
	Linear + CRI + density	**y = 0.13 x - 12.76 CRI + 5.81 density**	**0.33**	**38841**	**2.82%**
	Linear + CRI + RH	y = 0.14 x - 2.41 CRI - 0.06 RH	0.33	38848	2.83%
>10 µm	Linear	y = 0.11 x	0.70	8117	3.66%
	Linear + CRI	y = 0.14 x - 3.72 CRI	0.71	7997	3.69%
	Linear + RH	y = 0.14 x - 0.16 RH	0.71	7998	3.65%
	Linear + density	y = 0.14 x - 2.27 density	0.71	8022	3.66%
	Linear + CRI + density	**y = 0.13 x - 12.76 CRI + 5.81 density**	**0.72**	**7918**	**3.67%**
	Linear + CRI + RH	y = 0.14 x - 2.41 CRI - 0.06 RH	0.71	8000	3.68%
Lower concentration range (APS total number concentration < 100 #/ cm^3) (n = 1,838)					
>0.3 µm	Linear	y = 4.84 x	0.97	30263	7.96%
	Linear + CRI	y = 4.95 x - 86.88 CRI	0.97	30263	8.02%
	Linear + RH	y = 4.80 x - 1.08 RH	0.97	30270	7.94%
	Linear + density	y = 4.92 x - 43.29 Density	0.97	30265	8.01%
	Linear + CRI + density	y = 4.98 x - 723.33 CRI + 396.15 Density	0.97	30259	7.98%
	Linear + CRI + RH	**y = 4.94 x - 358.12 CRI + 13.68 RH**	**0.97**	**30235**	**7.94%**

>0.5 µm	Linear	y = 10.84 x	0.93	30285	10.39%
	Linear + CRI	y = 10.89 x - 9.97 CRI	0.93	30293	10.41%
	Linear + RH	y = 10.38 x + 5.12 RH	0.93	30276	10.21%
	Linear + density	y = 10.89 x - 5.98 Density	0.93	30293	10.41%
	Linear + CRI + density	y = 10.89 x - 15.80 CRI + 3.63 density	0.93	30300	10.41%
	Linear + CRI + RH	**y = 10.83 x - 385.61 CRI + 18.91 RH**	**0.94**	**30234**	**10.23%**
>1 µm	Linear	y = 12.50 x	0.92	26963	8.50%
	Linear + CRI	y = 11.21 x + 105.13 CRI	0.93	26844	7.99%
	Linear + RH	y = 10.88 x + 6.37 RH	0.93	26734	7.68%
	Linear + density	y = 11.17 x + 69.72 density	0.93	26828	7.97%
	Linear + CRI + density	y = 11.33 x - 361.34 CRI + 294.27 density	0.93	26812	7.94%
	Linear + CRI + RH	**y = 11.10 x - 105.04 CRI + 10.59 RH**	**0.93**	**26713**	**7.57%**
>2.5 µm	Linear	y = 0.51 x	0.60	14298	7.73%
	Linear + CRI	y = 0.46 x + 1.20 CRI	0.60	14284	7.72%
	Linear + RH	y = 0.41 x + 0.13 RH	0.62	14192	7.76%
	Linear + density	y = 0.46 x + 0.80 density	0.60	14282	7.72%
	Linear + CRI + density	y = 0.46 x - 4.61 CRI + 3.71 density	0.60	14286	7.68%
	Linear + CRI + RH	**y = 0.45 x - 8.38 CRI + 0.48 RH**	**0.66**	**14018**	**7.22%**
>5 µm	Linear	y = 0.01 x	0.35	-2612	11.52%
	Linear + CRI	y = 0.003 x + 0.04 CRI	0.43	-2845	12.04%
	Linear + RH	**y = 0.004 x + 0.002 RH**	**0.44**	**-2876**	**11.89%**
	Linear + density	y = 0.003 x + 0.03 density	0.43	-2856	12.01%
	Linear + CRI + density	y - 0.003 x - 0.06 CRI + 0.06 density	0.44	-2855	11.95%
	Linear + CRI + RH	y = 0.003 x + 0.007 CRI + 0.002 RH	0.44	-2869	11.91%
>10 µm	Linear	y = 0.004 x	0.19	-5846	15.16%
	Linear + CRI	y = 0.002 x + 0.009 CRI	0.22	-5922	17.97%
	Linear + RH	**y = 0.002 x + 0.0004 RH**	**0.22**	**-5926**	**17.74%**
	Linear + density	y = 0.002 x + 0.006 density	0.22	-5922	17.95%
	Linear + CRI + density	y = 0.002 x + 0.004 CRI + 0.003 density	0.22	-5915	17.97%
	Linear + CRI + RH	y = 0.002 x + 0.003 CRI + 0.0003 RH	0.22	-5920	17.91%

[a] y: APS measurement; x: PMS measurement. The models emboldened for each size bin were the optimal model selected according to the BIC.
Definition of abbreviations: n = number of datapoints; CRI = complex index of refraction; RH = relative humidity; BIC = Bayesian information criteria; NMAE = normalized mean absolute error.

Table 6.2. Summary of the calibration models for mass concentration, the R^2, Bayesian information criterion (BIC), and the normalized mean absolute error (NMAE).

Indices	Equation	Regression [a]	R^2	BIC [b]	NMAE
Full concentration range (APS total number concentration between 0 – 1000 #/ cm^3) (n = 4,134)					
PM_1	Linear	y = 1.06 x	0.96	25852	3.11%
	Polynomial	y = 0.76 x + 0.007 x^2	0.97	24480	2.41%
	Linear + CRI	y = 1.16 x - 2.12 CRI	0.97	25137	2.99%
	Polynomial + CRI	y = 0.82 x + 0.006 x^2 - 0.58 CRI	0.97	24446	2.48%
	Linear + RH	y = 1.15 x - 0.08 RH	0.97	25333	3.03%
	Polynomial + RH	y = 0.79 x + 0.01 x^2 - 0.02 RH	0.97	24471	2.46%
	Linear + density	y = 1.16 x - 1.51 density	0.97	24906	3.00%
	Polynomial + density	y = 0.87 x + 0.01 x^2 - 0.65 density	0.97	24351	2.54%
	Linear + CRI + density	y = 1.13 x + 13.88 CRI - 10.13 density	0.97	24181	2.84%
	Polynomial + CRI + density	**y = 0.83 x + 0.01 x^2 + 14.44 CRI - 9.58 density**	**0.98**	**23432**	**2.33%**

	Linear + CRI + RH	y = 1.15 x - 2.14 CRI + 0.001 RH	0.97	25143	2.99%
	Polynomial + CRI + RH	y = 0.82 x + 0.006 x^2 - 0.78 CRI + 0.01 RH	0.97	24451	2.47%
$PM_{2.5}$	Linear	y = 2.29 x	0.94	42435	4.53%
	Polynomial	y = 1.55 x + 0.006 x^2	0.96	41341	3.41%
	Linear + CRI	y = 2.54 x - 16.04 CRI	0.95	41613	4.07%
	Polynomial + CRI	y = 1.86 x + 0.004 x^2 - 7.36 CRI	0.96	41227	3.47%
	Linear + RH	y = 2.50 x - 0.53 RH	0.95	41983	4.12%
	Polynomial + RH	y = 1.64 x + 0.005 x^2 - 0.1 RH	0.96	41337	3.41%
	Linear + density	y = 2.53 x - 10.36 density	0.95	41568	4.05%
	Polynomial + density	y = 1.88 x + 0.004 x^2 - 5.11 density	0.96	41199	3.48%
	Linear + CRI + density	y = 2.52 x + 13.55 CRI - 18.82 density	0.95	41565	4.04%
	Polynomial + CRI + density	y = 1.85 x + 0.004 x^2 + 22.74 CRI - 19.13 density	0.96	41172	3.44%
	Linear + CRI + RH	y = 2.51 x - 23.27 CRI + 0.36 RH	0.95	41565	4.07%
	Polynomial + CRI + RH	**y = 1.80 x + 0.004 x^2 - 15.55 CRI + 0.42 RH**	**0.96**	**41152**	**3.44%**
PM_{10}	Linear	y = 1.53 x	0.85	49963	3.56%
	Polynomial	y = 0.72 x - 0.003 x^2	0.88	48959	2.61%
	Linear + CRI	y = 1.72 x - 27.80 CRI	0.86	49555	3.31%
	Polynomial + CRI	y = 0.78 x + 0.003 x^2 - 3.13 CRI	0.88	48963	2.63%
	Linear + RH	y = 1.69 x - 0.96 RH	0.86	49716	3.33%
	Polynomial + RH	y = 0.66 x - 0.003 x^2 + 0.13 RH	0.88	48963	2.62%
	Linear + density	y = 1.71 x - 17.91 density	0.86	49541	3.32%
	Polynomial + density	y = 0.80 x - 0.003 x^2 - 2.9 density	0.88	48958	2.65%
	Linear + CRI + density	y = 1.71 x + 12.33 CRI - 25.67 density	0.86	49548	3.32%
	Polynomial + CRI + density	y = 0.75 x + 0.003 x^2 + 55.58 CRI - 37.27 density	0.88	48934	2.62%
	Linear + CRI + RH	y = 1.69 x - 39.14 CRI + 0.56 RH	0.87	49544	3.31%
	Polynomial + CRI + RH	**y = 0.73 x + 0.003 x^2 - 17.94 CRI + 0.75 RH**	**0.88**	**48931**	**2.61%**
Lower concentration (APS total number concentration < 100 #/ cm^3) (n = 1,838)					
PM_1	Linear	y = 0.72 x	0.90	6211	10.10%
	Polynomial	y = 0.91 x - 0.02 x^2	0.91	6053	9.23%
	Linear + CRI	y = 0.6 x + 0.50 CRI	0.91	6020	8.82%
	Polynomial + CRI	y = 0.71 x - 0.01 x^2 + 0.36 CRI	0.91	6017	8.82%
	Linear + RH	y = 0.60 x + 0.02 RH	0.92	5979	8.75%
	Polynomial + RH	y = 0.70 x - 0.001 x^2 + 0.02 RH	0.92	5971	8.68%
	Linear + density	y = 0.62 x + 0.26 density	0.91	6077	9.04%
	Polynomial + density	y = 0.82 x - 0.02 x^2 + 0.1 density	0.91	6052	9.06%
	Linear + CRI + density	y = 0.57 x + 4.80 CRI - 2.68 density	0.93	5746	8.16%
	Polynomial + CRI + density	**y = 0.80 x - 0.02 x^2 + 4.93 CRI - 2.95 density**	**0.93**	**5694**	**8.08%**
	Linear + CRI + RH	y = 0.60 x + 0.08 CRI + 0.02 RH	0.92	5989	8.73%
	Polynomial + CRI + RH	y = 0.72 x - 0.01 x_2 - 0.1 CRI + 0.02 RH	0.92	5987	8.69%
$PM_{2.5}$	Linear	y = 1.10 x	0.91	11170	9.14%

	Polynomial	$y = 1.34\ x - 0.01\ x^2$	0.91	11087	8.80%
	Linear + CRI	$y = 0.98\ x + 1.37\ CRI$	0.92	11061	8.48%
	Polynomial + CRI	$y = 1.09\ x - 0.004\ x^2 + 1.06\ CRI$	0.92	11064	8.49%
	Linear + RH	$y = 0.94\ x + 0.09\ RH$	0.92	10932	8.11%
	Polynomial + RH	$y = 0.92\ x + 0.001\ x^2 + 0.09\ RH$	0.92	10939	8.11%
	Linear + density	$y = 0.99\ x + 0.80\ density$	0.91	11076	8.55%
	Polynomial + density	$y = 1.14\ x - 0.01\ x^2 + 0.54\ density$	0.92	11074	8.58%
	Linear + CRI + density	$y = 0.97\ x + 6.51\ CRI - 3.23\ density$	0.92	11043	8.40%
	Polynomial + CRI + density	$y = 1.09\ x - 0.004\ x^2 + 6.28\ CRI - 3.31\ density$	0.92	11045	8.42%
	Linear + CRI + RH	$y = 0.97\ x - 1.87\ CRI + 0.16\ RH$	0.92	10890	8.01%
	Polynomial + CRI + RH	**$y = 1.14\ x - 0.006\ x^2 - 2.43\ CRI + 0.17\ RH$**	**0.92**	**10885**	**7.97%**
PM_{10}	Linear	$y = 0.63\ x$	0.89	11878	9.30%
	Polynomial	$y = 0.86\ x - 0.01\ x^2$	0.90	11686	8.53%
	Linear + CRI	$y = 0.55\ x + 1.92\ CRI$	0.90	11716	8.45%
	Polynomial + CRI	$y = 0.75\ x - 0.004\ x^2 + 0.88\ CRI$	0.90	11675	8.34%
	Linear + RH	$y = 0.52\ x + 0.12\ RH$	0.91	11566	8.10%
	Polynomial + RH	$y = 0.62\ x - 0.002\ x^2 + 0.1\ RH$	0.91	11556	7.99%
	Linear + density	$y = 0.55\ x + 1.12\ density$	0.90	11741	8.54%
	Polynomial + density	$y = 0.78\ x - 0.004\ x^2 + 0.38\ density$	0.90	11685	8.41%
	Linear + CRI + density	$y = 0.54\ x - 11.26\ CRI - 5.92\ density$	0.90	11662	8.26%
	Polynomial + CRI + density	$y = 0.72\ x - 0.003\ x^2 + 9.58\ CRI - 5.45\ density$	0.90	11631	8.16%
	Linear + CRI + RH	$y = 0.54\ x - 2.15\ CRI + 0.20\ RH$	0.91	11627	8.01%
	Polynomial + CRI + RH	**$y = 0.78\ x - 0.004\ x^2 - 3.57\ CRI + 0.21\ RH$**	**0.91**	**11461**	**7.75%**

[a] y: APS measurement; x: PMS measurement. The models emboldened for each size bin were the optimal model selected according to the BIC.
Definition of abbreviations: n = number of datapoints; CRI = complex index of refraction; RH = relative humidity; BIC = Bayesian information criteria; NMAE = normalized mean absolute error.

6.2 Time-series Plots of Indoor and Outdoor $PM_{2.5}$ Concentrations throughout the 2020 Wildfire Study

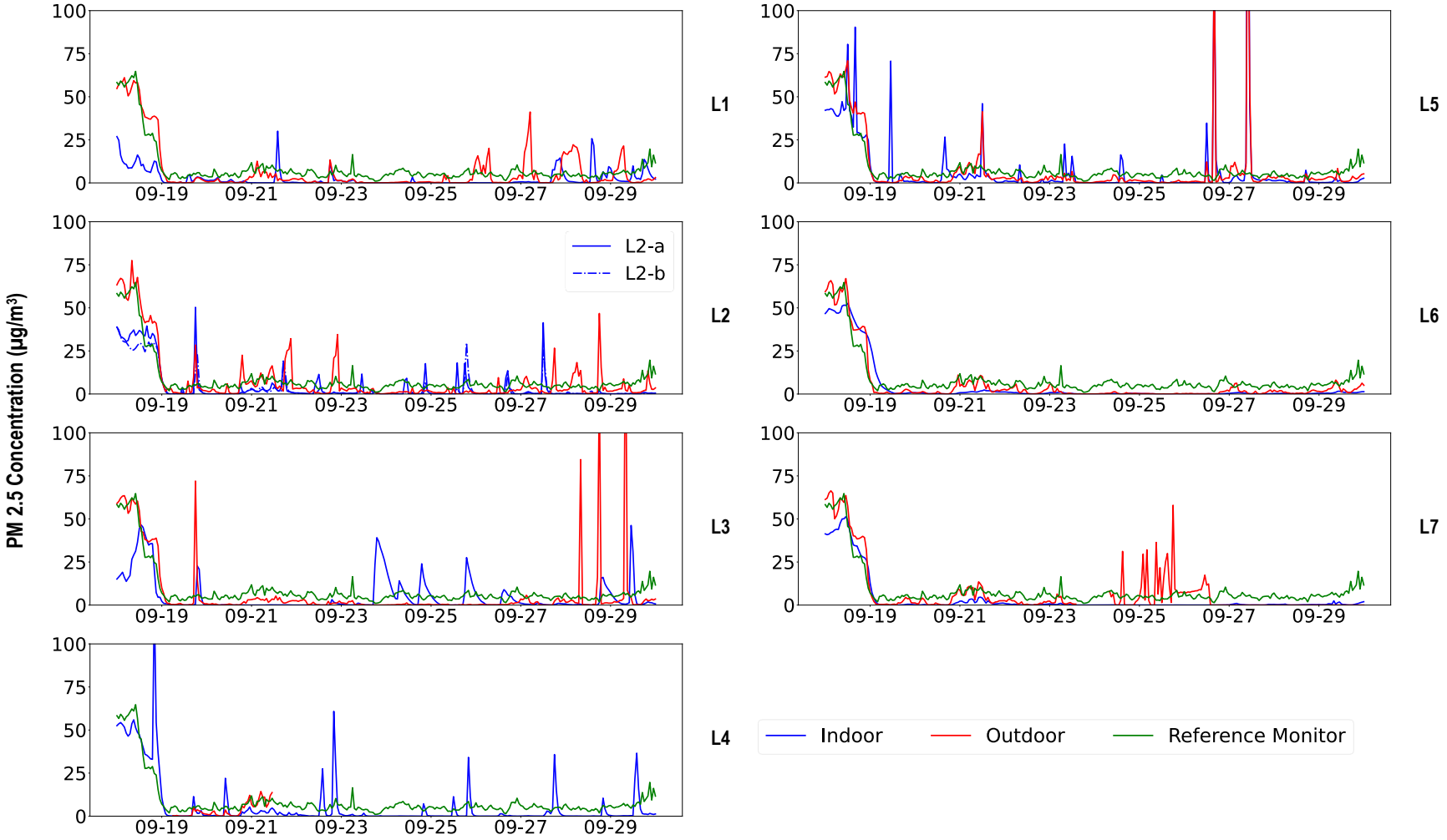

Figure 6.1. Time-series plots of indoor and outdoor $PM_{2.5}$ concentrations compared to the reference monitors for each sampling site during the wildfire. The blue and red lines illustrate the sensors' indoor and outdoor $PM_{2.5}$ concentrations measurements, and the green line illustrates the averaged $PM_{2.5}$ measurements from the nearby regional monitoring sites.

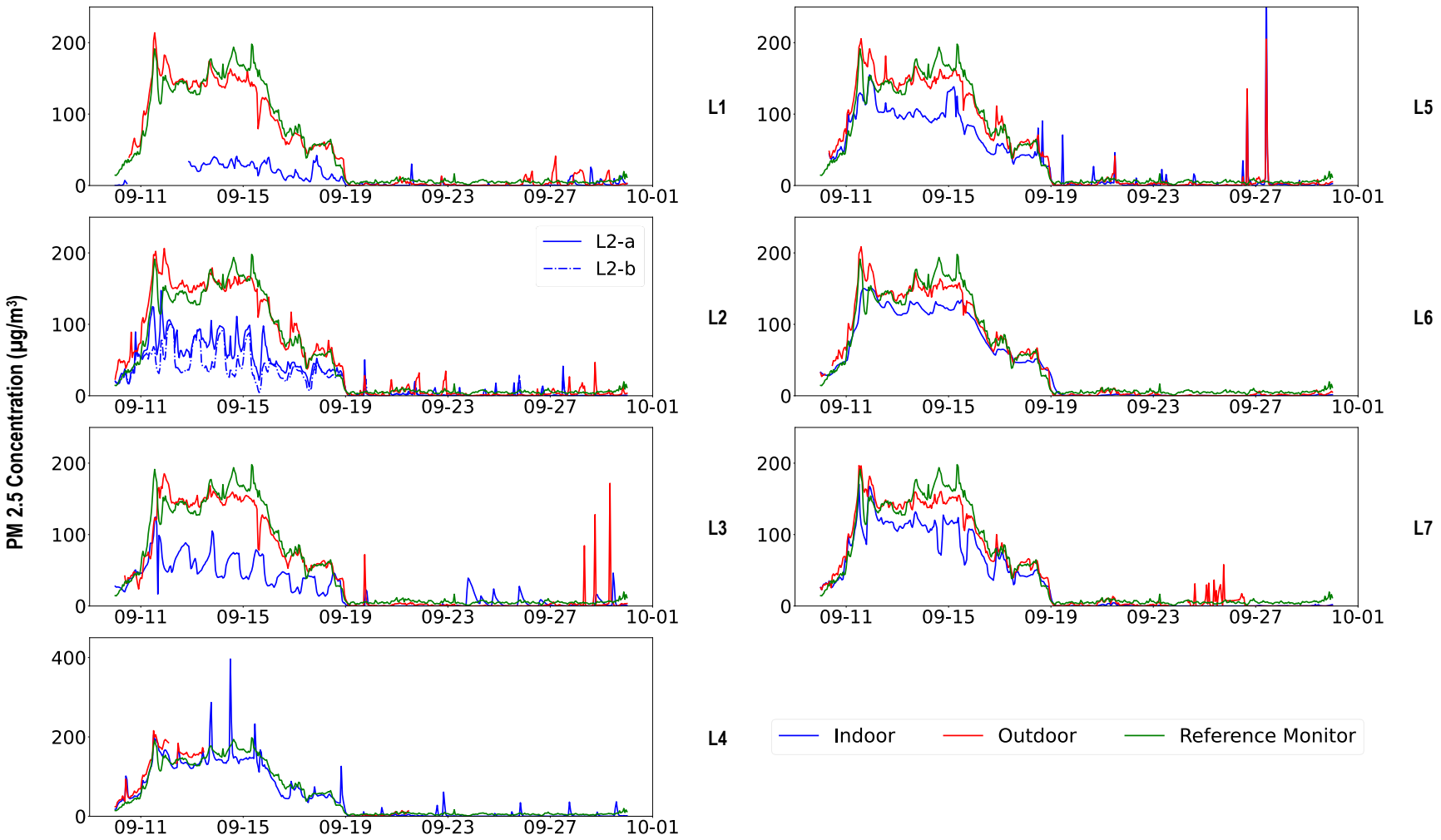

Figure 6.2. Time-series plots of indoor and outdoor $PM_{2.5}$ concentrations compared to the reference monitors for each sampling site during the wildfire. The blue and red lines illustrate the sensors' indoor and outdoor $PM_{2.5}$ concentrations measurements, and the green line illustrates the averaged $PM_{2.5}$ measurements from the nearby regional monitoring sites.

VITA

Jiayang (Joe) He is a Ph.D. candidate and a research scientist at the University of Washington Novosselov Research Group (NRG). His research focuses on developing low-cost personal exposure monitoring approaches for monitoring sampling and chemical analysis of particulate matter (PM). Understanding the exposure to PM at the individual level can help develop better strategies for air pollution protection. Joe's contribution in the aerosol monitoring field allowed his team to build a low-cost PM sensor network that can be used in large-scale wildfire smoke exposure monitoring and small-scale indoor infectious aerosol monitoring. His contribution in the aerosol sampling field leads to developing the micro-well cartridge that can capture fine PM and personal exposure monitors explicitly targeting $PM_{2.5,}$ which has been deployed in a large-scale epidemiological study. His contribution in the aerosol analysis field using the EEM technique can lead to a fast and low-cost way to detect Reactive Oxygen Species in combustion aerosols. His contributions enable researchers to better understand the adverse health effect associated with exposure to PM.

REFERENCES

[1] W. C. Hinds, *Aerosol technology : properties, behavior, and measurement of airborne particles*, 2nd ed. New York: Wiley, 1999, pp. xx, 483 pages.

[2] D. Krewski *et al.*, "Overview of the reanalysis of the Harvard Six Cities Study and American Cancer Society Study of Particulate Air Pollution and Mortality," (in eng), *Journal of toxicology and environmental health. Part A*, vol. 66, no. 16-19, pp. 1507-51, Aug 22-Oct 10 2003, doi: 10.1080/15287390306424.

[3] D. Krewski *et al.*, "Extended follow-up and spatial analysis of the American Cancer Society study linking particulate air pollution and mortality," (in eng), *Research report (Health Effects Institute)*, no. 140, pp. 5-114; discussion 115-36, May 2009.

[4] C. A. Pope, 3rd and D. W. Dockery, "Health effects of fine particulate air pollution: lines that connect," (in eng), *Journal of the Air & Waste Management Association (1995)*, vol. 56, no. 6, pp. 709-42, Jun 2006.

[5] C. A. Pope, 3rd *et al.*, "Particulate air pollution as a predictor of mortality in a prospective study of U.S. adults," (in eng), *American journal of respiratory and critical care medicine*, vol. 151, no. 3 Pt 1, pp. 669-74, Mar 1995, doi: 10.1164/ajrccm/151.3_Pt_1.669.

[6] J. M. Samet, F. Dominici, F. C. Curriero, I. Coursac, and S. L. Zeger, "Fine particulate air pollution and mortality in 20 U.S. cities, 1987-1994," (in eng), *The New England journal of medicine*, vol. 343, no. 24, pp. 1742-9, Dec 14 2000, doi: 10.1056/nejm200012143432401.

[7] A. J. Cohen *et al.*, "Urban air pollution," *Comparative quantification of health risks: global and regional burden of disease attributable to selected major risk factors*, vol. 2, pp. 1353-1433, 2004.

[8] S. Deflorio-Barker, J. Crooks, J. Reyes, and A. G. Rappold, "Cardiopulmonary Effects of Fine Particulate Matter Exposure among Older Adults, during Wildfire and Non-Wildfire Periods, in the United States 2008–2010," *Environmental Health Perspectives*, vol. 127, no. 3, p. 037006, 2019-03-01 2019, doi: 10.1289/ehp3860.

[9] Y. Liu, E. Austin, J. Xiang, T. Gould, T. Larson, and E. Seto, "Health Impact Assessment of the 2020 Washington State Wildfire Smoke Episode: Excess Health Burden Attributable to Increased $PM_{2.5}$ Exposures and Potential Exposure Reductions," *GeoHealth*, vol. 5, no. 5, 2021-05-01 2021, doi: 10.1029/2020gh000359.

[10] M. Dennekamp and M. J. Abramson, "The effects of bushfire smoke on respiratory health," *Respirology*, vol. 16, no. 2, pp. 198-209, 2011-02-01 2011, doi: 10.1111/j.1440-1843.2010.01868.x.

[11] J. S. Brown, K. L. Zeman, and W. D. Bennett, "Ultrafine particle deposition and clearance in the healthy and obstructed lung," (in eng), *Am J Respir Crit Care Med*, vol. 166, no. 9, pp. 1240-7, Nov 01 2002, doi: 10.1164/rccm.200205-399OC.

[12] J. Schwartz and L. M. Neas, "Fine Particles Are More Strongly Associated Than Coarse Particles with Acute Respiratory Health Effects in Schoolchildren," *Epidemiology*, vol. 11, no. 1, pp. 6-10, 2000. [Online]. Available: http://www.jstor.org/stable/3703646.

[13] L. L. Nani Guarieiro and A. L. Nani Guarieiro, "Vehicle Emissions: What Will Change with Use of Biofuel?," in *Biofuels - Economy, Environment and Sustainability*: InTech, 2013.

[14] S. G. Tringe *et al.*, "The Airborne Metagenome in an Indoor Urban Environment," *PLoS ONE*, vol. 3, no. 4, p. e1862, 2008-04-02 2008, doi: 10.1371/journal.pone.0001862.

[15] H. Mbareche, L. Morawska, and C. Duchaine, "On the interpretation of bioaerosol exposure measurements and impacts on health," *J. Air Waste Manage. Assoc.*, vol. 69, no. 7, pp. 789-804, 2019-07-03 2019, doi: 10.1080/10962247.2019.1587552.

[16] Y. Li *et al.*, "Probable airborne transmission of SARS-CoV-2 in a poorly ventilated restaurant," *Building and Environment*, vol. 196, p. 107788, 2021, doi: 10.1016/j.buildenv.2021.107788.

[17] S. Asadi, N. Bouvier, A. S. Wexler, and W. D. Ristenpart, "The coronavirus pandemic and aerosols: Does COVID-19 transmit via expiratory particles?," *Aerosol Sci Tech*, vol. 54, no. 6, pp. 635-638, 2020-06-02 2020, doi: 10.1080/02786826.2020.1749229.

[18] L. Morawska *et al.*, "How can airborne transmission of COVID-19 indoors be minimised?," *Environment International*, vol. 142, p. 105832, 2020-09-01 2020, doi: 10.1016/j.envint.2020.105832.

[19] L. Morawska and D. K. Milton, "It Is Time to Address Airborne Transmission of Coronavirus Disease 2019 (COVID-19)," *Clinical Infectious Diseases*, 2020-07-06 2020, doi: 10.1093/cid/ciaa939.

[20] N. Pandey, B. B. Basnet, S. Koju, A. Khapung, and A. Gupta, "Awareness of aerosol-related transmission of COVID-19 among the dentists of Nepal," *BDJ Open*, vol. 7, no. 1, 2021-12-01 2021, doi: 10.1038/s41405-021-00079-0.

[21] L. Setti *et al.*, "Airborne Transmission Route of COVID-19: Why 2 Meters/6 Feet of Inter-Personal Distance Could Not Be Enough," *International Journal of Environmental Research and Public Health*, vol. 17, no. 8, p. 2932, 2020-04-23 2020, doi: 10.3390/ijerph17082932.

[22] C. Foocharoen, U. Peansukwech, P. Pongkulkiat, A. Mahakkanukrauh, and S. Suwannaroj, "Aerosol components associated with hospital mortality in systemic sclerosis: an analysis from a nationwide Thailand healthcare database," *Scientific Reports*, vol. 11, no. 1, 2021-12-01 2021, doi: 10.1038/s41598-021-87114-0.

[23] P. Fabian *et al.*, "Influenza Virus in Human Exhaled Breath: An Observational Study," *PLoS ONE*, vol. 3, no. 7, p. e2691, 2008-07-16 2008, doi: 10.1371/journal.pone.0002691.

[24] B. J. Cowling *et al.*, "Aerosol transmission is an important mode of influenza A virus spread," *Nature Communications*, vol. 4, no. 1, 2013-10-01 2013, doi: 10.1038/ncomms2922.

[25] Z.-D. Guo *et al.*, "Aerosol and Surface Distribution of Severe Acute Respiratory Syndrome Coronavirus 2 in Hospital Wards, Wuhan, China, 2020," *Emerging Infectious Diseases*, vol. 26, no. 7, pp. 1583-1591, 2020-07-01 2020, doi: 10.3201/eid2607.200885.

[26] M. Elbayoumi, N. A. Ramli, and N. F. F. Md Yusof, "Spatial and temporal variations in particulate matter concentrations in twelve schools environment in urban and overpopulated camps landscape," *Building and Environment*, vol. 90, pp. 157-167, 8// 2015, doi: http://dx.doi.org/10.1016/j.buildenv.2015.03.036.

[27] M. M. Patel *et al.*, "Spatial and Temporal Variations in Traffic-related Particulate Matter at New York City High Schools," *Atmospheric environment (Oxford, England : 1994)*, vol. 43, no. 32, pp. 4975-4981, 2009, doi: 10.1016/j.atmosenv.2009.07.004.

[28] *Directive 2008/50/EC of the European Parliament and of the Council of 21 May 2008 on ambient air quality and cleaner air for Europe*, EU, 2008.

[29] (1997a). *40 CFR Parts 50 - Reference Methods for the Determination of Fine Particulate Matter as PM2.5 in the Atmosphere (Appendix L)*.

[30] E. Seto, E. Austin, I. Novosselov, and M. G. Yost, "Use of low-cost particle monitors to calibrate traffic-related air pollutant models in urban areas," in *International Environmental Modelling and Software Society*, 2014.

[31] X. Liu *et al.*, "Low-cost sensors as an alternative for long-term air quality monitoring," *Environmental research*, vol. 185, p. 109438, 2020.
[32] T. Kuhn *et al.*, "Air quality during and after the Commonwealth Games 2018 in Australia: Multiple benefits of monitoring," *Journal of Aerosol Science*, vol. 152, p. 105707, 2021.
[33] W. Jiao *et al.*, "Community Air Sensor Network (CAIRSENSE) project: evaluation of low-cost sensor performance in a suburban environment in the southeastern United States," *Atmospheric Measurement Techniques*, vol. 9, no. 11, pp. 5281-5292, 2016.
[34] S. Makhsous *et al.*, "Methodology for Addressing Infectious Aerosol Persistence in Real-Time Using Sensor Network," 2021.
[35] S. Hegde *et al.*, "Indoor household particulate matter measurements using a network of low-cost sensors," *Aerosol and Air Quality Research*, vol. 20, no. 2, pp. 381-394, 2020.
[36] J. Li *et al.*, "Spatiotemporal distribution of indoor particulate matter concentration with a low-cost sensor network," *Building and Environment*, vol. 127, pp. 138-147, 2018.
[37] G. E. Duncan *et al.*, "Usability of a personal air pollution monitor: Design-feedback iterative cycle study," *JMIR mHealth and uHealth*, vol. 6, no. 12, p. e12023, 2018.
[38] L. Morawska *et al.*, "Indoor aerosols: from personal exposure to risk assessment," *Indoor Air*, vol. 23, no. 6, pp. 462-487, 2013-12-01 2013, doi: 10.1111/ina.12044.
[39] S. Steinle *et al.*, "Personal exposure monitoring of PM2.5 in indoor and outdoor microenvironments," *Science of the Total Environment*, vol. 508, pp. 383-394, Mar 2015, doi: 10.1016/j.scitotenv.2014.12.003.
[40] K. A. Koehler and T. M. Peters, "New Methods for Personal Exposure Monitoring for Airborne Particles," *Current Environmental Health Reports*, vol. 2, no. 4, pp. 399-411, 2015-12-01 2015, doi: 10.1007/s40572-015-0070-z.
[41] O. Stampfer, E. Austin, T. Ganuelas, T. Fiander, E. Seto, and C. J. Karr, "Use of low-cost PM monitors and a multi-wavelength aethalometer to characterize PM2.5 in the Yakama Nation reservation," *Atmospheric Environment*, vol. 224, p. 117292, 2020-03-01 2020, doi: 10.1016/j.atmosenv.2020.117292.
[42] W. M. Jolly *et al.*, "Climate-induced variations in global wildfire danger from 1979 to 2013," *Nature Communications*, vol. 6, no. 1, p. 7537, 2015-11-01 2015, doi: 10.1038/ncomms8537.
[43] M. C. Kennedy, R. R. Bart, C. L. Tague, and J. S. Choate, "Does hot and dry equal more wildfire? Contrasting short‐ and long‐term climate effects on fire in the Sierra Nevada, CA," *Ecosphere*, vol. 12, no. 7, 2021-07-01 2021, doi: 10.1002/ecs2.3657.
[44] R. Barbero, J. T. Abatzoglou, N. K. Larkin, C. A. Kolden, and B. Stocks, "Climate change presents increased potential for very large fires in the contiguous United States," *International Journal of Wildland Fire*, vol. 24, no. 7, p. 892, 2015-01-01 2015, doi: 10.1071/wf15083.
[45] D. V. Spracklen *et al.*, "Impacts of climate change from 2000 to 2050 on wildfire activity and carbonaceous aerosol concentrations in the western United States," *Journal of Geophysical Research*, vol. 114, no. D20, 2009-10-20 2009, doi: 10.1029/2008jd010966.
[46] X. Yue, L. J. Mickley, J. A. Logan, and J. O. Kaplan, "Ensemble projections of wildfire activity and carbonaceous aerosol concentrations over the western United States in the mid-21st century," *Atmospheric Environment*, vol. 77, pp. 767-780, 2013-10-01 2013, doi: 10.1016/j.atmosenv.2013.06.003.
[47] M. Burke, A. Driscoll, S. Heft-Neal, J. Xue, J. Burney, and M. Wara, "The changing risk and burden of wildfire in the United States," *Proceedings of the National Academy of Sciences*, vol. 118, no. 2, p. e2011048118, 2021-01-12 2021, doi: 10.1073/pnas.2011048118.
[48] V. Samburova, B. Zielinska, and A. Khlystov, "Do 16 polycyclic aromatic hydrocarbons represent PAH air toxicity?," *Toxics*, vol. 5, no. 3, p. 17, 2017.
[49] C. P. West *et al.*, "Molecular Composition and the Optical Properties of Brown Carbon Generated by the Ethane Flame," *ACS Earth and Space Chemistry*, vol. 4, no. 7, pp. 1090-1103, 2020/07/16 2020, doi: 10.1021/acsearthspacechem.0c00095.
[50] G. Mahamuni *et al.*, "Excitation–Emission Matrix Spectroscopy for Analysis of Chemical Composition of Combustion Generated Particulate Matter," *Environmental Science & Technology*, vol. 54, no. 13, pp. 8198-8209, 2020/07/07 2020, doi: 10.1021/acs.est.0c01110.
[51] J. Davis, E. Molnar, and I. Novosselov, "Nanostructure transition of young soot aggregates to mature soot aggregates in diluted diffusion flames," *Carbon*, vol. 159, pp. 255-265, 2020/04/15/ 2020, doi: https://doi.org/10.1016/j.carbon.2019.12.043.
[52] J. Davis, K. Tiwari, and I. Novosselov, "Soot morphology and nanostructure in complex flame flow patterns via secondary particle surface growth," *Fuel*, vol. 245, pp. 447-457, 2019/06/01/ 2019, doi: https://doi.org/10.1016/j.fuel.2019.02.058.
[53] N. I. F. Center. "National Large Incident Year-to-Date Report." https://gacc.nifc.gov/index.php (accessed 2021).
[54] C. Xu *et al.*, "Investigation and modeling of the residential infiltration of fine particulate matter in Beijing, China," *J. Air Waste Manage. Assoc.*, vol. 67, no. 6, pp. 694-701, 2017-06-03 2017, doi: 10.1080/10962247.2016.1272503.
[55] B. R. Park, Y. S. Eom, D. H. Choi, and D. H. Kang, "Estimation of Outdoor PM2.5 Infiltration into Multifamily Homes Depending on Building Characteristics Using Regression Models," *Sustainability*, vol. 13, no. 10, p. 5708, 2021-05-19 2021, doi: 10.3390/su13105708.
[56] T. G. Foat *et al.*, "A prototype personal aerosol sampler based on electrostatic precipitation and electrowetting-on-dielectric actuation of droplets," (in English), *J Aerosol Sci*, vol. 95, pp. 43-53, May 2016, doi: 10.1016/j.jaerosci.2016.01.007.
[57] D. Schmechel *et al.*, "A two-stage personal cyclone sampler for the collection of fungal aerosols and direct ELISA and PCR sample analysis," (in English), *J Allergy Clin Immun*, vol. 119, no. 1, pp. S188-S188, Jan 2007, doi: DOI 10.1016/j.jaci.2006.12.102.
[58] K. Willeke, X. J. Lin, and S. A. Grinshpun, "Improved aerosol collection by combined impaction and centrifugal motion," (in English), *Aerosol Sci Tech*, vol. 28, no. 5, pp. 439-456, May 1998, doi: Doi 10.1080/02786829808965536.
[59] A. Arffman, M. Marjamäki, and J. Keskinen, "Simulation of low pressure impactor collection efficiency curves," *J Aerosol Sci*, vol. 42, no. 5, pp. 329-340, 2011, doi: 10.1016/j.jaerosci.2011.02.006.
[60] V. A. Marple, B. Y. H. Liu, and K. T. Whitby, "Fluid mechanics of the laminar flow aerosol impactor," *J Aerosol Sci*, vol. 5, no. 1, pp. 1-IN1, 1974.
[61] S. A. Grinshpun *et al.*, "Collection of airborne spores by circular single-stage impactors with small jet-to-plate distance," *J Aerosol Sci*, vol. 36, no. 5-6, pp. 575-591, 2005, doi: 10.1016/j.jaerosci.2004.06.078.
[62] B. Uk Lee and S. S. Kim, "The effect of varying impaction plate temperature on impactor performance: experimental studies," *J Aerosol Sci*, vol. 33, no. 3, pp. 451-457, 3// 2002, doi: http://dx.doi.org/10.1016/S0021-8502(01)00191-4.
[63] S. Vinchurkar, P. W. Longest, and J. Peart, "CFD simulations of the Andersen cascade impactor: Model development and effects of aerosol charge," *J Aerosol Sci*, vol. 40, no. 9, pp. 807-822, 9// 2009, doi: http://dx.doi.org/10.1016/j.jaerosci.2009.05.005.

[64] C. Dunbar, A. Kataya, and T. Tiangbe, "Reducing bounce effects in the Andersen cascade impactor," *Int J Pharm*, vol. 301, no. 1-2, pp. 25-32, Sep 14 2005, doi: 10.1016/j.ijpharm.2005.04.039.
[65] M. Marjamäki and J. Keskinen, "Effect of impaction plate roughness and porosity on collection efficiency," *J Aerosol Sci*, vol. 35, no. 3, pp. 301-308, 2004, doi: 10.1016/j.jaerosci.2003.09.001.
[66] C.-J. Tsai and Y.-H. Cheng, "Solid Particle Collection Characteristics on Impaction Surfaces of Different Designs," *Aerosol Sci Tech*, vol. 23, no. 1, pp. 96-106, 1995, doi: 10.1080/02786829508965297.
[67] U. N. Lee *et al.*, "Miniaturizing Wet Scrubbers for Aerosolized Droplet Capture," *Anal Chem*, 2021/08/11 2021, doi: 10.1021/acs.analchem.1c01296.
[68] I. V. Novosselov, R. A. Gorder, J. A. Van Amberg, and P. C. Ariessohn, "Design and Performance of a Low-Cost Micro-Channel Aerosol Collector," *Aerosol Sci Tech*, vol. 48, no. 8, pp. 822-830, 2014, doi: 10.1080/02786826.2014.932895.
[69] J. Schreiner, C. Voigt, K. Mauersberger, P. McMurry, and P. Ziemann, "Aerodynamic lens system for producing particle beams at stratospheric pressures," (in English), *Aerosol Sci Tech*, vol. 29, no. 1, pp. 50-56, Jul 1998, doi: Doi 10.1080/02786829808965550.
[70] P. Liu, P. J. Ziemann, D. B. Kittelson, and P. H. Mcmurry, "Generating Particle Beams of Controlled Dimensions and Divergence .1. Theory of Particle Motion in Aerodynamic Lenses and Nozzle Expansions," (in English), *Aerosol Sci Tech*, vol. 22, no. 3, pp. 293-313, Apr 1995, doi: Doi 10.1080/02786829408959748.
[71] P. Liu, P. J. Ziemann, D. B. Kittelson, and P. H. Mcmurry, "Generating Particle Beams of Controlled Dimensions and Divergence .2. Experimental Evaluation of Particle Motion in Aerodynamic Lenses and Nozzle Expansions," (in English), *Aerosol Sci Tech*, vol. 22, no. 3, pp. 314-324, Apr 1995, doi: Doi 10.1080/02786829408959749.
[72] P. J. Ziemann, P. Liu, N. P. Rao, D. B. Kittelson, and P. H. Mcmurry, "Particle-Beam Mass-Spectrometry of Submicron Particles Charged to Saturation in an Electron-Beam," (in English), *J Aerosol Sci*, vol. 26, no. 5, pp. 745-756, Jul 1995, doi: Doi 10.1016/0021-8502(95)00009-2.
[73] J. Schreiner *et al.*, "A mass spectrometer system for analysis of polar stratospheric aerosols," (in English), *Rev Sci Instrum*, vol. 73, no. 2, pp. 446-452, Feb 2002, doi: 10.1063/1.1430732.
[74] J. N. Shu *et al.*, "Online MALDI-TOF MS Using an Aerodynamic Lens Assembly as a Direct Deposition Interface," (in English), *Anal Chem*, vol. 82, no. 13, pp. 5906-5909, Jul 1 2010, doi: 10.1021/ac100941z.
[75] W. H. Benner, M. J. Bogan, U. Rohner, S. Boutet, B. Woods, and M. Frank, "Non-destructive characterization and alignment of aerodynamically focused particle beams using single particle charge detection," (in English), *J Aerosol Sci*, vol. 39, no. 11, pp. 917-928, Nov 2008, doi: 10.1016/j.jaerosci.2008.05.008.
[76] K. Park, G. Cho, and J. H. Kwak, "Development of an Aerosol Focusing-Laser Induced Breakdown Spectroscopy (Aerosol Focusing-LIBS) for Determination of Fine and Ultrafine Metal Aerosols," (in English), *Aerosol Sci Tech*, vol. 43, no. 5, pp. 375-386, 2009, doi: 10.1080/02786820802662947.
[77] J. Schreiner, U. Schild, C. Voigt, and K. Mauersberger, "Focusing of aerosols into a particle beam at pressures from 10 to 150 Torr," (in English), *Aerosol Sci Tech*, vol. 31, no. 5, pp. 373-382, Nov 1999, doi: Doi 10.1080/027868299304093.
[78] J. W. Lee, M. Y. Yi, and S. M. Lee, "Inertial focusing of particles with an aerodynamic lens in the atmospheric pressure range," (in English), *J Aerosol Sci*, vol. 34, no. 2, pp. 211-224, Feb 2003, doi: Pii S0021-8502(02)00158-1
Doi 10.1016/S0021-8502(02)00158-1.
[79] R. Deng, X. Zhang, K. A. Smith, J. Wormhoudt, D. K. Lewis, and A. Freedman, "Focusing Particles with Diameters of 1 to 10 Microns into Beams at Atmospheric Pressure," *Aerosol Sci Tech*, vol. 42, no. 11, pp. 899-915, 2008, doi: 10.1080/02786820802360674.
[80] I. V. Novosselov and P. C. Ariessohn, "Rectangular Slit Atmospheric Pressure Aerodynamic Lens Aerosol Concentrator," *Aerosol Sci Tech*, vol. 48, no. 2, pp. 163-172, 2013, doi: 10.1080/02786826.2013.865832.
[81] A. Peters *et al.*, "Translocation and potential neurological effects of fine and ultrafine particles a critical update," *Particle and fibre toxicology*, vol. 3, no. 1, p. 13, 2006.
[82] S. Fuzzi *et al.*, "Particulate matter, air quality and climate: lessons learned and future needs," *Atmospheric chemistry and physics*, vol. 15, no. 14, pp. 8217-8299, 2015.
[83] R. A. Dobbins, "Soot inception temperature and the carbonization rate of precursor particles," *Combustion and Flame*, vol. 130, no. 3, pp. 204-214, 2002.
[84] S. E. Stein and A. Fahr, "High-temperature stabilities of hydrocarbons," *The Journal of Physical Chemistry*, vol. 89, no. 17, pp. 3714-3725, 1985.
[85] M. Commodo *et al.*, "On the early stages of soot formation: Molecular structure elucidation by high-resolution atomic force microscopy," *Combustion and Flame*, vol. 205, pp. 154-164, 2019.
[86] D. Chen, J. Akroyd, S. Mosbach, D. Opalka, and M. Kraft, "Solid–liquid transitions in homogenous ovalene, hexabenzocoronene and circumcoronene clusters: A molecular dynamics study," *Combustion and Flame*, vol. 162, no. 2, pp. 486-495, 2015.
[87] D. Aubagnac-Karkar, A. El Bakali, and P. Desgroux, "Soot particles inception and PAH condensation modelling applied in a soot model utilizing a sectional method," *COMBUSTION AND FLAME*, vol. 189, pp. 190-206, 2018.
[88] J. Davis, "Characterization of combustion generated particulates produced in an inverted gravity flame reactor " Ph.D., University of Washington, Seattle, 2019.
[89] J. J. Cao *et al.*, "Spatial and seasonal variations of atmospheric organic carbon and elemental carbon in Pearl River Delta Region, China," *Atmospheric Environment*, vol. 38, no. 27, pp. 4447-4456, 2004/09/01/ 2004, doi: 10.1016/j.atmosenv.2004.05.016.
[90] J. C. Chow, J. G. Watson, L. W. A. Chen, J. Rice, and N. H. Frank, "Quantification of PM2.5 organic carbon sampling artifacts in US networks," (in English), *Atmospheric Chemistry and Physics*, vol. 10, no. 12, pp. 5223-5239, 2010/06/15/ 2010, doi: https://doi.org/10.5194/acp-10-5223-2010.
[91] P. Lin, L. T. Fleming, S. A. Nizkorodov, J. Laskin, and A. Laskin, "Comprehensive Molecular Characterization of Atmospheric Brown Carbon by High Resolution Mass Spectrometry with Electrospray and Atmospheric Pressure Photoionization," *Analytical Chemistry*, vol. 90, no. 21, pp. 12493-12502, 2018/11/06/ 2018, doi: 10.1021/acs.analchem.8b02177.
[92] Y. Wei, I.-K. Han, M. Hu, M. Shao, J. Zhang, and X. Tang, "Personal exposure to particulate PAHs and anthraquinone and oxidative DNA damages in humans," *Chemosphere*, vol. 81, no. 10, pp. 1280-1285, 2010/11/01/ 2010, doi: 10.1016/j.chemosphere.2010.08.055.
[93] S. Bonetta *et al.*, "DNA damage in A549 cells exposed to different extracts of PM2.5 from industrial, urban and highway sites," *Chemosphere*, vol. 77, no. 7, pp. 1030-1034, 2009/11/01/ 2009, doi: 10.1016/j.chemosphere.2009.07.076.

[94] Y. Wei, I.-K. Han, M. Shao, M. Hu, J. Zhang, and X. Tang, "PM2.5 Constituents and Oxidative DNA Damage in Humans," *Environ. Sci. Technol.*, vol. 43, no. 13, pp. 4757-4762, 2009/07/01/ 2009, doi: 10.1021/es803337c.
[95] R. J. Delfino, C. Sioutas, and S. Malik, "Potential role of ultrafine particles in associations between airborne particle mass and cardiovascular health," (in English), *Environmental Health Perspectives*, vol. 113, no. 8, pp. 934-946, Aug 2005, doi: 10.1289/ehp.7938.
[96] R. J. Delfino, N. Staimer, T. Tjoa, D. L. Gillen, J. J. Schauer, and M. M. Shafer, "Airway inflammation and oxidative potential of air pollutant particles in a pediatric asthma panel," (in English), *Journal of Exposure Science and Environmental Epidemiology*, vol. 23, no. 5, pp. 466-473, Sep-Oct 2013, doi: 10.1038/jes.2013.25.
[97] V. Samburova, B. Zielinska, and A. Khlystov, "Do 16 Polycyclic Aromatic Hydrocarbons Represent PAH Air Toxicity?," *Toxics*, vol. 5, no. 3, 2017/08/15/ 2017, doi: 10.3390/toxics5030017.
[98] I. W. G. o. t. E. o. C. R. t. Humans and C. International Agency for Research on, Eds. *Some non-heterocyclic polycyclic aromatic hydrocarbons and some related occupational exposures* (IARC monographs on the evaluation of carcinogenic risks to humans, no. v. 92). Lyon, France : Geneva: IARC Press ; Distributed by World Health Organization (in en), 2010, p. 853.
[99] I. Berlman, *Handbook of florescence spectra of Aromatic Molecules*. Elsevier (in en), 2012, p. 488.
[100] D. Gao, T. Fang, V. Verma, L. G. Zeng, and R. J. Weber, "A method for measuring total aerosol oxidative potential (OP) with the dithiothreitol (DTT) assay and comparisons between an urban and roadside site of water-soluble and total OP," (in English), *Atmos Meas Tech*, vol. 10, no. 8, pp. 2821-2835, Aug 8 2017, doi: 10.5194/amt-10-2821-2017.
[101] Y. Sameenoi *et al.*, "Microfluidic Paper-Based Analytical Device for Aerosol Oxidative Activity," (in English), *Environmental Science & Technology*, vol. 47, no. 2, pp. 932-940, Jan 15 2013, doi: 10.1021/es304662w.
[102] Y. Sameenoi *et al.*, "Microfluidic Electrochemical Sensor for On-Line Monitoring of Aerosol Oxidative Activity," (in English), *J Am Chem Soc*, vol. 134, no. 25, pp. 10562-10568, Jun 27 2012, doi: 10.1021/ja3031104.
[103] U. Poschl, "Atmospheric aerosols: Composition, transformation, climate and health effects," (in English), *Angew Chem Int Edit*, vol. 44, no. 46, pp. 7520-7540, 2005, doi: 10.1002/anie.200501122.
[104] H. Jung, B. Guo, C. Anastasio, and I. M. Kennedy, "Quantitative measurements of the generation of hydroxyl radicals by soot particles in a surrogate lung fluid," (in English), *Atmospheric Environment*, vol. 40, no. 6, pp. 1043-1052, Feb 2006, doi: 10.1016/j.atmosenv.2005.11.015.
[105] E. Vidrio, C. H. Phuah, A. M. Dillner, and C. Anastasio, "Generation of Hydroxyl Radicals from Ambient Fine Particles in a Surrogate Lung Fluid Solution," (in English), *Environmental Science & Technology*, vol. 43, no. 3, pp. 922-927, Feb 1 2009, doi: 10.1021/es801653u.
[106] E. Ghelfi, C. Ramos-Rhoden, G. A. Wellenius, J. Lawrence, and B. Gonzalez-Flecha, "Cardiac oxidative stress and electrophysiological changes in rats exposed to concentrated ambient particles are mediated by TRP-dependent pulmonary reflexes," (in English), *Toxicol Sci*, vol. 102, no. 2, pp. 328-336, Apr 2008, doi: 10.1093/toxsci/kfn005.
[107] N. Li *et al.*, "Ultrafine particulate pollutants induce oxidative stress and mitochondrial damage," (in eng), *Environ Health Perspect*, vol. 111, no. 4, pp. 455-60, Apr 2003, doi: 10.1289/ehp.6000.
[108] H. J. Lee, A. Laskin, J. Laskin, and S. A. Nizkorodov, "Excitation–emission spectra and fluorescence quantum yields for fresh and aged biogenic secondary organic aerosols," *Environmental science & technology*, vol. 47, no. 11, pp. 5763-5770, 2013.
[109] S. M. Phillips and G. D. Smith, "Further evidence for charge transfer complexes in brown carbon aerosols from excitation–emission matrix fluorescence spectroscopy," *The Journal of Physical Chemistry A*, vol. 119, no. 19, pp. 4545-4551, 2015.
[110] Q. Chen, F. Ikemori, and M. Mochida, "Light absorption and excitation–emission fluorescence of urban organic aerosol components and their relationship to chemical structure," *Environmental Science & Technology*, vol. 50, no. 20, pp. 10859-10868, 2016.
[111] J. T. Matos, S. M. Freire, R. M. Duarte, and A. C. Duarte, "Natural organic matter in urban aerosols: Comparison between water and alkaline soluble components using excitation–emission matrix fluorescence spectroscopy and multiway data analysis," *Atmospheric Environment*, vol. 102, pp. 1-10, 2015.
[112] J. W. Rutherford *et al.*, "Excitation emission matrix fluorescence spectroscopy for combustion generated particulate matter source identification," *Atmospheric Environment*, vol. 220, p. 117065, 2020/01/01/ 2020, doi: https://doi.org/10.1016/j.atmosenv.2019.117065.
[113] C.-H. Huang, J. He, E. Austin, E. Seto, and I. Novosselov, "Assessing the Value of Complex Refractive Index and Particle Density for Calibration of Low-Cost Particle Matter Sensor for Size-Resolved Particle Count and PM2. 5 Measurements," *arXiv preprint arXiv:2106.12889*, 2021.
[114] R. S. Vaddi, Y. Guan, and I. Novosselov, "Behavior of ultrafine particles in electro-hydrodynamic flow induced by corona discharge," *Journal of Aerosol Science*, p. 105587, 2020.
[115] J. Y. He and I. V. Novosselov, "Design and evaluation of an aerodynamic focusing micro-well aerosol collector," (in English), *Aerosol Science and Technology*, vol. 51, no. 9, pp. 1016-1026, 2017/09/02 2017, doi: 10.1080/02786826.2017.1329515.
[116] R. S. Vaddi, Y. Guan, and I. Novosselov, "Particle Dynamics in Corona Induced Electro-hydrodynamic Flow," *arXiv:1902.02986*, 2019.
[117] T. Shefelbine, C. Forehand, and K. Rink, "3MTM Ceramic Microspheres in Architectural Paint," 2015. [Online]. Available: https://multimedia.3m.com/mws/media/1123884O/ceramic-microsphere-product-comparison-technical-paper.pdf?fn=10892%20Ceramic%20Microsphere%20Produc.
[118] J. Xiang *et al.*, "Using Vehicles' Rendezvous for In Situ Calibration of Instruments in Fleet Vehicle-Based Air Pollution Mobile Monitoring," *Environmental Science & Technology*, vol. 54, no. 7, pp. 4286-4294, 2020/04/07 2020, doi: 10.1021/acs.est.0c00612.
[119] D. H. Hagan and J. H. Kroll, "Assessing the accuracy of low-cost optical particle sensors using a physics-based approach," (in eng), *Atmospheric measurement techniques*, vol. 13, no. 11, pp. 6343-6355, 2020, doi: 10.5194/amt-13-6343-2020.
[120] T. Njalsson and I. Novosselov, "Design and optimization of a compact low-cost optical particle sizer," *Journal of Aerosol Science*, vol. 119, pp. 1-12, 2018.
[121] E. Austin, I. Novosselov, E. Seto, and M. G. Yost, "Laboratory Evaluation of the Shinyei PPD42NS Low-Cost Particulate Matter Sensor," *PloS one*, vol. 10, no. 9, p. e0137789, 2015.
[122] B. Feenstra *et al.*, "Performance evaluation of twelve low-cost PM2. 5 sensors at an ambient air monitoring site," *Atmospheric Environment*, vol. 216, p. 116946, 2019.
[123] R. Jayaratne *et al.*, "Low-cost PM2. 5 sensors: An assessment of their suitability for various applications," *Aerosol and Air Quality Research*, vol. 20, no. 3, pp. 520-532, 2020.

[124] J. Xiang *et al.*, "Impacts of the COVID-19 responses on traffic-related air pollution in a Northwestern US city," *Science of The Total Environment*, vol. 747, p. 141325, 2020/12/10/ 2020, doi: https://doi.org/10.1016/j.scitotenv.2020.141325.
[125] C.-H. Huang *et al.*, "Impacts of using auto-mode portable air cleaner on indoor PM2.5 levels: An intervention study," *Building and Environment*, vol. 188, p. 107444, 2021/01/15/ 2021, doi: https://doi.org/10.1016/j.buildenv.2020.107444.
[126] J. Namieśnik, B. Zabiegała, A. Kot-Wasik, M. Partyka, and A. Wasik, "Passive sampling and/or extraction techniques in environmental analysis: a review," (in eng), *Anal Bioanal Chem*, vol. 381, no. 2, pp. 279-301, Jan 2005, doi: 10.1007/s00216-004-2830-8.
[127] I. Lee *et al.*, "Integrated Bioaerosol Sampling/Monitoring Platform: Field-Deployable and Rapid Detection of Airborne Viruses," (in eng), *ACS Sens*, vol. 5, no. 12, pp. 3915-3922, Dec 24 2020, doi: 10.1021/acssensors.0c01531.
[128] C. W. Haig, W. G. Mackay, J. T. Walker, and C. Williams, "Bioaerosol sampling: sampling mechanisms, bioefficiency and field studies," (in eng), *J Hosp Infect*, vol. 93, no. 3, pp. 242-55, Jul 2016, doi: 10.1016/j.jhin.2016.03.017.
[129] J. He *et al.*, "Evaluation of micro-well collector for capture and analysis of aerosolized Bacillus subtilis spores," *PloS one*, vol. 13, no. 5, p. e0197783, 2018.
[130] J. S. Kesavan, R. W. Doherty, and J. R. Bottiger, "Performance Characterization Methods of Aerosol Samplers," DTIC Document, 2003.
[131] S. Rennecke and A. P. Weber, "The critical velocity for nanoparticle rebound measured in a low pressure impactor," (in English), *J Aerosol Sci*, vol. 58, pp. 135-147, Apr 2013. [Online]. Available: <Go to ISI>://WOS:000317949200012.
[132] M. Chen, F. J. Romay, L. Li, A. Naqwi, and V. A. Marple, "A novel quartz crystal cascade impactor for real-time aerosol mass distribution measurement," (in English), *Aerosol Sci Tech*, vol. 50, no. 9, pp. 971-983, 2016. [Online]. Available: <Go to ISI>://WOS:000382192000010.
[133] S. Payet, D. Boulaud, G. Madelaine, and A. Renoux, "Penetration and pressure drop of a HEPA filter during loading with submicron liquid particles," *J Aerosol Sci*, vol. 23, no. 7, pp. 723-735, 1992/10/01 1992, doi: http://dx.doi.org/10.1016/0021-8502(92)90039-X.
[134] J. He and I. V. Novosselov, "Design and evaluation of an aerodynamic focusing micro-well aerosol collector," *Aerosol Science and Technology*, no. just-accepted, 2017.
[135] X. Zhang, K. A. Smith, D. R. Worsnop, J. Jimenez, J. T. Jayne, and C. E. Kolb, "A Numerical Characterization of Particle Beam Collimation by an Aerodynamic Lens-Nozzle System: Part I. An Individual Lens or Nozzle," *Aerosol Sci Tech*, vol. 36, no. 5, pp. 617-631, 2002, doi: 10.1080/02786820252883856.
[136] J. Goo, "Numerical simulation of aerosol concentration at atmospheric pressure by a cascade of aerodynamic slit lenses," *Journal of aerosol science*, vol. 33, no. 11, pp. 1493-1507, 2002.
[137] I. V. Novosselov and P. C. Ariessohn, "Rectangular slit atmospheric pressure aerodynamic lens aerosol concentrator," *Aerosol Science and Technology*, vol. 48, no. 2, pp. 163-172, 2014.
[138] L. R. e. Al, "Swab Materials and Bacillus anthracis Spore Recovery from Nonporous Surfaces - Volume 10, Number 6—June 2004 - Emerging Infectious Disease journal - CDC," (in en-us), doi: 10.3201/eid1006.030716.
[139] O. o. R. Development. "Literature Review of Protocols for Processing Soils Contaminated with Bacillus anthracis Spores." (accessed.
[140] M. Pospíšilová, G. Kuncová, and J. Trögl, "Fiber-optic chemical sensors and fiber-optic bio-sensors," *Sensors*, vol. 15, no. 10, pp. 25208-25259, 2015.
[141] O. S. Wolfbeis, "Fiber-optic chemical sensors and biosensors," *Anal Chem*, vol. 80, no. 12, pp. 4269-4283, 2008.
[142] B. R. Pinkard *et al.*, "Raman Spectroscopic Data from Formic Acid Decomposition in Subcritical and Supercritical Water," *Data in Brief*, p. 105312, 2020.
[143] A. Kudelski, "Analytical applications of Raman spectroscopy," *Talanta*, vol. 76, no. 1, pp. 1-8, 2008.
[144] B. J. Marquardt, T. Le, and L. W. Burgess, "Demonstration of a high-precision optical probe for effective sampling of solids by Raman spectroscopy," in *Raman Spectroscopy and Light Scattering Technologies in Materials Science*, 2001, vol. 4469: International Society for Optics and Photonics, pp. 62-70.
[145] S. Farquharson, L. Grigely, V. Khitrov, W. Smith, J. F. Sperry, and G. Fenerty, "Detecting Bacillus cereus spores on a mail sorting system using Raman spectroscopy," *Journal of Raman spectroscopy*, vol. 35, no. 1, pp. 82-86, 2004.
[146] B. R. Pinkard, D. J. Gorman, E. G. Rasmussen, J. C. Kramlich, P. G. Reinhall, and I. V. Novosselov, "Kinetics of formic acid decomposition in subcritical and supercritical water – a Raman spectroscopic study," *International Journal of Hydrogen Energy*, vol. 44, no. 60, pp. 31745-31756, 2019/12/06/ 2019, doi: https://doi.org/10.1016/j.ijhydene.2019.10.070.
[147] B. R. Pinkard, A. L. Purohit, S. J. Moore, J. C. Kramlich, P. G. Reinhall, and I. V. Novosselov, "Partial Oxidation of Ethanol in Supercritical Water," *Industrial & Engineering Chemistry Research*, vol. 59, no. 21, pp. 9900-9911, 2020/05/27 2020, doi: 10.1021/acs.iecr.0c00945.
[148] B. R. Pinkard, S. Shetty, J. C. Kramlich, P. G. Reinhall, and I. V. Novosselov, "Hydrolysis of Dimethyl Methylphosphonate (DMMP) in Hot-Compressed Water," *The Journal of Physical Chemistry A*, vol. 124, no. 41, pp. 8383-8389, 2020/10/15 2020, doi: 10.1021/acs.jpca.0c05104.
[149] P. L. Stiles, J. A. Dieringer, N. C. Shah, and R. P. Van Duyne, "Surface-enhanced Raman spectroscopy," *Annu. Rev. Anal. Chem.*, vol. 1, pp. 601-626, 2008.
[150] G. I. Petrov, V. V. Yakovlev, A. V. Sokolov, and M. O. Scully, "Detection of Bacillus subtilis spores in water by means of broadband coherent anti-Stokes Raman spectroscopy," *Optics Express*, vol. 13, no. 23, pp. 9537-9542, 2005.
[151] V. Sivaprakasam, A. L. Huston, C. Scotto, and J. D. Eversole, "Multiple UV wavelength excitation and fluorescence of bioaerosols," *Optics express*, vol. 12, no. 19, pp. 4457-4466, 2004.
[152] J. Eversole, W. Cary, C. Scotto, R. Pierson, M. Spence, and A. Campillo, "Continuous bioaerosol monitoring using UV excitation fluorescence: Outdoor test results," *Field Analytical Chemistry & Technology*, vol. 5, no. 4, pp. 205-212, 2001.
[153] R. G. Zepp, W. M. Sheldon, and M. A. Moran, "Dissolved organic fluorophores in southeastern US coastal waters: correction method for eliminating Rayleigh and Raman scattering peaks in excitation–emission matrices," *Marine Chemistry*, vol. 89, no. 1, pp. 15-36, 2004/10/01/ 2004, doi: https://doi.org/10.1016/j.marchem.2004.02.006.
[154] Y. Guan, R. S. Vaddi, A. Aliseda, and I. Novosselov, "Analytical model of electro-hydrodynamic flow in corona discharge," *Physics of Plasmas*, vol. 25, no. 8, p. 083507, 2018.
[155] Y. Guan, R. S. Vaddi, A. Aliseda, and I. Novosselov, "Experimental and numerical investigation of electrohydrodynamic flow in a point-to-ring corona discharge," *Physical Review Fluids*, vol. 3, no. 4, p. 043701, 2018.

[156] A. Tang, R. S. Vaddi, A. Mamishev, and I. V. Novosselov, "Empirical relations for discharge current and momentum injection in dielectric barrier discharge plasma actuators," *Journal of Physics D: Applied Physics*, vol. 54, no. 24, p. 245204, 2021/03/31 2021, doi: 10.1088/1361-6463/abec0b.
[157] G. Mahamuni, B. Ockerman, and I. Novosselov, "Electrostatic Capillary Collector for In-Situ Spectroscopic Analysis of Aerosols," *Aerosol Science and Technology*, pp. 1-40, 2019, doi: 10.1080/02786826.2019.1600653.
[158] M. Gaurav *et al.*, *Solid Phase Excitation-Emission Matrix Spectroscopy for In-Situ Chemical Analysis of Combustion Aerosols*. 2020.
[159] G. Mahamuni *et al.*, "Solid-phase excitation-emission matrix spectroscopy for chemical analysis of combustion aerosols," *PLOS ONE*, vol. 16, no. 5, p. e0251664, 2021, doi: 10.1371/journal.pone.0251664.